

POSITIVE DISPLACEMENT FLUID FLUTTER
USING COUPLED PLATE STRAIN ENERGY DEFLECTION

A Thesis

presented to

the Faculty of the Graduate School

at the University of Missouri – Columbia

In Partial Fulfillment

of the Requirements for the Degree

Master of Science in Mechanical Engineering

ROBERT D. CHAPMAN

DR. FRANK FENG, FACULTY ADVISOR

MAY 2013

The undersigned, appointed by the dean of the Graduate School, have examined the thesis entitled

POSITIVE DISPLACEMENT FLUID FLUTTER
USING COUPLED PLATE STRAIN ENERGY DEFLECTION

presented by Robert D. Chapman,

a candidate for the degree of Master of Science in Mechanical Engineering,

and hereby certify that, in their opinion, it is worthy of acceptance.

Professor Frank Feng, PhD

Professor Roger Fales, PhD

Professor Kevin C. Dellsperger MD, PhD

ACKNOWLEDGEMENTS

I would like to thank the Missouri Space Grant Consortium (MSGC) for funding my research assistantship; Dr. Feng for granting me the opportunity to serve as a teaching and research assistant; Dr. John Miles for making possible my continued search for higher education and passion for knowledge; Dr. Pai for helping me comprehend finite element mathematical formulation; Dr. Fales for expanding knowledgebase of hydraulic control systems and rigid body dynamics; Dr. Smith for allowing software usage to conduct numerical simulation analyses; and Dr. Dellsperger for his expertise in cardiac function and foresight in the application of the proposed concept.

ABSTRACT

In nature, there exist highly evolved mechanical systems which exploit passive mechanical compliance and material property transients to impart hydraulic actuation and fluid motion. The human heart generates blood flow through periodic geometric chamber contraction and expansion. Delicate red blood cell corpuscles transport oxygen and nutrient requirements throughout the body. Applying a cyclical impulse pressure transient, the heart squeezes this incompressible fluid through the vascular network. No such current state fluid flow device exists that is capable of replicating nonlinear fluid particle motion without severely damaging the fragile oxygen-carrying red blood cells. A new type of pump mechanism is provided to demonstrate flow pressure and mass transport that can be utilized as to replicate the cardiac cycle fluid motion. The concept of fluid flutter using shell mechanical pre-compression strain energy is provided as a viable method for actuation of fluid particles in a nonlinear periodic cycle. Using commercially available software and implicit numerical solver schemes, a fluid-structural interaction problem is formulated. Simple flask container geometry is developed to illustrate symmetric chamber halves undergoing simultaneous fluid contraction and expansion. Passive valve actuation is employed as a means to regulate the induced fluid chamber ejection pressure.

TABLE OF CONTENTS

ACKNOWLEDGEMENTS	ii
ABSTRACT.....	iii
LIST OF ILLUSTRATIONS	vi
1 INTRODUCTION	1
1.1 CARDIAC PHYSIOLOGY	2
1.2 CARDIAC STRUCTURE & FUNCTION	6
1.3 DEVELOPMENT OF THE ARTIFICIAL HEART – A PRIORI ART	10
2 CONSTITUTIVE FLUID DYNAMICS.....	13
2.1 GOVERNING FLUID CONSERVATION PRINCIPLES.....	13
2.2 INCOMPRESSIBLE NEWTONIAN LAMINAR FLUID FLOW	15
3 STRUCTURAL MECHANICS.....	20
3.1 GOVERNING EQUATIONS OF MOTION	20
3.2 ELASTIC DEFORMATION & STRAIN	21
3.3 EQUILIBRIUM & VIRTUAL WORK	22
3.4 NONLINEAR SOLUTION METHODS.....	24
3.5 IMPLICIT DYNAMIC ANALYSIS	25
3.6 SHELL ELEMENTS	27
3.7 PLATE BUCKLING – CLASSICAL PLATE THEORY	28
3.8 THE LIMIT CYCLE	31
4 FLUID-STRUCTURAL INTERACTION	32
4.1 FLUID-STRUCTURE INTERACTION COUPLING.....	32

4.2	COUPLING PLATE STRAIN ENERGY TO GENERATE FLUID FLOW	35
4.3	USE OF COMMERCIAL SOFTWARE TOOLS - THE PHILOSOPHY	39
4.4	COUPLING STAR-CCM+ AND ABAQUS CO-SIMULATION	40
4.5	INDUCED SHELL BIFURCATION FINITE ELEMENT ANALYSIS	43
4.6	INDUCED FLASK BIFURCATION DYNAMIC RESPONSE	54
4.7	DEVELOPMENT OF FLUID STRUCTURE INTERACTION MODEL	58
4.7.1	Geometry Creation	64
4.7.2	Mesh Generation	65
4.7.3	Fluid Properties & Physics	66
4.7.4	Boundary Conditions.....	66
4.7.5	Computational Fluid Dynamics Solver	67
4.7.6	Numerical Methods for Computational Fluid Dynamics.....	67
4.8	ENCAPSULATING FLUID CONTAINER DYNAMIC BIFURCATION	68
4.9	IMPLICIT DYNAMIC FLASK DEFLECTION FLUID RESPONSE	72
4.10	FLAPPER NOZZLE VALVE DESIGN.....	101
4.10.1	Flapper Nozzle Valve Model.....	103
4.10.2	Model Simulation Results	106
4.11	QUADRANT CUSPED PASSIVE VALVE ACTUATION.....	111
5	CONCLUSION.....	115
	BIBLIOGRAPHY.....	116

LIST OF ILLUSTRATIONS

Figure 1.1.a Pressure, volume response versus time.....	2
Figure 1.1.b Left ventricle cardiac pressure versus volume.....	3
Figure 1.1.c Left ventricle pressure range.....	4
Figure 1.2.a Cardiac structure	7
Figure 1.2.b Pressure as a function of time at cardiac stages.....	9
Figure 3.1.a Second order conceptual model.....	20
Figure 3.7.a Plate curvature variable definition.....	28
Figure 3.7.b CCW (top) & CW (bottom) input torque couple to strained, constrained plate	30
Figure 3.8.a Limit cycle trajectory oscillations.....	31
Figure 4.2.a Fluid structure interaction.....	35
Figure 4.2.b Irreversible bifurcation fluid motion control volume	36
Figure 4.2.c Reversible bifurcation fluid motion control volume.....	36
Figure 4.2.d Four chamber closed configuration	37
Figure 4.2.e CCW & CW input torque coupling strained, constrained plate bisection	38
Figure 4.5.a Shell boundary conditions	43
Figure 4.5.b Shell applied loading	44
Figure 4.5.c Applied CCW shell input torque	44
Figure 4.5.d Applied CW shell input torque.....	45
Figure 4.5.e Shell face displacement versus time	45
Figure 4.5.f Shell edge displacement versus time.....	46
Figure 4.5.g Induced shell strain energy versus time.....	47
Figure 4.5.h Shell strain energy versus displacement.....	48
Figure 4.5.i Shell edge load versus time	48
Figure 4.5.j Shell edge load versus induced strain energy	49
Figure 4.5.k Shell surface displacement versus edge load.....	50
Figure 4.5.l Shell CW & CCW equilibrium positions	51
Figure 4.5.m Shell deflection path along surface edge	53
Figure 4.6.a Flask style container	54
Figure 4.6.b Applied CCW input torque.....	55
Figure 4.6.c Applied CCW input torque.....	55
Figure 4.6.d Flask spline applied CCW input torque.....	56

Figure 4.6.e Flask spline applied CW input torque.....	56
Figure 4.6.f Applied CCW input torque equilibrium position	57
Figure 4.7.a Simple fluid boundary configuration for single shell FSI interface.....	59
Figure 4.7.b Structural nodal displacement superimposed on the fluid FSI interface	59
Figure 4.7.c Morphed mesh discretization in the equilibrium deflection position	60
Figure 4.7.d Scalar field pressure output along FSI interface.....	61
Figure 4.7.e Left and right fluid region morphed mesh discretization in the deflected position ...	62
Figure 4.7.f Left and right side computed scalar field pressure.....	63
Figure 4.8.a Applied master shell surface traction.....	69
Figure 4.8.b Master & slave surface mesh discretization	69
Figure 4.8.c Applied CCW input torque	70
Figure 4.9.a Structural nodal displacement superimposed on the FSI interface	73
Figure 4.9.b Left side fluid region mesh discretization	73
Figure 4.9.c Morphed mesh discretization in the deflected equilibrium position.....	74
Figure 4.9.d Scalar field pressure	74
Figure 4.9.e Applied CCW input torque left side fluid region volume decrease.....	76
Figure 4.9.f No-slip wall shear stress increase.....	77
Figure 4.9.g Mass flow rate ejection through virtual ports	78
Figure 4.9.h Fluid volume contraction pressure decrease.....	80
Figure 4.9.i Morphed mesh discretization in the deflected equilibrium position	81
Figure 4.9.j Applied CW input torque left side fluid region volume increase	81
Figure 4.9.k Pressure generated fluid work profile.....	82
Figure 4.9.l No-slip wall shear stress increase.....	83
Figure 4.9.m Fluid volume expansion pressure profile.....	85
Figure 4.9.n Left & right side fluid region initial mesh discretization	86
Figure 4.9.o Left & right side final mesh discretization	86
Figure 4.9.p Velocity field through forward port boundaries	87
Figure 4.9.q Scalar field mass flux through permeable forward port boundaries	88
Figure 4.9.r Left & right aft port mass flow rate.....	88
Figure 4.9.s Left & right forward port mass flow rate.....	89
Figure 4.9.t Finite volume observed maximum pressure	91
Figure 4.9.u Left & right pressure generated work profile	92
Figure 4.9.v Applied CCW input torque scalar field pressure response.....	93

Figure 4.9.w Morphed mesh discretization in equilibrium position	93
Figure 4.9.x Finite volume observed maximum pressure	94
Figure 4.9.y Left & right side port surface force	95
Figure 4.9.z Left & right side pressure generated work.....	96
Figure 4.9.aa Left & right side ejection port mass flow rate.....	97
Figure 4.9.bb Shell strain energy versus time	98
Figure 4.9.cc Shell input energy versus time	100
Figure 4.10.a Flapper nozzle variable definition	102
Figure 4.10.b Conceptual valve synchronization mapping.....	102
Figure 4.10.c MATLAB Simulink flapper valve control system flow diagram	105
Figure 4.10.d Flapper valve control pressure versus time	106
Figure 4.10.e Flapper rotation angle versus time.....	107
Figure 4.10.f Angular velocity versus time.....	107
Figure 4.10.g Control pressure overshoot response	108
Figure 4.10.h Valve control pressure versus time.....	108
Figure 4.10.i Control pressure versus rotation angle	109
Figure 4.10.j Volumetric flow rate versus time	109
Figure 4.10.k Control pressure versus ejection volume.....	110
Figure 4.11.a Quadrant cusped flapper valve mesh discretization.....	112
Figure 4.11.b Applied surface pressure deflection	112
Figure 4.11.c Valve deflection versus actuating pressure.....	113

1 INTRODUCTION

The human heart undergoes periodic nonlinear deformation that mimics the dynamics of a limit cycle. Given the geometric construct of the heart and the evolved electro-chemical actuation, the heart squeezes and responds to force blood throughout the body. The development of such a device could be highly instrumental in transporting delicate fluid through a system without inducing violent shear stresses or chaotic fluid turbidity which damage delicate red blood cell corpuscles. Forcing blood through the vast array of arteries and veins requires a transient pressure pulse followed by a periodic static pressure to permit mass transport. Contraction of the heart decreases ventricular chamber volume that creates the systolic pressure pulse. The periodic cycle simultaneously couples the left and right heart halves propel venous blood through the pulmonary system for oxygenation while maintaining the required blood supply volumetric flow rate. There is currently no such man-made device which can actuate fluid flow as precisely as the human heart without damaging the suspended red blood cell fluid particles. As a means to introduce the concept and need of fluid flutter, a brief overview of the structural evolutions and fluid response induced by the heart is provided. There exists extensive knowledge in regards to the structure and function of the human heart. The studied literature sets forth an objective goal in creating a mechanism which can service typical cardiac blood flow requirements without violently shearing chambered blood fluid region. The linkages between the heart stress-strain relationships and the resulting fluid pressure response curves are discussed. To understand the need for such a mechanical device, one must first appreciate the complex structural dynamics and terminologies of the human heart. The introductory material is to justify the design development and analysis efforts in creating a mechanism that can give the required fluid flow response.

1.1 CARDIAC PHYSIOLOGY

The human heart is compartmentalized into four distinct muscular chambers; two atria and two ventricles. The left atrium and ventricle pumps blood from the pulmonary veins into the aorta. The right atrium and ventricle pump blood from the vena cavae to the pulmonary arteries. Separated by the inter-ventricular septum, the thin-walled muscular structures receive blood from low pressure venous systems. The tricuspid valve featured in the right-half and the mitral valve in the left, provides atrium-to-ventricle separation which permits unidirectional flow through the heart during the ventricular contraction. The aortic and pulmonary valves separate the ventricles from the arterial routing and provide a unidirectional flow path. The pressure gradient between the atrium and ventricle enacts passive valve actuation. The right and left ventricles generate blood flow and pressure through geometric contraction. Muscular fibers comprising the heart anterior cross-section shorten along the longitudinal axis, resulting in the internal transmitted force. The diastolic passive force and the systolic active force provide the total force that

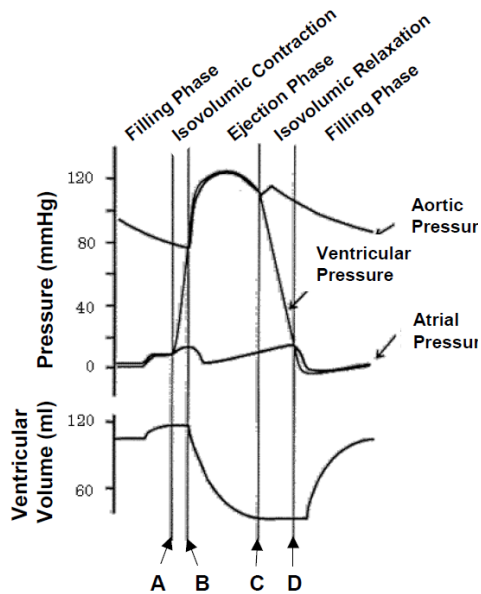


Figure 1.1.a Pressure, volume response versus time

maintains steady-state pressure from which the transient pressure periodically interjects. The muscle is stretched from the initial length, at which no force is generated, from resting end-diastolic to the peak end-systolic pressure. The ventricle is composed of such muscle fibers wrapping circumferentially around the chamber and longitudinally over the heart span. Force generated by the fibers then translates into systolic chamber pressure. End-systolic and end-diastolic pressure-volume relationships (ESPVR and EDPVR)

characterize peak systolic and end diastolic properties of the ventricular chambers. The EDPVR is nonlinear, with a steep rise in pressure initiating at 20 mmHg. The ESPVR is linear, increasing the ventricular pressure-generating capability as the ventricular volume is increased.

An approximate relationship defines the ESPVR slope with the myocardial stiffness, commonly known as the muscular elastance. Increasing muscular contractility

increases the ESPVR slope. Changes in ventricular chamber pressure cause blood to pass through the ventricle. Pressure and volume changes in the ventricle are defined as the delta ventricular volume (VV), pressure (VP), atrial pressure (AP) and aortic pressure (AoP). The cardiac cycle begins with the relaxed diastolic state at which the VP and VV are constant. An electrical activation of the heart contracts the chamber, which produces an increase in pressure. The VP rises to exceed AP and the mitral valve closes along with the aortic valve. Complete valve closure restricts blood flow in or out of the sealed control volume. This isovolumetric contraction builds pressure within the chamber. As the VP exceeds the AoP, the aortic valve opens outward and blood is ejected into the aorta as VP decreases. As the cardiac muscular contraction relaxes, VP falls below AoP and the aortic valve closes. The VP falls below the left atrium pressure, opens the mitral valve and forces blood flow from the left atrium into the left ventricle. The temporal cardiac cycle is shown in Figure 1.1.a, which gives VV and VP in the time domain. Plotting VP versus VV gives the pressure-volume diagram shown in Figure 1.1.b for the cardiac cycle. The maximum volume and minimum pressure at time A signifies systole. VP rises above AoP and the

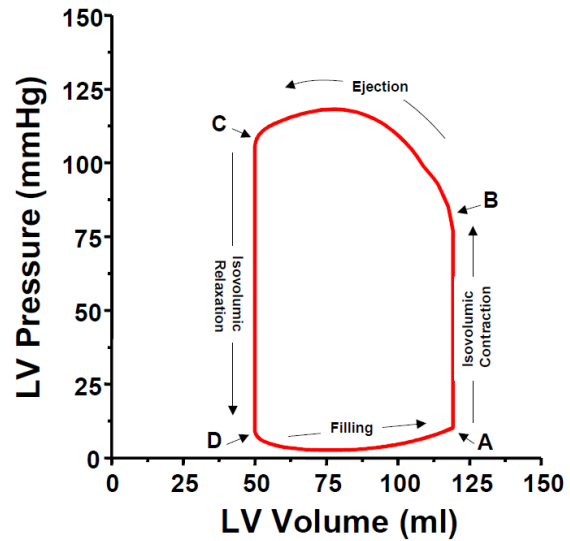


Figure 1.1.b Left ventricle cardiac pressure versus volume

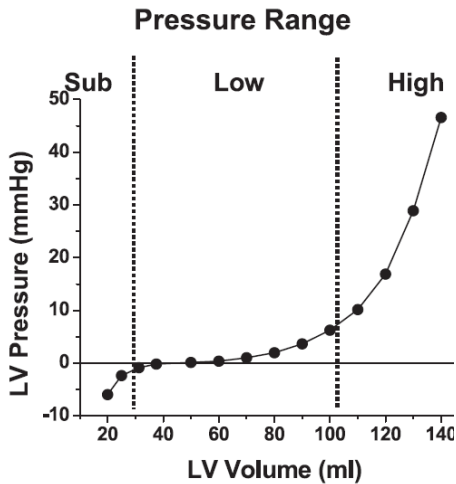


Figure 1.1.c Left ventricle pressure range

aortic valve opens at B, where ejection begins and volume decreases. Following C, VP drops below AoP and the aortic valve closes and isovolumetric relaxation continues to D. Opening of the mitral valve then allows for ventricle filling. In the muscular contraction of the ventricular wall, the chamber undergoes stiffening at the end of the systole and softening during relaxation as shown within Figure

1.1.c. The transient geometric and material vary in a periodic, yet cyclical fashion. The period of the

cardiac cycle is the interval between beats, governed in part by the oxygen demand and cellular resource requirements.

Based upon quantitative analysis, pressure and volume are related using the nonlinear function as $EDP = P_o + \beta V^\alpha$ where EDP is the end-diastolic pressure, V is the volume inside the ventricle, P_o is the pressure asymptote at low volumes, and α and β are constants which define the line curvature determined by the mechanical properties of the muscle and the structural features of the ventricle. [1] The myocardium has mechanically elastic and contractile properties that change during the cardiac cycle. The ability of the heart to fill with blood is permitted by the elastic muscular elastin fibers strain. The ventricular compliance characterizes the elastic response. The amount of blood volume that fills the ventricles for a given amount of distending pressure is the gradient of blood volume which fills the ventricle relative to the distending pressure. The ventricular filling is governed by; the pressure driving the venous blood to the atrium, the tendency of the ventricle to draw in blood upon contraction, the atrial pressure generated when the atria contraction and the mechanical compliance. The heart contractility is the

measure of force the myocardium generates during the cardiac cycle. Cardiac output is the product of the stroke volume and heart rate per minute.

Ventricular pump performance is quantified by the ejection fraction, which is the ratio of stroke volume to the end-diastolic volume. The left ventricular stroke volume is influenced by; pulmonary venous return, cardiac filling, contractility, rates and arterial resistance. The mechanical work that pumps the moving blood mass control volume through the vascular system and contributes to heat generation through frictional resistance requires external work. Energy used to open and close valves is internal, actuated by the applied fluid pressure. The total cardiac work requirement must equate to the input energy for the heart to function. Ventricular work and efficiency is highly influenced by myocardium tension, contraction velocity and the number of cardiac cycles to force blood through the vascular network. [2]

Ventricular chamber response depends on myocardial properties, muscle mass and geometry. The slope of the end-systolic myocardial stress-strain relationship is load independent and sensitive to changes in myocardial contractility with changing geometry. The EDPVR is nonlinear given the comprising structural fibers stretched through the pressure-volume ranges. In the low pressure-volume range, where there is only a small increase in pressure for a given increment in volume, the stretched fibers represent the stiffness parameter. Increasing pressure generates a corresponding increase in volume as the fiber stretch is resisted by the myocardial wall. Chamber stiffness increases as the end-diastolic pressure is increased. Passive myocardial properties are characterized by the stress and strain segment length relative to the original length. The heart is subjected to a three-dimensional state of stress that requires computation of LV wall stress and strain components in the radial, meridional and circumferential directions. Lagrangian strain is defined as $\varepsilon_L = (L - L_o)/L_o$ and the natural strain is given as $\varepsilon_N = \ln(L/L_o)$, where L_o is the stretch length at zero stress and L is the stretched length. The total Lagrangian strain is

typically used in studies of metallic materials with small deformations, whereas the natural strain is used in modeling the large deformations observed within the heart muscular contraction. [3]

The mechanical energy needed for the ventricle to change the chamber wall elastic state from a diastolic compliant level to an end-systolic stiff level is formulated using the theory of elasticity. Consider the elastic potential energy for a simple mechanical spring stretched from an initial length l_o to final length l_s . The theory of elasticity defines the mechanical strain energy of the spring at the stretched state that is equivalent to the integration of force as a function of spring length and displacement. The ventricular wall spring stiffness is time-varying, introducing mechanical nonlinearity in the force versus deflection response. [4] There is no mechanical work performed on the time-varying spring from external forces; rather, the potential energy is produced by the increase in spring stiffness. The amount of energy required by the ventricle is equivalent to the amount of mechanical work the elastic chamber can impart to the outside when its volume decreases from the point B to C shown in Figure 1.1.b.

1.2 CARDIAC STRUCTURE & FUNCTION

The action potential within the cardiac muscle is generated by coordinated actions of activation and voltage-gated ion channels. These specialized cells impart the rapid voltage-dependent changes in ion permeability which render the dynamic membrane elastic potential. The rhythmic contraction originates spontaneously in the conducting system and the impulse travels to different regions of the heart. The left and right atriums cycle in coincidence followed by simultaneous ventricular contraction. The impulse passage lag permits time for the atria to empty blood into the ventricular chamber prior to contraction. The cardiac impulse begins at the sinoatrial node, which generates sinoatrial node generates an electrical excitation impulse that spreads across the left and right atriums, contracting first the right side in nearest proximity. The excitation activates the atrioventricular node, which precedes the ventricular impulse that

contracts the myocardium and pumps the blood into the pulmonary artery and aorta through the ventricles. This excitation is controlled by the sympathetic nervous system and the vagus nerve of the parasympathetic nervous system.[5]

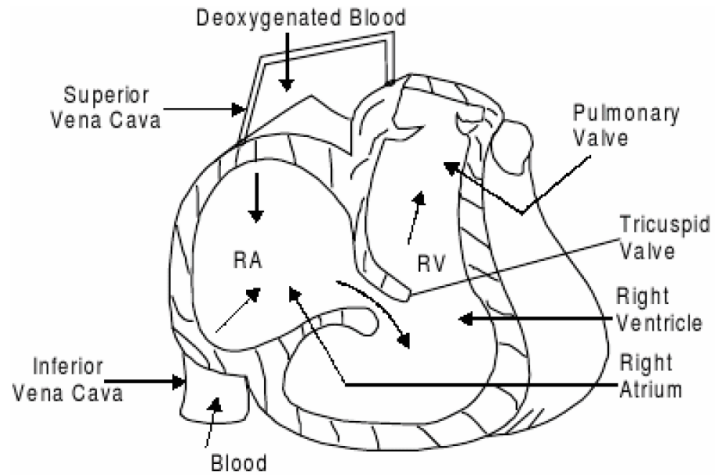


Figure 1.2.a Cardiac structure

The amount of blood ejected from the heart per minute is defined as the cardiac output. The product of stroke volume and heart rate is used to compute the volumetric cardiac output. The average adult ranges from 5 L/min at rest to nearly 20 L/min during strenuous exercise. The stroke volume is the blood ejected in one ventricular contraction, given the amount of external energy that is expended as stroke work. The heart contractility forces blood from within the chamber and achieves the required volumetric displacement. The end-diastolic volume and pressure defines the respective volume and pressure in the ventricle immediately preceding contraction. The end-systolic volume defines the volumetric displacement of blood remaining in the ventricle immediately after contraction. The central venous pressure represents the pressure of blood in the veins entering the right atrium. Venous return is the volume of blood returning to the heart right side in one minute. The ejection fraction is the proportion of the end-diastolic volume that is ejected during systole. The mechanical stroke volume is influenced by the preload, afterload and contractility. Preload is the degree of ventricular stretch at the end of diastole, determined by the end-diastolic volume. Increasing the end-diastolic volume requirement also increases the mechanical preload in displacing said fluid volume. Afterload is the force or stress

imparted during systole with which the force against the ventricle must contract. The resistance to outflow from the ventricle affects the relative magnitude of the required afterload.

The energy released during contraction is a function of the initial fiber length. Stretching the heart by preload filling provides the energy released by contraction. The initial stretch of the ventricular myocardium preload is produced by the end-diastolic volume. The relationship between the end-diastolic pressure and end-diastolic volume is nearly linear up until filling pressures generate excessive fiber stretch. This relationship then becomes nonlinear as the end-diastolic pressure is exceeded. Additional increase in the end-diastolic pressure decreases stroke volume. An increase in preload provides an increase in cardiac output; wherein increasing the right ventricular end-diastolic preload pressure increases the initial stretch of the right ventricular myocardium. The force of contraction controls the right ventricular stroke volume and the left ventricle filling and end-diastolic volume. Increasing the force of contraction increases the left ventricle stroke volume and reduces afterload. [6]

The time-varying mechanical compliance intrinsic to the human heart makes for a fitting application to the proposed fluid motion mechanism. The cardiovascular system is a closed, continuous hydraulic system that features suspended plasma and red blood cell corpuscles. For each cubic millimeter of blood, there exist approximately 5 million red blood cells that flow freely through the closed loop. The circulation of blood is maintained within the blood vessels by an applied rhythmic pressure exerted by the heart contraction and expansion. The pumping action is induced by a nonlinear elastic muscular contraction to force blood through the vascular network. The blood circulates oxygenated red blood cells to deliver oxygen to cell tissue while simultaneously looping deoxygenated blood through the lungs in a continuous fluid loop. Starting at the left atrium as shown within Figure 1.2.a, blood flows to the aortic valve through the left ventricle entering at the aorta to deliver oxygenated blood to tissue cells. Blood then returns following oxygen depletion to the right atrium where it is forced through the semilunar valve and

the right ventricle and pulmonary valves to the lungs for oxygen enrichment. The process is repeated with an average cyclic of 0.8 seconds between each successive beat. The heart is a pair of two stage pumps that work in series and are arranged in a parallel configuration. Blood passes through the first stage to the second stage in series, reciprocating fluid motion to the neighboring chamber. The right side pumps blood to the lungs and maintains decreased pressure amplitudes as shown within Figure 1.2.b to that of the left side pumps, which deliver blood to the cell tissue requiring oxygenated blood. The left side experiences a high resistance circuit with a large pressure gradient between the arteries and veins. This increased resistance requires greater muscular contraction to overcome such fluid flow obstructions. The volume of blood that is displaced by each side is equivalent as the pumps work in series, though the pressure amplitudes need not be identical.

Deoxygenated blood enters the right atrium and when the chamber is full, then undergoes contraction which forces blood through the tricuspid valve into the right ventricle. The tricuspid valve closes following the right ventricle contraction and the chamber pressure forces the semilunar pulmonary valve to open to permit blood flow into the lungs. Oxygenated blood enters the left atrium and blood is pumped through the left ventricle mitral valve by the contraction of the left atrium muscles. As the left

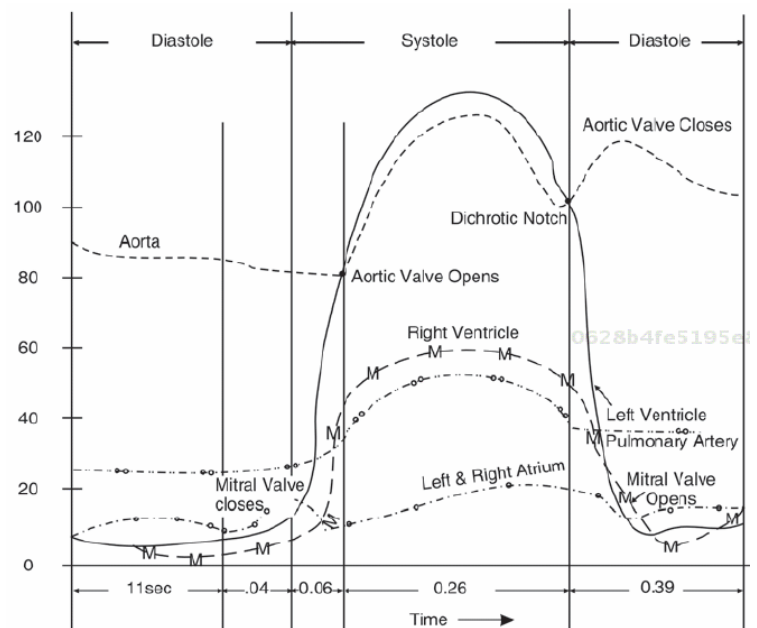


Figure 1.2.b Pressure as a function of time at cardiac stages

ventricular muscles contract, pressure increases and closes the mitral valve. The increase in pressure reaches a set point which prompts the aortic valve to open and blood to flow into the aorta. The outward flowing of blood from the right and left heart is passive and highly synchronized. The heart walls are composed of a thick layer of cardiac muscle known as the myocardium. Dividing the left and right atrial portions is a thin interatrial septum wall. The thicker intraventricular septum bisects the right and left ventricular portions to generate the required pressure amplitudes to force blood from chamber. The right ventricle is connected with the right atrium through the atrioventricular orifice gated by the tricuspid valve, which itself is a three cusped passively compliant actuating valve. The right ventricle is connected to the pulmonary artery through the pulmonary orifice gated by the pulmonary valve, which itself features three semilunar cusps. The left atrium is connected to the left ventricle through the atrioventricular orifice that is gated by the mitral valve. The left ventricle is connected to the aorta through the aortic orifice which is gated by the three cusped aortic valves. Displaced blood is approximately 0.07 L/beat, or 70 mL for each rhythmic cardiac beat. Blood is characteristically a non-Newtonian fluid that does not follow the linear shear stress and deformation rate relationship. The blood flow is nearly laminar through the blood vessels; however, as the blood exits the aorta there is a fraction of blood which undergoes transition to turbulent flow regime. [7]

1.3 DEVELOPMENT OF THE ARTIFICIAL HEART – A PRIORI ART

Each year over 400,000 new cases of congestive heart failure are diagnosed in the United States alone. With a 75 percent mortality rate, it is often necessary that the patient receive a cardiac transplantation to replace the damaged heart. Aside from donor transplantation, there exist two primary options considered to replicate the pumping action of the heart; the ventricular-assist device (VAD) and the total artificial heart (TAH). These devices severely alter the patient mobility and lifestyle, compromising both quantity and quality of life. The LV pumps blood

throughout the entire body and is susceptible to increased damage beyond that of the RV supply through the lungs alone. As such, the LV requires pressure amplitudes and mass flow magnitudes that exceed RV chamber requirements.

The VAD features the diseased native heart aided by a mechanical blood pump to circulate blood or by an aortic installed balloon to increase distending diastolic pressure. Instead of replacing the complete heart, unhurt portions of the heart are coupled with the VAD. Diastolic blood pressure is artificially increased to aid in the required systolic pressure requirements achieved by the myocardium contraction. The TAH is a complete replacement of the native heart with a mechanical pump to force fluid through the venous and arterial circulatory passages. There exists three viable classifications for mechanical blood pumps capable of transplantation, which include; pulsatile sacks, reciprocating piston pump and centrifugal impeller pumps.

Pulsatile sacks feature flexible diaphragms compressed and released in a periodic manner to generate the blood pressure pulsation. The intra-aortic balloon counter-pulsation device is designed to improve balance between myocardial oxygen supply and demand. Placed in the thoracic aorta, the device inflates and deflates to assist the left ventricular contraction by reducing the afterload of cardiac work. These temporary devices are limited to in-hospital care and are not portable.

Implantable blood pumps that feature a piston-type design to replace the damaged heart use a pneumatic or electrically driven piston in displacing blood through a linear volumetric stroke. These devices are limited by the linear cylinder actuation diameter size, the duplicitous mechanical valves opening and closing simultaneously to permit blood flow, active control system feedback implementation and limited systematic coupling between structural fiber and volumetric displacement. That is to say, the piston-style pump works well in applications for which it was originally designed; namely, the control of heavy equipment at steady-state high flow conditions but not for mimicking blood flow rate through the body. This type of device is

inherently flawed in achieving the delicate motion of fluid particles in a highly coupled structural mechanism such as the human heart.

Centrifugal pumps force intake blood flow through an axially driven impeller that generates a centrifugal acceleration of fluid particles. The blood exits the pump with an increased velocity and is decelerated to increase static blood pressure. This type of device provides a continuous, non-pulsatile flow and maintains fluid system pressure without the non-linear pressure volume profile shown within Figure 1.1.c. The impeller pump generates rapid acceleration and deceleration of the fluid particles that exert fluid particle shear stresses along the blade. [8] The outer blade edges move at high speeds, damaging blood red cells through the uncontrolled shearing. The damaged red blood cells and high shear activate platelets in coagulation on the device surfaces. Also, as activated platelets navigate through narrow blood vessels, then can lodge within vessels within the brain leading to stroke or in the kidneys resulting in renal failure. While the centrifugal pump is adequate for the applications to which it was originally designed, it fails to meet the criteria required in the gentle fluttering of fluid particles as provided by the human heart. The current-state devices are inherently flawed in replicating the delivery of blood flow throughout the body. To achieve typical cardiac fluid flow response, it is required that an alternative design be created.

2 CONSTITUTIVE FLUID DYNAMICS

2.1 GOVERNING FLUID CONSERVATION PRINCIPLES

The motion of fluid particles within a hydraulic control system is governed by the Navier-Stokes equation;

$$\rho \left(\frac{\partial \vec{v}}{\partial t} + v \nabla \vec{v} - \vec{f} \right) = -\nabla p + \mu \nabla^2 \vec{v} \quad (2.1.1)$$

Where ρ is the fluid density, \vec{v} is the velocity vector of the fluid, t is time, \vec{f} is a vector featuring all body forces acting on the fluid, p is the fluid pressure and μ is the fluid viscosity.

This relationship governs the fluid particle or element through the flow field. The Reynolds transport theorem characterizes the influence of fluid on the control volume. For a simple control volume, flow entering and exiting the control volume at different locations can be derived with a system of particles to give the conservation of mass.

$$\frac{dm}{dt} = \frac{\partial}{\partial t} \int_{c.v.} \rho dV + \int_{c.v.} \rho (\vec{v} \cdot \vec{n}) dA \quad (2.1.2)$$

Where m is the control volume mass, \vec{v} is the velocity vector of flow entering and exiting the control volume and \vec{n} is the unit vector orthogonal to the control volume fluid boundary surface. The conservation of fluid momentum describes the time rate of change observed in the fluid momentum.

$$\frac{d\vec{p}}{dt} = \frac{\partial}{\partial t} \int_{c.v.} \rho \vec{v} dV + \int_{c.v.} \rho \vec{v} (\vec{v} \cdot \vec{n}) dA \quad (2.1.3)$$

Where \vec{p} the fluid momentum is vector, and \vec{v} is the fluid velocity vector. Newton's second law states that the time rate of change of fluid momentum is equivalent to the net force acting on the control volume.

$$\vec{F} = \frac{\partial}{\partial t} \int_{c.v.} \rho \vec{v} dV + \int_{c.v.} \rho \vec{v} (\vec{v} \cdot \vec{n}) dA \quad (2.1.4)$$

Where the vector force \vec{F} acts on the control volume, [9] \vec{F} is decomposed into body forces exerted on the fluid region and the surface forces exerted by the interior surface of the control volume.

$$\vec{F} = \vec{f}_s + \vec{f}_b \quad (2.1.5)$$

Let the fluid velocity vector \vec{v} be decomposed into the components (u, v, w) in the (x, y, z) Cartesian coordinates. Substitution into the conservation of linear momentum equations then gives the vector forms,

$$\frac{\partial(\rho u)}{\partial t} + \frac{\partial(\rho u^2)}{\partial x} + \frac{\partial(\rho uv)}{\partial y} + \frac{\partial(\rho uw)}{\partial z} = \vec{f}_{x,s} + \vec{f}_{x,b} \quad (2.1.6)$$

$$\frac{\partial(\rho v)}{\partial t} + \frac{\partial(\rho vu)}{\partial x} + \frac{\partial(\rho v^2)}{\partial y} + \frac{\partial(\rho vw)}{\partial z} = \vec{f}_{y,s} + \vec{f}_{y,b} \quad (2.1.7)$$

$$\frac{\partial(\rho w)}{\partial t} + \frac{\partial(\rho wu)}{\partial x} + \frac{\partial(\rho wv)}{\partial y} + \frac{\partial(\rho w^2)}{\partial z} = \vec{f}_{z,s} + \vec{f}_{z,b} \quad (2.1.8)$$

$$\vec{f}_{x,s} = \frac{\partial(\tau_{xx})}{\partial x} + \frac{\partial(\tau_{xy})}{\partial y} + \frac{\partial(\tau_{xz})}{\partial z} \quad (2.1.9)$$

$$\vec{f}_{y,s} = \frac{\partial(\tau_{yx})}{\partial x} + \frac{\partial(\tau_{yy})}{\partial y} + \frac{\partial(\tau_{yz})}{\partial z} \quad (2.1.10)$$

$$\vec{f}_{z,s} = \frac{\partial(\tau_{zx})}{\partial x} + \frac{\partial(\tau_{zy})}{\partial y} + \frac{\partial(\tau_{zz})}{\partial z} \quad (2.1.11)$$

In addition to the conservation of mass and momentum, the conservation of energy must be satisfied.

$$\frac{dE}{dt} = \frac{dQ}{dt} + \frac{dW}{dt} \quad (2.1.12)$$

$$\frac{dE}{dt} = \frac{\partial(\rho e)}{\partial t} + \frac{\partial(\rho ue)}{\partial x} + \frac{\partial(\rho ve)}{\partial y} + \frac{\partial(\rho we)}{\partial z} \quad (2.1.13)$$

$$\begin{aligned} \frac{dQ}{dt} + \frac{dW}{dt} = & \frac{\partial(q_x + u\tau_{xx} + v\tau_{xy} + w\tau_{xz})}{\partial x} + \\ & \frac{\partial(q_y + u\tau_{yx} + v\tau_{yy} + w\tau_{yz})}{\partial y} + \frac{\partial(q_z + u\tau_{zx} + v\tau_{zy} + w\tau_{zz})}{\partial z} \end{aligned} \quad (2.1.14)$$

Where E is the total Lagrangian internal, kinetic and potential energy of the system, Q is the heat addition to the control volume and W is the work applied to the control volume. In the constitutive equations, the blood is assumed to behave as a continuous and incompressible fluid.

2.2 INCOMPRESSIBLE NEWTONIAN LAMINAR FLUID FLOW

The transient Newtonian scenario in which the flow is forced by the applied pressure gradients and body forces are derived using the conservation of mass for incompressible fluid,

$$\frac{\partial \rho}{\partial t} = \frac{\rho}{K} \frac{\partial p}{\partial t} \quad (2.2.1)$$

Where K is the bulk modulus, ρ defines the density and P the pressure. For the incompressible Newtonian case, density is assumed as constant which eliminates the left-hand side term. This simplifies the computation and reduces numerical runtime in obtaining a solution.

The conservation of momentum is written in general for i^{th} cell volume as,

$$\frac{\partial U_i}{\partial t} = -\frac{\partial}{\partial x_j}(\rho u_j u_i) + \frac{\partial \tau_{ij}}{\partial x_j} - \frac{\partial p}{\partial x_i} + \rho g_i \quad (2.2.2)$$

Conservation of energy can be solved independently, neglecting temperature and heat generation terms,

$$\frac{\partial(\rho E)}{\partial t} = -\frac{\partial}{\partial x_j}(u_j \rho E) - \frac{\partial}{\partial x_j}(u_j p) + \frac{\partial}{\partial x_i}(\tau_{ij} u_j) + \rho g_i u_i \quad (2.2.3)$$

Where u_i defines the velocity components, E is the specific energy, ρg_i gives the body force and τ_{ij} are the deviatoric stress components defined as,

$$\tau_{ij} = \mu \left(\frac{\partial u_i}{\partial x_j} + \frac{\partial u_j}{\partial x_i} - \frac{2}{3} \delta_{ij} \frac{\partial u_k}{\partial x_k} \right) \quad (2.2.4)$$

Material balance over stationary fluid volume $\Delta x_1 \Delta x_2 \Delta x_3$ gives the accumulation equivalent to the inward less the outward bound transport,

$$\begin{aligned}
\Delta x_1 \Delta x_2 \Delta x_3 \frac{\partial \rho}{\partial t} &= \Delta x_2 \Delta x_3 [(\rho U_1)|_{x_1} - (\rho U_1)|_{x_1 + \Delta x_1}] \\
&+ \Delta x_1 \Delta x_3 [(\rho U_2)|_{x_2} - (\rho U_2)|_{x_2 + \Delta x_2}] \\
&+ \Delta x_1 \Delta x_2 [(\rho U_3)|_{x_3} - (\rho U_3)|_{x_3 + \Delta x_3}]
\end{aligned} \tag{2.2.5}$$

The formulation corresponds to the continuity equation finite-volume formulation for a hexahedral mesh. Dividing through by the common denominator then gives the originating continuity equation in the three spatial dimensions,

$$\frac{\partial \rho}{\partial t} + \frac{\partial \rho U_1}{\partial x_1} + \frac{\partial \rho U_2}{\partial x_2} + \frac{\partial \rho U_3}{\partial x_3} = 0 \tag{2.2.6}$$

Representing the continuity equation in tensor notation for j is 1, 2 and 3 then gives,

$$\frac{\partial \rho}{\partial t} + \frac{\partial \rho U_1}{\partial x_1} = 0 \tag{2.2.7}$$

Combining the continuity equation with the momentum equation then gives the Poisson equation of pressure for constant density and viscosity,

$$\frac{\partial}{\partial x_i} \left(\frac{\partial P}{\partial x_i} \right) = - \frac{\partial}{\partial x_i} \left[\frac{\partial (\rho U_i U_j)}{\partial x_j} \right] \tag{2.2.8}$$

The Navier-stokes equations are used to define velocity and pressure, introducing pressure as a dependent variable per the Poisson equation. The change in volumetric fluid flow is governed by the continuity equation and the velocity gradient for density,

$$\frac{\partial \rho}{\partial t} = -(\nabla \cdot \rho U) \tag{2.2.9}$$

The momentum equation can then be formulated to compute velocity field within the fluid region, characterizing fluid flow response that moves in the direction of flow,

$$\frac{\partial \rho}{\partial t} + \frac{\partial \rho U_1}{\partial x_1} + \frac{\partial \rho U_2}{\partial x_2} + \frac{\partial \rho U_3}{\partial x_3} = \rho \left(\frac{\partial U_1}{\partial x_1} + \frac{\partial U_2}{\partial x_2} + \frac{\partial U_3}{\partial x_3} \right) \tag{2.2.10}$$

Change in momentum in each direction is balanced by the forces acting in said direction.

Balancing momentum of velocity component in the x_i direction is defined as,

$$\begin{aligned}
\Delta x_1 \Delta x_2 \Delta x_3 \frac{\partial \rho U_1}{\partial x_1} &= \Delta x_2 \Delta x_3 [(\rho U_1 U_1)|_{x_1} - (\rho U_1 U_1)|_{x_1+\Delta x_1}] - \tau_{11}|_{x_1} \\
&+ \tau_{11}|_{x_1+\Delta x_1} + \Delta x_1 \Delta x_3 [(\rho U_2 U_1)|_{x_2} - (\rho U_2 U_1)|_{x_2+\Delta x_2}] \\
&- \tau_{21}|_{x_2} + \tau_{21}|_{x_2+\Delta x_2} \\
&+ \Delta x_1 \Delta x_2 [(\rho U_3 U_1)|_{x_3} - (\rho U_3 U_1)|_{x_3+\Delta x_3}] - \tau_{31}|_{x_3} \\
&+ \tau_{31}|_{x_3+\Delta x_3} + \Delta x_1 \Delta x_2 \Delta x_3 \rho g_1
\end{aligned} \tag{2.2.11}$$

Where τ defines the momentum transported into the fluid volume at x , the corresponding finite-volume formulation of momentum equations for hexahedral mesh by dividing through by common denominator $\Delta x_1 \Delta x_2 \Delta x_3$ then gives Navier-Stokes equations in three dimensions,

$$\frac{\partial U_1}{\partial t} + U_1 \frac{\partial U_1}{\partial x_1} + U_2 \frac{\partial U_1}{\partial x_2} + U_3 \frac{\partial U_1}{\partial x_3} = -\frac{1}{\rho} \frac{\partial P}{\partial x_1} + \frac{1}{\rho} \frac{\partial \tau_{11}}{\partial x_1} + \frac{1}{\rho} \frac{\partial \tau_{21}}{\partial x_2} + \frac{1}{\rho} \frac{\partial \tau_{31}}{\partial x_3} + g_1 \tag{2.2.12}$$

$$\frac{\partial U_2}{\partial t} + U_1 \frac{\partial U_2}{\partial x_1} + U_2 \frac{\partial U_2}{\partial x_2} + U_3 \frac{\partial U_2}{\partial x_3} = -\frac{1}{\rho} \frac{\partial P}{\partial x_2} + \frac{1}{\rho} \frac{\partial \tau_{21}}{\partial x_1} + \frac{1}{\rho} \frac{\partial \tau_{22}}{\partial x_2} + \frac{1}{\rho} \frac{\partial \tau_{32}}{\partial x_3} + g_2 \tag{2.2.13}$$

$$\frac{\partial U_3}{\partial t} + U_1 \frac{\partial U_3}{\partial x_1} + U_2 \frac{\partial U_3}{\partial x_2} + U_3 \frac{\partial U_3}{\partial x_3} = -\frac{1}{\rho} \frac{\partial P}{\partial x_3} + \frac{1}{\rho} \frac{\partial \tau_{13}}{\partial x_1} + \frac{1}{\rho} \frac{\partial \tau_{23}}{\partial x_2} + \frac{1}{\rho} \frac{\partial \tau_{33}}{\partial x_3} + g_3 \tag{2.2.14}$$

Rewriting the equations in summation form,

$$\frac{\partial U_i}{\partial t} + \sum_j U_j \frac{\partial U_i}{\partial x_j} = -\frac{1}{\rho} \frac{\partial P}{\partial x_i} + \sum_j \frac{1}{\rho} \frac{\partial \tau_{ji}}{\partial x_j} + g_i \tag{2.2.15}$$

Equivalently, the tensor notation form is written for the three equations as,

$$\frac{\partial U_i}{\partial t} + U_j \frac{\partial U_i}{\partial x_j} = -\frac{1}{\rho} \frac{\partial P}{\partial x_i} + \frac{1}{\rho} \frac{\partial \tau_{ji}}{\partial x_j} + g_i \tag{2.2.16}$$

For a Newtonian fluid with incompressible flow and constant ρ and ν , the tensor form of Navier-Stokes three dimensional equations is defined as,

$$\frac{\partial U_i}{\partial t} + U_j \frac{\partial U_i}{\partial x_j} = -\frac{1}{\rho} \frac{\partial P}{\partial x_i} + \nu \frac{\partial}{\partial x_j} \left(\frac{\partial U_i}{\partial x_j} + \frac{\partial U_j}{\partial x_i} \right) + g_i \tag{2.2.17}$$

The Navier-Stokes equations are limited to macroscopic conditions which govern the specified control volume region. Summation over the three dimensional space for $j = 1, 2, 3$ where the i^{th} term is present within each of the three constitutive momentum equations. [10] In addition to continuity and momentum equations used in mass transport of fluid medium, the

energy transport theorem is included within the computational model. Energy exists as kinetic, thermal, chemical and potential forms within the physical system. Only the kinetic and potential energies are included when characterizing the fluid-structural interaction response as the effects of thermal and chemical energies are comparatively negligible.

$$T = K + V \quad (2.2.18)$$

Given the known relationship for kinetic and potential energies,

$$T = \frac{1}{2} \rho U_i U_i + \rho g_i x_i \quad (2.2.19)$$

Differentiating the energy and momentum transport equation then gives the balance for kinetic and potential energy equation,

$$U_i \frac{\partial U_i}{\partial t} + U_i U_j \frac{\partial U_i}{\partial x_j} = -\frac{1}{\rho} U_i \frac{\partial P}{\partial x_i} + \frac{U_i}{\rho} \frac{\partial \tau_{ij}}{\partial x_j} + U_i g_i \quad (2.2.20)$$

Substituting for e as the scalar magnitude of j^{th} component $e = \frac{1}{2} (U_1^2 + U_2^2 + U_3^2)$ the simplification is made to the above equation,

$$\frac{\partial e}{\partial t} + U_j \frac{\partial e}{\partial x_j} = -\frac{1}{\rho} U_i \frac{\partial P}{\partial x_i} + \frac{1}{\rho} U_i \frac{\partial \tau_{ij}}{\partial x_j} + U_i g_i \quad (2.2.21)$$

Expanding the equation through summation over i and j , multiplying by fluid density and using separation of variable to parse out the mixed derivatives,

$$\rho \frac{\partial e}{\partial t} = -U_j \frac{\partial e}{\partial x_j} + P \frac{\partial U_i}{\partial x_i} - \frac{\partial(PU_i)}{\partial x_i} + \frac{\partial(\tau_{ij}U_i)}{\partial x_i} - \tau_{ij} \frac{\partial U_i}{\partial x_i} + \rho g U_i \quad (2.2.22)$$

Boundary conditions for the three-dimensional Navier-Stokes equations feature dependent variables $\{U_1 U_2 U_3 P\}$ which influence the simulation results. The inlet, outlet and wall conditions provide the boundary response along the fluid region control volume periphery. Inlet velocity is defined in terms of vector or scalar velocities or mass flow rate. Pressure inlet boundary conditions can be used when inlet pressure is known without information regarding the flow rate, regardless of whether fluid is entering or leaving the region. The standard outlet

boundary condition is zero-diffusion flux condition applied at outflow cells; extrapolating conditions at the outflow plane from within the domain.

$$\phi|_{L-} = \phi|_{L+} \quad (2.2.23)$$

Pressure outlet boundary condition defines the static pressure at flow outlets, resulting in increased convergence rate when backflow occurs during solving iteration. Pressure outflow is utilized when more than one outflow occurs within the specified fluid region. The wall boundaries for velocity assume a no-slip condition; hence, the relative velocity between the wall and fluid is zero for any specified wall surface along fluid region periphery. The Navier-Stokes equations are nonlinear, it is then required that an initial guess from which the solver can begin the equilibrium iterations is accurate. Providing initial conditions near that of the equilibrated solution increases convergence rate and can significantly reduce computational run time. Transient simulations are less vulnerable to poorly prescribed initial conditions as exact initial conditions are often unnecessary and large time step incrementation is permitted.

3 STRUCTURAL MECHANICS

3.1 GOVERNING EQUATIONS OF MOTION

A simple second order mathematical model capable of simulating the mechanical response coupling fluid dynamics with the structural displacement requires mass, damping and stiffness parameters.

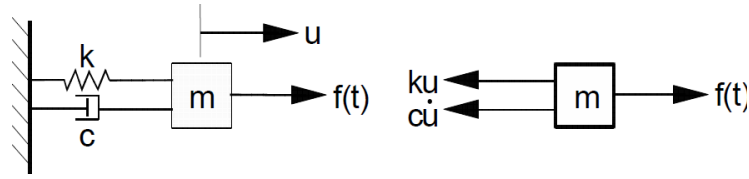


Figure 3.1.a Second order conceptual model

$$[M]\{\ddot{x}\} + [C]\{\dot{x}\} + [K]\{x\} = F\{t\} \quad (3.1.1)$$

Where $[M],[C],[K]$ are the mass, damping and stiffness matrices of the structural dynamic model. The extended Hamilton principle is used to derive the governing equations and the boundary conditions.

$$\int_{t_1}^{t_2} [\delta W_{nc} - \delta \Pi + \delta T] dt = 0 \quad (3.1.2)$$

$$\delta W_{nc} = \int_V \{\delta u\}^T \{g\} dV + \int_S \{\delta u\}^T \{f\} dS + \{\delta D\}^T \{Q\} \quad (3.1.3)$$

$$\delta \Pi = \int_V \{\delta \varepsilon\}^T \{\sigma\} dV = \int_V \{\delta \varepsilon\}^T [Q] \{\varepsilon\} dV \quad (3.1.4)$$

$$\delta T = - \int_V \{\delta u\}^T \rho \{\ddot{u}\} dV \quad (3.1.5)$$

Where Π is the elastic potential energy, T the kinetic, p the momentum and δW_{nc} the non-conservative work which includes body, surface and concentrated forces and $\{\sigma\} = [Q]\{\varepsilon\}$. In the biological tissue of the human heart, nonlinearity arises given the time dependent changes of position, geometry and material stiffness. To accurately model the behavioral response

of $[M]$, $[C]$ and $[K]$ it is required that nonlinearity be incorporated within the structural model. A nonlinear static model gives the bifurcated static deformation buckling load and the nonlinear dynamic model is used to generate the nodal velocity and accelerations which govern the periodic structural cycling. Modified Riks Method is used to model the geometric stiffness and buckling deflections along with the Newmark- β Method to model the implicit nonlinear dynamic structural analysis.

3.2 ELASTIC DEFORMATION & STRAIN

Material particle is initially located at position X in space which then is transitioned to an updated position x by the applied loading. This deformation correspondence is used to define the history of said particle through time as,

$$x = x(X, t) \quad (3.2.1)$$

For two neighboring particles, located at X and at $X + dX$ in the initial configuration, the current configuration then must be updated as,

$$dx = \frac{\partial x}{\partial X} dX \quad (3.2.2)$$

Mapped to the above equation then gives the deformation gradient matrix defined as,

$$dx = F \cdot dX \quad (3.2.3)$$

Material behavior is dependent upon material strain, which is retracted from the gross rigid body motion. An infinitesimal length dX from the particle at X , gives the initial and current lengths are measured as,

$$dL^2 = dX^T \cdot dX \quad (3.2.4)$$

$$dl^2 = dx^T \cdot dx \quad (3.2.5)$$

The nominalized infinitesimal gauge length is then defined as

$$\lambda = \frac{dl}{dL} = \sqrt{\frac{dx^T}{dX^T} \cdot \frac{dx}{dX}} \quad (3.2.6)$$

3.3 EQUILIBRIUM & VIRTUAL WORK

The exact solution requires that both force and moment equilibrium be maintained at all times over the body volume. Displacement finite element method is based upon approximating this equilibrium requirement as an average over a finite number of volumetric divisions. The exact equilibrium equations and the form of virtual work used in the finite element models are provided. Consider a volume V which occupies part of a body in the current configuration where S is the bounded surface encasing said volume. Let surface traction at any point on S be the force t per unit of current area and let the body force at any point within the material volume be f . The force equilibrium for the featured volume can then be defined as,

$$\int_S t dS + \int_V f dV = 0 \quad (3.3.1)$$

The Cauchy stress matrix σ at a point S is defined by,

$$t = n \cdot \sigma \quad (3.3.2)$$

For n as the unit outward normal to S at the point,

$$\int_S (n \cdot \sigma) dS + \int_V f dV = 0 \quad (3.3.3)$$

Rewriting surface integral as a volume integral in accordance with Gauss's theorem,

$$\int_S (n \cdot \sigma) dS = \int_V \left[\left(\frac{\partial}{\partial x} \right) \cdot \sigma \right] dV \quad (3.3.4)$$

The differential equation of translational equilibrium is given,

$$\left(\frac{\partial}{\partial x} \right) \cdot \sigma + f = 0 \quad (3.3.5)$$

The derived force equilibrium differential equations provide no approximation with respect to deformation or rotation magnitude. These equations represent an exact statement of equilibrium given that the definitions for surface traction, body forces, stress, volume and area are precise. The moment equilibrium is defined by taking moments about the origin,

$$\int_S (x \times t) dS + \int_V (x \times f) dV = 0 \quad (3.3.6)$$

Using Gauss's theorem then gives the result that the Cauchy stress matrix must be symmetric,

$$\sigma = \sigma^T \quad (3.3.7)$$

At each point there exist six independent components for the tri-axial state of stress. The three force equilibrium equations are replaced by an equivalent weak form representation. This single scalar equation over the entire body is obtained by multiplying the point-wise differential equations by an arbitrary vector-valued test or shape function, which maintains continuity across the entire volume and then integrating. The test function is a virtual velocity field δv , which is arbitrarily selected to obey kinematic continuity constraints. The dot product with the virtual velocity field for a single scalar equation at each material point is then integrated over the body which gives,

$$\int_V \left[\left(\frac{\partial}{\partial x} \right) \cdot \sigma + f \right] \cdot \delta v dV = 0 \quad (3.3.8)$$

Through use of the chain rule and Gauss's theorem the above can then be expanded as,

$$\int_S (t \cdot \delta v) dS + \int_V (f \cdot \delta v) dV = \int_V \sigma : \left(\frac{\partial \delta x}{\partial x} \right) dV \quad (3.3.9)$$

Simplifying the virtual work equation to the traditional form in substituting traction, force and Cauchy stress

$$\int_V (\sigma : \delta D) dV = \int_S (\delta v \cdot t) dS + \int_V (\delta v \cdot f) dV \quad (3.3.10)$$

The rate of work done by the external forces subjected to any virtual velocity field is equal to the equilibrating stress on the rate of deformation for given virtual velocity field. The principle of virtual work is the weak form of the equilibrium equations used as the basic equilibrium statement for finite element formulation. Approximations are introduced in choosing

the test or shape functions for the virtual velocity field, wherein the variation is restricted to a finite number of discretized elements.

3.4 NONLINEAR SOLUTION METHODS

The equilibrium equations obtained by discretizing virtual work are symbolically defined as,

$$F^N(u^M) = 0 \quad (3.4.1)$$

Where F^N gives the force components conjugate to the N^{th} variable in the problem and u^M is the value of the M^{th} variable. Newton's method numerical approach is used to solve the nonlinear equilibrium equations, improving convergence rate for the nonlinear type problems. The formulation of Newton's method assumes that after iteration i , an approximation u_i^M to the solution is obtained. Then, let c_{i+1}^M be the difference between approximate solution and the exact solution to the discrete equilibrium equation.

$$F^N(u_i^M + c_{i+1}^M) = 0 \quad (3.4.2)$$

Expanding this equation in a Taylor series approximate solution, where u_i^M is defined as a reasonably close approximation to the solution and the magnitude of c_{i+1}^M gives a linear system of equations,

$$K_i^{NP} c_{i+1}^p = -F_i^N \quad (3.4.3)$$

The Jacobian matrix is expressed by,

$$K_i^{NP} = \frac{\partial F^N}{\partial u^p}(u_i^M) \quad (3.4.4)$$

$$F_i^N = F^N(u_i^M) \quad (3.4.5)$$

The next iterate approximation to the exact solution is then,

$$u_{i+1}^M = u_i^M + c_{i+1}^M \quad (3.4.6)$$

In dynamic analysis when implicit integration is used, automatic time stepping is based on the concept of half-increment residuals. The time stepping operator defines the velocities and

accelerations at the end of the step ($t + \Delta t$). Equilibrium is established at ($t + \Delta t$), which assures equilibrium solution at the end of each time step and at the beginning and end of individual time steps. Equilibrium solutions do not guarantee equilibrium throughout the attempted time step increment. The time step control is based on measuring the equilibrium error at some point during the time step; using the integration operator combined with the solution obtained at ($t + \Delta t$) to interpolate with the ongoing time step. If the maximum entry in this residual vector is greater than the inputted tolerance, the time step is too large and is reduced for dynamic solver methods. If the maximum half-increment residual is less than the inputted tolerance, the time step is increased for the next increment. Automated numerical solvers reduce computational run time and expedite the solution process.

3.5 IMPLICIT DYNAMIC ANALYSIS

The equilibrium equation for the dynamic analysis procedure begins with the d'Alembert force, where the body force f is defined as an externally applied body force F and a d'Alembert force.

$$f = F - \rho \ddot{u} \quad (3.5.1)$$

Where ρ is the material density at the node, and u is the nodal displacement in the equation, the body force term in the virtual work equation is then defined as,

$$\int_V (f \cdot \delta v) dV = \int_V (F \cdot \delta v) dV - \int_V \rho (\ddot{u} \cdot \delta v) dV \quad (3.5.2)$$

Writing the d'Alembert force in terms of the reference volume and density,

$$\int_{V_o} \rho_o (\ddot{u} \cdot \delta v) dV_o \quad (3.5.3)$$

Where \ddot{u} is the acceleration with the equilibrium equations defined at the end of time step ($t + \Delta t$), calculated from the integration operator approximation for the nodal displacement as,

$$u = N^N u^N \quad (3.5.4)$$

Using the stated interpolation, d'Alembert force can be written as,

$$-\left(\int_{V_o} \rho_o N^N \cdot N^M dV_o\right) u^M \quad (3.5.5)$$

Representing the product of mass matrix and the acceleration of nodal definitions, the finite element approximation to equilibrium is,

$$M^{NM} u^M + I^N - P^N = 0 \quad (3.5.6)$$

The mass matrix is defined as the nodal displacement coefficient in the first term,

$$M^{NM} = \int_{V_o} \rho_o N^N \cdot N^M dV_o \quad (3.5.7)$$

The internal force vector is defined as,

$$I^N = \int_{V_o} \beta^N : \sigma dV_o \quad (3.5.8)$$

And, the external force vector is defined as,

$$P^N = \int_S (N^N \cdot t) dS + \int_V (N^N \cdot F) dV \quad (3.5.9)$$

The balance of d'Alembert forces at the end of time step and a weighted average of static forces at the beginning and end of time step then gives,

$$\begin{aligned} M^{NM} u^M|_{t+\Delta t} + (1 + \alpha)(I^N|_{t+\Delta t} - P^N|_{t+\Delta t}) - \alpha(I^N|_t - P^N|_t) \\ + L^N|_{t+\Delta t} = 0 \end{aligned} \quad (3.5.10)$$

Featuring $L^N|_{t+\Delta t}$ as the sum of Lagrange multiplier forces associated with degree of freedom N . The operator definition is completed using the Newmark displacement and velocity integration,

$$u|_{t+\Delta t} = u|_t + \Delta t \dot{u}|_t + \Delta t^2 \left(\left(\frac{1}{2} - \beta \right) \ddot{u}|_t + \beta \ddot{u}|_{t+\Delta t} \right) \quad (3.5.11)$$

$$\dot{u}|_{t+\Delta t} = \dot{u}|_t + \Delta t \left((1 - \gamma) \ddot{u}|_t + \gamma \ddot{u}|_{t+\Delta t} \right) \quad (3.5.12)$$

3.6 SHELL ELEMENTS

The shell element permits modeling of curved, intersecting shells that can exhibit nonlinear material response and undergo large translation and rotation motions. Thin shell elements provide solutions to problems which can be adequately captured by Kirchhoff shell theory. The general purpose shell element provides accurate solutions in all loading conditions for the thin shell type problem. These elements do not suffer from transverse shear locking or unconstrained hourglass modes.

In geometrically nonlinear analysis, the cross-section thickness of finite-strain shell elements changes as function of membrane strain per the defined Poisson's ratio. Shell elements are used to model structures in which one dimension, namely the thickness, is significantly smaller than the width and length dimensions. Conventional shell elements discretize a body by defining the geometry at a reference surface. The thickness is defined through the section property definition. Conventional shell elements have displacement and rotational degrees of freedom. For a homogeneous shell section, the total number of section points is defined by the number of integration points through the thickness. The number of integration points through the thickness is integrated during the analysis.

Conventional shells assume stress in the thickness direction to be nearly zero and that the strain results only from the finite element Poisson effect. Shell elements defined by integrating the section during the analysis use Poisson strain calculated by enforcing plane stress conditions. This is performed at either the individual material points in the section and then integrating the Poisson strain from the material points or at the integration for the whole section using the inputted Poisson's ratio. In this analysis, it is assumed that only the section Poisson ratio method is utilized, neglecting any localized necking or plasticity effects that occur through the shell element thickness when loaded. Material section property defines the shell made of a homogeneous material. The thickness and the number of integration points to be used through the

shell section define the material section. The cross-sectional behavior of the shell is calculated using Gauss quadrature, which provides greater accuracy than Simpson's rule with equivalent number of section points used in the analysis.

3.7 PLATE BUCKLING – CLASSICAL PLATE THEORY

To demonstrate the concept of plate strain, consider the rectangular plate element that is featured within classical Kirchhoff plate theory. The stress-strain, strain-displacement relationship is defined using a 4-node thin plate element. [11] These relationships can be used within

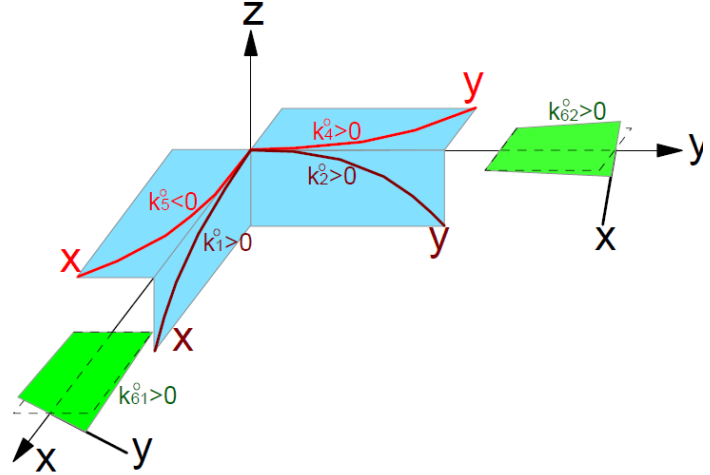


Figure 3.7.a Plate curvature variable definition

both the static boundary value problems and modal analysis eigenvalue problems.

The shell stress-strain, strain-displacement based relationships in the x, y, z directions are derived as follows,

$$\varepsilon_{11} = u_x - k_5^0 v + z(\theta_{2x} + k_5^0 \theta_1) \quad (3.7.1)$$

$$\varepsilon_{22} = v_y + k_4^0 u + z(-\theta_{1y} + k_4^0 \theta_2) \quad (3.7.2)$$

$$\varepsilon_{12} = u_y + v_x - k_4^0 v + k_5^0 u + z(\theta_{2y} - \theta_{1x} + k_4^0 \theta_1 + k_5^0 \theta_2) \quad (3.7.3)$$

$$\{\varepsilon\} = \begin{Bmatrix} \varepsilon_{11} \\ \varepsilon_{22} \\ \varepsilon_{33} \end{Bmatrix} = [\partial] \begin{Bmatrix} u \\ v \\ w \end{Bmatrix} = [\partial][N]\{d^{(i)}\} = [B]\{d^{(i)}\} \quad (3.7.4)$$

$$\begin{Bmatrix} u_1 \\ u_2 \\ u_3 \end{Bmatrix} = \begin{bmatrix} 1 & 0 & 0 & -z & 0 \\ 0 & 1 & 0 & 0 & -z \\ 0 & 0 & 1 & 0 & 0 \end{bmatrix} \begin{Bmatrix} u \\ v \\ w \\ w_x \\ w_y \end{Bmatrix} = [\tilde{B}]\{d\} \quad (3.7.5)$$

$$\begin{Bmatrix} \sigma_{11} \\ \sigma_{22} \\ \sigma_{12} \end{Bmatrix} = \begin{bmatrix} \hat{E} & v\hat{E} & 0 \\ v\hat{E} & \hat{E} & 0 \\ 0 & 0 & G \end{bmatrix} \begin{Bmatrix} \varepsilon_{11} \\ \varepsilon_{22} \\ \varepsilon_{12} \end{Bmatrix} = [\bar{Q}]\{\varepsilon\} \quad (3.7.6)$$

$$\hat{E} = \frac{E}{1 - \nu^2} \quad D = \frac{Eh^3}{12(1 - \nu^2)} \quad (3.7.7)$$

$$\begin{Bmatrix} \varepsilon_{11} \\ \varepsilon_{22} \\ \varepsilon_{12} \end{Bmatrix} = \begin{bmatrix} 1 & 0 & 0 & -z & 0 & 0 \\ 0 & 1 & 0 & 0 & -z & 0 \\ 0 & 0 & 1 & 0 & 0 & -z \end{bmatrix} \begin{Bmatrix} u_x \\ v_y \\ u_y + v_x \\ w_{xx} \\ w_{yy} \\ 2w_{xy} \end{Bmatrix} = [B]\{d\} \quad (3.7.8)$$

$$[k^{(i)}] = \int_{A_i} [\tilde{N}]^T [\Phi] [\tilde{N}] dA \quad (3.7.9)$$

$$[\Phi] = \begin{bmatrix} \hat{E}h & v\hat{E}h & 0 & 0 & 0 & 0 \\ v\hat{E}h & \hat{E}h & 0 & 0 & 0 & 0 \\ 0 & 0 & Gh & 0 & 0 & 0 \\ 0 & 0 & 0 & D & vD & 0 \\ 0 & 0 & 0 & vD & D & 0 \\ 0 & 0 & 0 & 0 & 0 & h^3G/12 \end{bmatrix} \quad (3.7.10)$$

$$[m^{(i)}] = \int_{A_i} [\tilde{N}]^T [\tilde{\Phi}] [\tilde{N}] dA \quad (3.7.11)$$

$$[\Phi] = \begin{bmatrix} \rho h & 0 & 0 & 0 & 0 \\ 0 & \rho h & 0 & 0 & 0 \\ 0 & 0 & \rho h & 0 & 0 \\ 0 & 0 & 0 & \rho h^3/12 & 0 \\ 0 & 0 & 0 & 0 & \rho h^3/12 \end{bmatrix} \quad (3.7.12)$$

To illustrate the buckling behavior of a rectangular thin plate subjected to critical loading pre-compression, consider the finite element formulation using Geometrically Exact Structural Analysis (GESA) static and modal system response. A four-node, six degree-of-freedom thin plate element is discretized into 10 x 10 sections along X and Y directions. Boundary conditions are applied in the X, Y, Z directions along all four plate edges and at $x = L/2$ to constrain spatial displacement. The

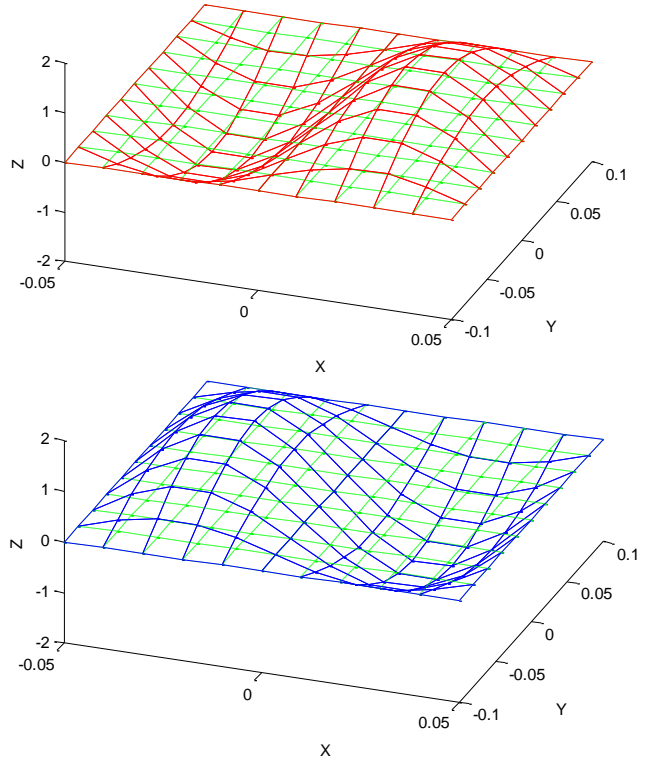


Figure 3.7.b CCW (top) & CW (bottom) input torque couple to strained, constrained plate

The compressive pre-stresses, τ are applied at $x = 0$ and $x = L$ inward normal opposing directions to achieve the first natural frequency equating to the first zero eigenvalue.

At the critical static loading, the thin plate becomes compliant and can be deformed with a small change to the angular displacement along the symmetric axis defined at $x = L/2$ perpendicular to the applied pre-compression direction.

Applying a positive input torque in the counterclockwise (CCW) direction to the plate results in a deflection as shown in Figure 3.7.b (top); conversely, a negative applied input torque in the clockwise (CW) direction yields an identical deflection path in the opposite direction as shown in Figure 3.7.b (bottom). The thin plate motion on the left and right sides produce conjugate deflection that acts in the direction of applied input torque.

3.8 THE LIMIT CYCLE

A limit cycle is an isolated closed trajectory, which means that neighboring trajectories spiral toward or away from the limit cycle. These dynamic systems model self-sustained

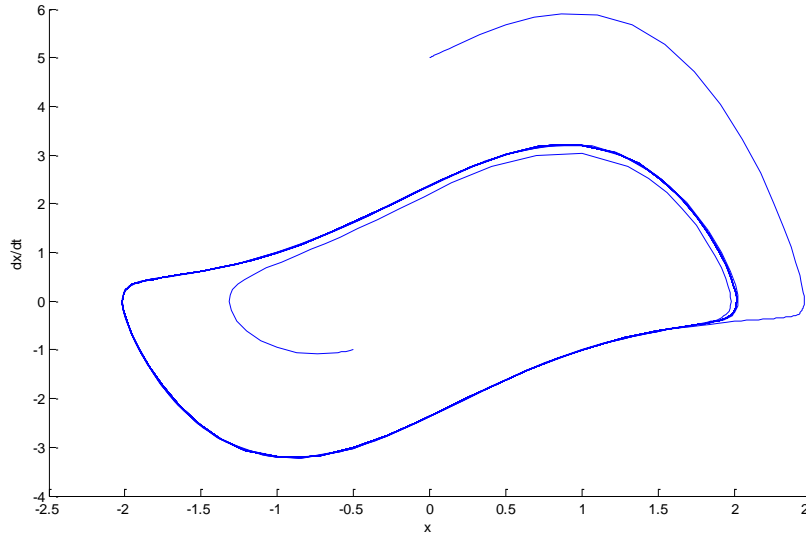


Figure 3.8.a Limit cycle trajectory oscillations

oscillations, such as the beating of a heart. There is a standard oscillation of period, waveform and amplitude that these systems attenuate even in the absence of an external periodic force.

When perturbed slightly, the system returns to the standard cycle. In a linear system represented as $\dot{\mathbf{x}} = A\mathbf{x}$ there can exist only closed orbits; however, the amplitude of the linear oscillation is governed by the initial conditions. Any slight disturbance to the amplitude will continue forever, whereas limit cycle oscillations are governed by the inherent system structure. Thus, a linear system cannot replicate the dynamic motion prescribed in the mechanical flutter of the human heart to impart fluid transport. The van der Pol equation shown in Figure 3.8.a is governed by the dynamic mathematical model, which features a nonlinear damping parameter $\mu(x^2 - 1)$ that behaves as positive damping for $x > 1$ and negative damping for $x < 1$. [15]

$$\ddot{x} + \mu(x^2 - 1)\dot{x} + x = 0 \tag{3.8.1}$$

4 FLUID-STRUCTURAL INTERACTION

4.1 FLUID-STRUCTURE INTERACTION COUPLING

At the fluid structure interface, the structural and fluid fields share a common interface denoting the coupling conditions as Γ ,

$$d_r = \frac{\partial u_r}{\partial t} \quad (4.1.1)$$

$$\sigma_r^S \cdot n = \sigma_r^F \cdot n \quad (4.1.2)$$

Given the interface structural displacement d_r , the interface fluid velocity u_r and the Cauchy stresses for both fluid σ_r^F and structure σ_r^S projected along the interface normal n . The fluid domain displacements d_g are based on the original fluid domain position x_o and the interface displacement d_r which accounts for the fluid domain deformation as an extension of the fluid structure interface deformation. The fluid structure interaction solution schemes are independent of numerical treatment of the time-varying fluid domain. The fluid field is governed by incompressible Navier-Stokes equations on a deforming domain, where both the fluid velocity and dynamic fluid pressure can be applied to the fluid region.

The conservation of momentum, fluid body forces and strain rate tensor for Newtonian fluid with dynamic viscosity are used to map the fluid region. The conservation of mass requires constant density for the incompressible fluid. The computed field equations are discretized in space and time. The relationship between the fluid and solid continua can be best understood as an interaction type of problem to which the response is governed by the neighboring interface.

Motion of the solid induces some motion within the fluid which is assumed to remain in contact with the solid without penetration or separation. The fluctuating displacement imparted by the solid continua is a function of time for a dynamic case. As the fluid moves fluctuating stresses are generated, which then load the solid by imposing fluctuating forces at the interface.

The motion of the solid is then modified from the initial configuration per direct feedback from the fluid continua. If the solid leads in the motion, it then drives the fluid which responds to the amplitude of fluctuation. If the fluid leads in the motion, then the solid is driven by the exerted pressure field and the solid is displaced. On the wall wetted nearest the fluid, the fluid and solid continua maintain the same nodal displacement for a no-slip boundary condition constraint.

The fluid and structural stresses exerted on the wetted wall are equivalent given the local dynamic equilibrium. The dynamic equations of deformable solids are formulated using the theory of solid continuum mechanics, related to the material points. The dynamic equations of fluids are formulated using continuum fluid mechanics theory, including the fluid properties referenced to the spatial cell volume and not the individual fluid particles.

Consider a solid modeled as continua which occupies a finite volume bounded by a closed surface. The motion of solid governed by the local equations of dynamic equilibrium is defined by solid continuum mechanics. The density and Cauchy stress tensor of the solid material represents the state of stress for the body subjected to an external fluctuating load which is time dependent. The body force field is assumed to vanish at the boundary superimposed by the contact force field exerted on the boundary. Motion is prescribed to a portion of the boundary which is given a time-dependent displacement field. As the solid moves, its initial and actual configuration at a lagging time is not identical.

A fluid can only resist an external load through normal stresses, which are the same in all directions provided that the fluid behaves as isotropic continua. This behavior then gives the isotropic diagonal tensor,

$$\sigma_f = - \begin{bmatrix} P & 0 & 0 \\ 0 & P & 0 \\ 0 & 0 & P \end{bmatrix} \quad (4.1.3)$$

Where p gives the pressure and no such static shear stresses arise in a fluid to resist an external shearing load. The stress forces per unit volume can be expressed by,

$$\text{div } \sigma_f = -\text{grad } P \quad (4.1.4)$$

This definition of pressure is applicable only for incompressible fluid continua. Fluid compressibility does not modify the pressure which balances the external load; rather, it provides a means to relate the pressure to fluid strain through stress-strain relationship as performed in the case of an elastic solid. The elastic potential density per unit of fluid volume is defined as,

$$e_e = \frac{1}{2} \sigma_f : \varepsilon_f \quad (4.1.5)$$

Where ε_f is the small strain tensor and the hydrostatic stress tensor is defined as,

$$e_e = -\frac{1}{2} p \text{div } \overline{X}_f \quad (4.1.6)$$

Where \overline{X}_f gives the small fluid displacement and p gives the small change in pressure.

Extending the one-dimensional elastic law to the three-dimensional case,

$$p = -E_f \text{div } \overline{X}_f \quad (4.1.7)$$

Substituting, the quadratic positive form of elastic potential density is given as,

$$e_e = \frac{1}{2} \rho_f c_f^2 (\text{div } \overline{X}_f)^2 \quad (4.1.8)$$

It is then possible to define the movement of the fluid boundary domain through software interface to extract stress data along moving boundaries. Only the pressure distribution is needed along the moving boundary to define fluid response to the impending structural deflection. The response of flow solver is represented as,

$$p_{k+1}^{n+1} = F^{n+1}(X_{k+1}^{n+1}) \quad (4.1.9)$$

Where X_{k+1}^{n+1} denotes the prescribed position of the boundary nodal definitions obtained from the structural solver in sub iteration or iterate $k + 1$ when computing the solution for time $n + 1$ incrementation. The superscript $n + 1$ on F denotes the other variables in the flow solver that are already known for time step $n + 1$ which includes inflow and outflow boundary conditions. Initializing from time step n the pressure distribution on the boundary nodes p_{k+1}^{n+1} is

computed, which is then communicated to the structural solver. The structural model is defined as,

$$G^{n+1}(X_{k+1}^{n+1}, p_k^{n+1}, \Delta p_{k+1}^{n+1}) = 0 \quad (4.1.10)$$

The function G^{n+1} incorporates the prescribed time dependency of the structural properties and it is assumed that the structural solver computes updated boundary node position and pressure change Δp_{k+1}^{n+1} for all nodes. The pressure change is used to adjust the pressure used in the fluid computations. The structural equations can be defined as,

$$G^{n+1}(X_{k+1}^{n+1}, p_k^{n+1}) = 0 \quad (4.1.11)$$

For a given pressure input p_k^{n+1} incoming from the fluid solver, which neglects the update of pressure boundary condition needed in the fluid solver. [14]

4.2 COUPLING PLATE STRAIN ENERGY TO GENERATE FLUID FLOW

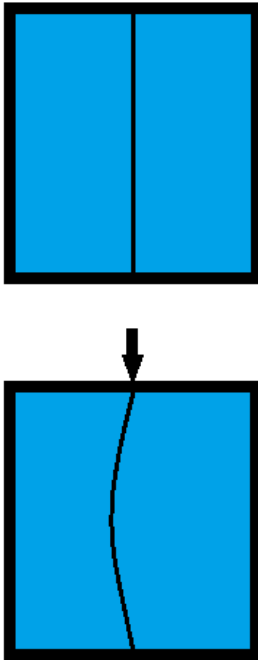


Figure 4.2.a Fluid structure interaction

Consider a direct coupling between the mechanical strain energy of a pre-compressed thin plate and forced flow of neighboring fluid particles. A simplified configuration features a thin plate suspended within a sealed container as shown in Figure 4.2.a. The left (L) and right (R) side control volumes (CV) are isolated by an intermediate mutual thin plate boundary. The applied critical buckling load onsets the bifurcation of the immersed plate. The strained plate deflection towards the left control volume (L_{CV}) yields an applied positive pressure on the left as the volumetric deflection attempts to compress the incompressible fluid CV. Moving in the opposite direction towards the right control volume (R_{CV}), a negative applied pressure attempts to stretch the incompressible fluid. The deflection exerts equivalent pressure magnitudes on each respective

fixed control volume that varies only in the applied direction.

The plate behaves as a loaded diaphragm that is stiff in the deflected position, yet compliant in the strained vertical position. With a fixed control volume, the plate can flutter to the left and right without performing external mechanical work on the system.

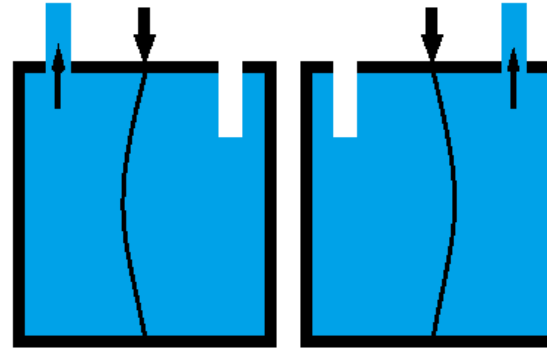


Figure 4.2.b Irreversible bifurcation fluid motion control volume

If L_{CV} and R_{CV} are opened to allow fluid to move across the CV, then the thin plate generates positive pressure in the deflection direction. As shown in Figure 4.2.b, the fluid flows out of the L_{CV} and produces negative displacement suction on the R_{CV} region. The vacuum then draws air from the atmosphere into the control volume. Reciprocating the plate deflection backward and forward produces an irreversible net fluid displacement. Consider four separate valves placed at the L and R chambers, for both the top (T) and bottom (B) locations. Sensing the direction of fluid displacement, these valves open and close to achieve the desired fluid motion as shown within Figure 4.2.c. The plate deflection towards the L_{CV} forces LB and RT valves into the closed positions.

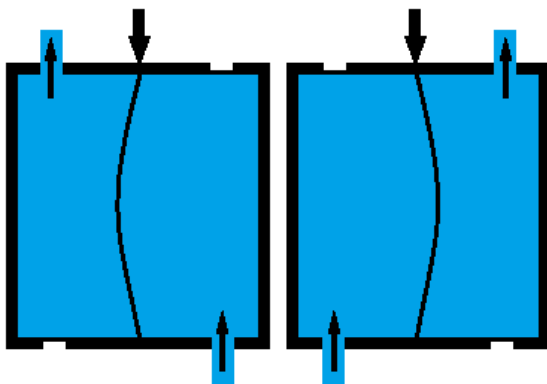


Figure 4.2.c Reversible bifurcation fluid motion control volume

The simultaneous passive valve actuation generated by sudden onset of plate bifurcation gives the positive displacement fluid flutter. The thin plate deflection serves to provide the pressure pulsation acting on the fluid. Applying an oscillatory load to the common plate surface that is capable of plate deflection services the two chamber type

design requirements. Recall the plate illustrated by the rectangular plate in which the structural bifurcation was onset by a small torque applied at the pre-compressed plate mid-plane. The input torque actuates the plate bifurcation into the two positions shown in Figure 3.7.b. Reversing the direction of the applied mechanical input torque, the plate can achieve a similar fluid motion response as that demonstrated within Figure 4.2.c. The oscillating compressive load is replaced by an oscillatory input torque applied to the pre-stressed thin plate. Induced strain energy created during plate pre-compression is redirected inward as the input torque is reversed. This action onsets bifurcation to the deflected path and exerts a normal applied pressure to the fluid adjacent to the thin plate wall. Such orthogonal pressure pulsation is similar to that of the beating heart, in which the ventricular contraction forces positive fluid flow directed normal to the myocardial wall. This action minimizes fluid shear stress exerted on the suspended fluid particles, reducing red blood cellular damage. The fluid control volume experiences a positive displacement squeezing action that forces blood from within the chamber. The left side atrium and ventricle service blood flow to the entire body while the right side circulates spent blood through the pulmonary loop for red blood cell oxygenation.

Each loop is isolatable yet structurally coupled for synchronous blood transport. To

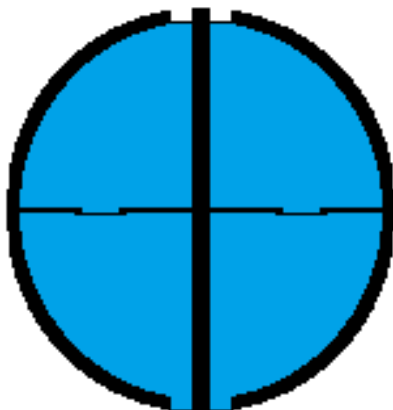


Figure 4.2.d Four chamber closed configuration

achieve the necessary routing of blood flow through a continuous loop, a minimum of two separate chambers is featured within the initial design synthesis. Four separate chambers that contract and expand in coincidence as shown in Figure 4.2.e is the ideal configuration in maintaining conformance with the heart structure. Six separate unidirectional check valves placed along the control volume boundaries serve to enclose fluid within the four quadrants. Fluid flow is simultaneously sensed

and controlled by the pressure-actuated passive valves, opening and closing the CV boundaries. In the design of a cardiac device, such timing is crucial to avoid mass accumulation or platelet shear stress damage that results in actuating the valve. The valve design must feature passive pressure actuated positioning to avoid backflow of blood in the reverse direction of flow and to promptly respond to the change in the dynamic pressure transient.

Beginning at the rightward location and proceeding in a CCW rotation, the quadrants are defined as QI, QII, QIII and QIV similar to a trigonometric unit circle quadrants. The center plate that runs from top to bottom remains stiff in comparison with the pin-pin configuration of the bisecting pre-compressed compliant plate directed left to right. The hydrostatic position is shown within Figure 4.2.d, with the valves along the control volume peripheral boundaries in the closed position. At this stage in the cycle, there is no fluid flow permitted through the valves and the mechanism is fully-shut. Without an applied external or internal force, the system achieves diastolic conditions whereby static fluid pressure upstream and downstream is interlocked and unchanged.

Placing the applied input torque at the perpendicular plate bisection upsets the compliant plate into the first mode of bifurcation. This motion is illustrated in the Figure 4.2.e displaying the observed fluid flutter in the direction of the applied input torque. The CCW (CCW) motion of the input torque about the central bisection axis of rotation generates a positive pressure in Q3 while simultaneously pulling fluid into Q2 control volume. The pressure differential sensed by the intermediate valve forces this interface into the closed position. The

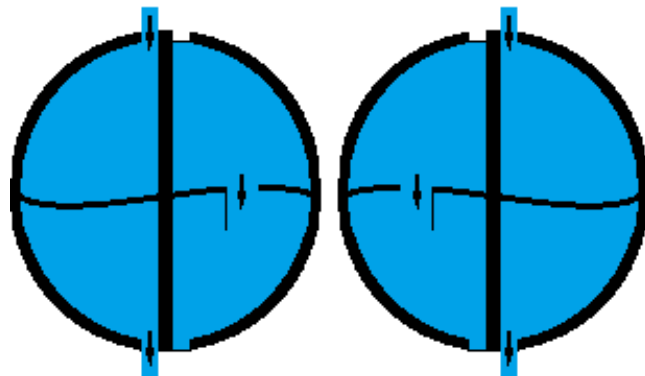


Figure 4.2.e CCW & CW input torque coupling strained, constrained plate bisection

control volume maintains fixed volume and mass-flow rate for both Q2 and Q3 chambers as blood is forced simultaneously through Q2 and Q3 chambers on the left-hand side undergoing isovolumetric expansion. At the same instance in time, the right-half chambers Q1 and QIV observe isovolumetric contraction that opens the intermediate actuating valve and transports fluid from Q1 into Q4 control volume. Internal fluid flow occurs from Q1 to Q4 as the plate attempts to pressurize Q1 and to stretch Q3 entrained fluid. Fluid flow motion through the mechanism is performed ide synchronously and without integration of active hydraulic control valves to open and close the control volume fluid boundaries. The bifurcation concavity is governed by the direction of the applied torque. Reversing direction of the applied input torque from CCW to CW then upsets the corresponding deflection in the opposite direction. The cycle commences in the identical sequence as shown in Figure 4.2.e, replicating conjugate fluid motion on the opposite chamber half. The left-half chambers undergo isovolumetric contraction while the right-half chambers observe isovolumetric relaxation.

4.3 USE OF COMMERCIAL SOFTWARE TOOLS - THE PHILOSOPHY

Applying the aforementioned fluid and structural principles, available commercial software is utilized to solve the complex fluid-structural interaction problem. It is poor engineering practice to utilize any software which removes understanding and comprehension from the problem physics. The software itself is less difficult to learn and implement than raw developments of structural and fluid mechanics theory, computational algorithms and solving schemes. However, the ease-of-use in this software does not omit the fundamental understanding which governs that continua physics. Such a tool is highly useful in the approach of this problem type, as the required computational programming is reduced to expedite physics setup and to run the numerical simulation. Using the correct tool to solve complex problems is common practice in engineering conserve resources such as time, cost and schedule. The use of a hammer to drive

a screw may secure the fastener, but fails to do so per design. Likewise, understanding how to swing a hammer is crucial in driving a nail; without which neither a screw nor a nail can be fastened. Selecting the correct tool is equally important to the knowledge required in operating said tool. Using software to perform a computationally extensive numerical simulation is, in a sense, selecting the proper tool to obtain the correct solution when appropriately used. Without a fundamental understanding of the software “black-box” inner workings, it is difficult to give physically significant results. Given enough time and resources, the analyses featured by this software may be replicated by hand computation and computer programming much like driving a nail with bare hand; it can be done, yet it is excruciatingly painful and a poor use of time. The aim in selecting such a method is not to omit understanding; rather, to redirect the allotted time to examine the proposed fluid-structural interaction problem. The ultimate goal is to envision that which does not yet exist with the intent to further design, analyze and manufacture such a device. Through the provided numerical experimentation results, a design is analyzed to demonstrate how such a device functions.

4.4 COUPLING STAR-CCM+ AND ABAQUS CO-SIMULATION

Conventional solid and fluid regions are created and meshed in STAR-CCM+, both regions are solved separately by selecting the physics continua with the appropriate mathematical models to generate scalar and vector field data. The solutions for solid and fluid regions are completed separately, coupling through the exchange of boundary data at the common surface boundary. Surface data mappers are created to map from the solid to fluid and from the fluid to solid. This method is applicable only to weakly coupled mechanical systems in which the solid and fluid regions can be approximated as nearly independent systems.

The fluid structure interaction (FSI) application built within STAR-CCM+ as the primer server, utilizes the structural analysis performed within Abaqus to model and solve for the solid

region nodal displacements and STAR-CCM+ to compute the resulting fluid region surface traction loads. The fluid physics continua and solver properties are specified within STAR-CCM+, requiring that the FSI include mesh model morphing fluid cell volumes to transition with the solid displacement without fluid-to-structure separation. The Abaqus simulation is executed to give the initial nodal displacement database (.odb) from the input file (.inp). Importing the nodal displacement database file into STAR-CCM+ then gives the surface pair interfacing to couple the fluid to solid data exchange. The FSI analysis includes pressure and wall shear stress from fluid to solid and the surface displacements from solid to fluid surface map. The solid to fluid interaction is defined using the solid surface as the driving source and the fluid boundary as the driven target surface. Nodal displacements computed in Abaqus are then mapped onto the FSI boundary in STAR-CCM+ and used to conform with the originating solid definition and motion.

To map data between STAR-CCM+ and the imported Abaqus model, the imported surfaces must map to a fluid boundary defined within the STAR-CCM+ software. This approach is known as a file-based coupling approach, where the fluid motion is driven by the shell displacement computed within the Abaqus simulation. By mapping data between STAR-CCM+ and Abaqus, running the two codes sequentially gives a converged solution for the whole model. The solution for each part of the model is obtained at the interface between fluid-to-structure surface and nodal mesh definitions.

The file-based sequential analysis is sufficient for instances which are deemed one-way or weakly coupled fluid-structural interaction type problems. For the strongly coupled or two-way FSI problem proposed, the use of mechanical co-simulation is required to accurately describe the relationship between fluid and structure. A mechanical co-simulation case features the simultaneous integrated use of STAR-CCM+ and Abaqus for a strong physical coupling between the two codes. Data is exchanged at iterate step intervals, allowing for a full solution across the

fluid-solid interface to be computed in coincidence. This two-way communication captures response of fluid to changes in the solid and response of solid to changes in the fluid.

The solvers iteratively converge to equilibrium for each step increment in tandem to the solution obtained by the adjacent continua. The fluid response is modified to changes in the structural shell surface deflection, which is then updated to reflect changes to the fluid state. It is this inseparable coupling that introduces complexity in numerical solution convergence. The mechanical coupling relays STAR-CCM+ traction loads to Abaqus, which then transmits said displacements to STAR-CCM+. These displacements are then used as input to the mesh morpher defining the fluid control volume. The co-simulation data is then exchanged between STAR-CCM+ and Abaqus using the co-simulation engine, differing from the aforementioned file-based sequential method in that now the solution cannot be independently solved.

Only an implicit numerical scheme can be applied to obtain the simultaneous solution which satisfies both the fluid and structure boundary conditions and convergence criteria. Separate models are prepared for the fluid and solid domains; a modified Abaqus solid model defined by the input file (.inp) and STAR-CCM+ fluid model to give the appropriate boundary conditions, physics, geometry and meshing properties. Fluid domain is initialized using a quasi-steady state simulation, disabling co-simulation and mesh morphers to run an increased time-step size and internal iterations for a single simulation time-step. This gives the initial flow field used as the initial conditions for the co-simulation. Limited computational resources, including both processor capacity and allowable software licensure are permitted to simultaneously execute the simulation. This constraint restricts the meshing discretization size and time-step increment used in the analysis. Only select geometrical configurations are permitted, as an increase in the complexity of mechanism geometry lends to an increase in the mesh size and density. In practice, it is preferred that the node size is minimized as to achieve optimal simulation runtime. While a finer mesh density gives increased accuracy, it can significantly increase computational runtime.

The co-simulation features two stand-alone models, which are both capable of independent solution convergence. The traction and displacements are interchanged between STAR-CCM+ and Abaqus to allow the coupled boundary to move in accordance with the imported nodal field data. The implicit numerical iteration leads with the initial Abaqus nodal displacement solution, and then lags with STAR-CCM+ fluid region response. The fluid region mesh must morph to accommodate structural displacements along the FSI boundary. Mechanically coupling the fluid and structural solvers increases the computational runtime as outputted field data must be transmitted between software at every node for each step increment.

4.5 INDUCED SHELL BIFURCATION FINITE ELEMENT ANALYSIS

As a means to demonstrate the structural bifurcation that governs the desired shell deflection path, a finite element model was developed within Abaqus, V6.11-2 commercial software. This preliminary analysis serves as an initial reference in visualizing the shell behavior given boundary conditions and applied loadings.

Using the available numerical simulation software to obtain a preliminary working solution eliminates analytical developments and computational code scripting. All standard units are expressively defined per the SI unit of measurement for length (m), time (s) and mass (kg). Material properties are defined for annealed titanium Ti-8Mn, which is utilized as a compositionally inert material with exceptional corrosion and fatigue resistance.

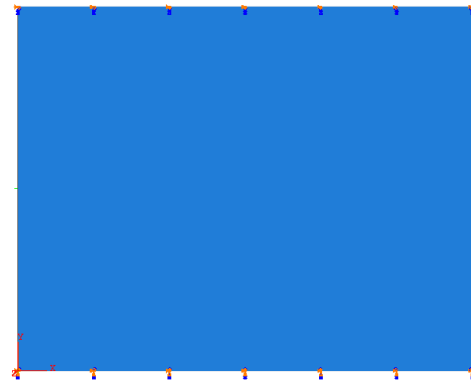


Figure 4.5.a Shell boundary conditions

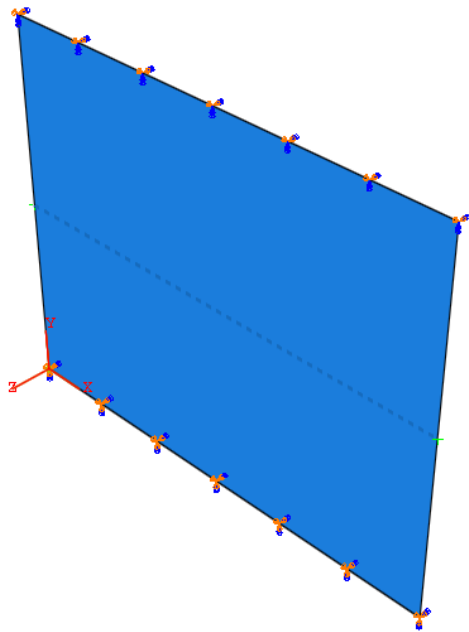


Figure 4.5.b Shell applied loading

A homogeneous quadrilateral shell element was selected to discretize the rectangular geometry, modeled with a through-thickness of 3.8 mm. Boundary conditions were selected as to constrain translational shell motion in the x direction and along the shell edges. The global coordinate system is shown within Figure 4.5.b, which displays translational displacement constraint applied along the bottom shell edge in the y direction.

The top shell edge permits displacement along the y axis as shown within Figure 4.5.b and

Figure 4.5.c. Shell edge constraints along the top and bottom permit rotational about the x axis such that the shell is free to rotate CW or CCW based upon the input torque direction. The bottom edge emulates pin joint behavior while the top acts as a revolute translating joint. Rotational constraints along the bottom and top shell edges constrain in-plane y and z displacements pin axis of rotation. The angular displacement applied about the x axis drives the shell bifurcation outward in the positive or negative z direction.

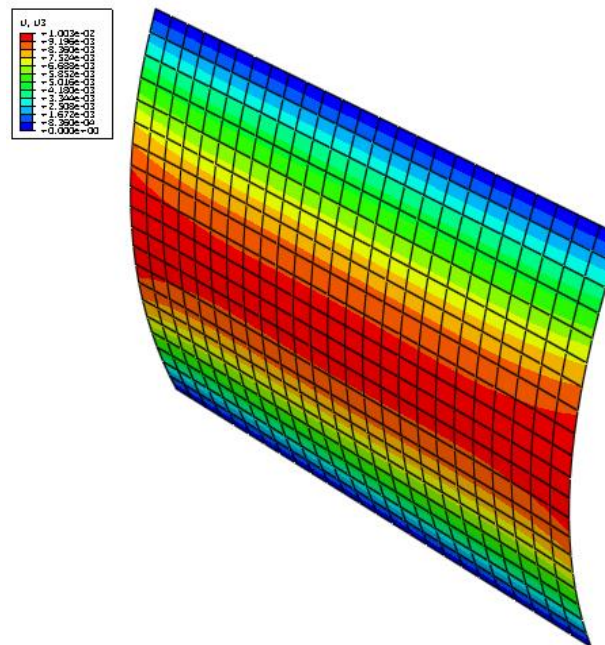


Figure 4.5.c Applied CCW shell input torque

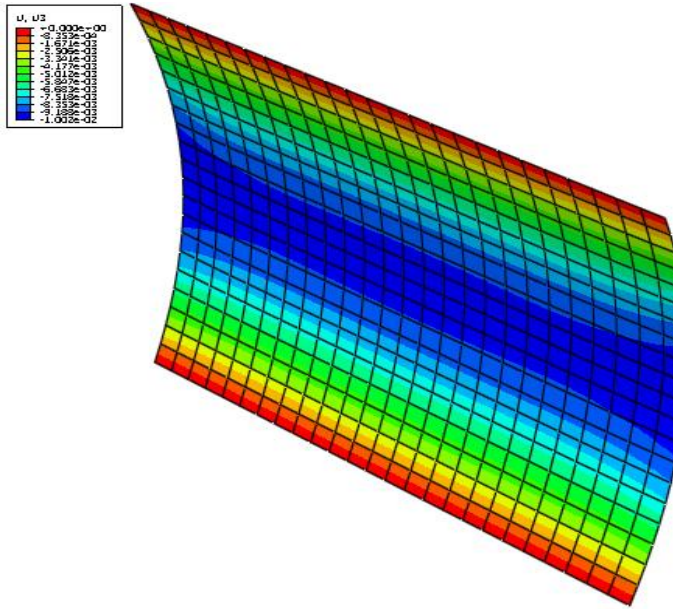


Figure 4.5.d Applied CW shell input torque

shown within Figure 4.5.c and Figure 4.5.d.

The simulation features four separate steps in which the static loading is reversed to achieve the shell displacement path. A mechanical shell pre-compression is applied to the shell edge locations at the top and bottom sections. Step amplitude is ramped linearly for each consecutive step incrementation. Each of the four steps alternates the applied shell edge moment direction along the constrained shell edge locations.

In the first simulation

Modifying boundary conditions and constraints alters the shell deflection magnitude. Boundary conditions were selected as to increase the outward and inward z displacements normal to the xy plane as shown within Figure 4.5.c. The surface contours display the outward z displacement, with red indicating positive and blue negative as

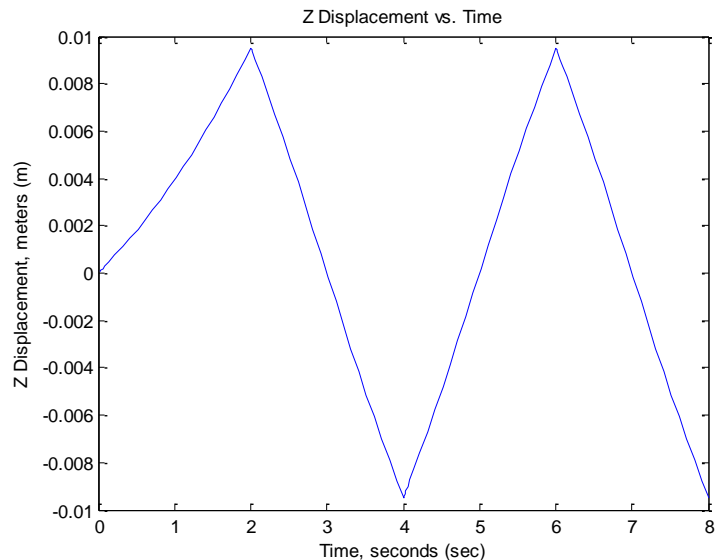


Figure 4.5.e Shell face displacement versus time

step, a CW moment is applied at the top shell edge (TSE), while a simultaneous CCW moment is applied along the bottom shell edge (BSE).

This edge moment reciprocation is repeated in the subsequent three simulation step iterations, alternating moment direction along each shell edge. In Figure 4.5.c, the static buckling mode is given to visualize the displacement magnitude and inflection along the shell surface for the first step iteration.

The loading reverses in the opposite direction for the next step loading that follows the initial static shell bifurcation onset as shown in Figure 4.5.d. Using a full Newton numerical solver, the software determines the static displacement through dynamic numerical integration; ramping the applied loads throughout the simulation duration to the maximum input magnitude. A small applied moment then onsets the shell bifurcation as shown within Figure 4.5.c, which is forced into the respective deflection mode. The plot shown within Figure 4.5.f demonstrates the nonlinearity in the forced shell bifurcation for the y displacement. Alternating the applied shell edge moment direction gives a flutter effect alongside each shell surface as shown within Figure

4.5.d. This is the driving mechanism that allows the simultaneous pushing and pulling along the left and right side shell surfaces. Changing the shell concavity directs positive or negative shell bifurcation; rotating the shell edges through an angular displacement forces shell deflection along the desired

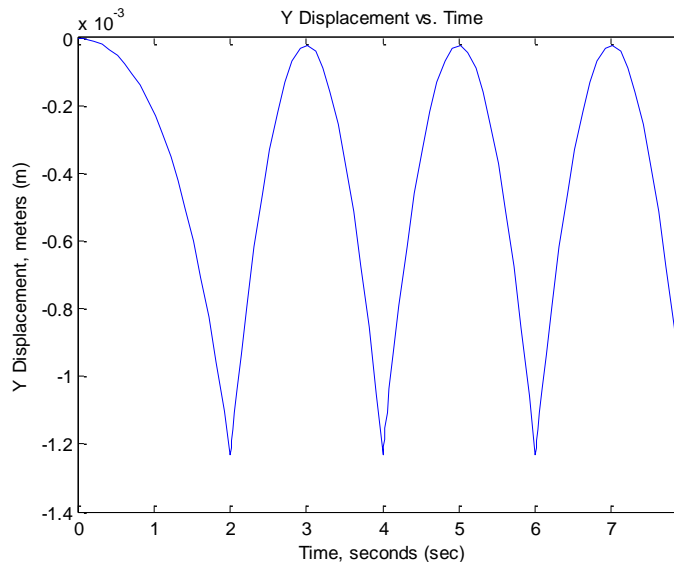


Figure 4.5.f Shell edge displacement versus time

bifurcation branch.

The shell displacement in the z direction normal to the shell surface is illustrated in Figure 4.5.c and Figure 4.5.d for the CCW and CW rotations, respectively. The nodal displacement in the z direction is shown within Figure 4.5.e for a node located on shell surface midplane center. The moment is ramped

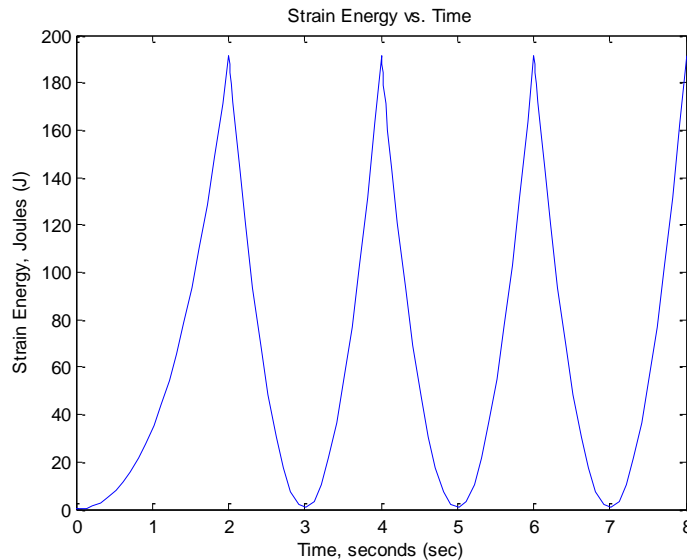


Figure 4.5.g Induced shell strain energy versus time

linearly from a null value up to the maximum input torque. The compressive shell edge load that is directed inward parallel to the shell surface is ramped from a null value beyond the buckling load. Linearly ramping the applied input torque and compressive load gives an approximation for how the shell responds through time to various instantaneous loading combinations. In the simulation, the precise instantaneous buckling load magnitude need not be known to give the desired bifurcation. The ramp range upper limit exceeds the buckling load during the z outward normal deflection path as shown within Figure 4.5.c and Figure 4.5.d. The incremental static equilibrium is computed using a dynamic solver to emulate the step-wise loading response. The shell flutter results from a moment coupling and pre-compression directed normal to the shell BSE and TSE. Without a mechanical pre-stress directed inwards, the conjugate moment coupling gives significantly less deflection and nodal y and z displacements. Mechanical shell section pre-compression approaches a buckling load given by the first eigenvector, which decreases the required input torque to onset the bifurcation magnitude.

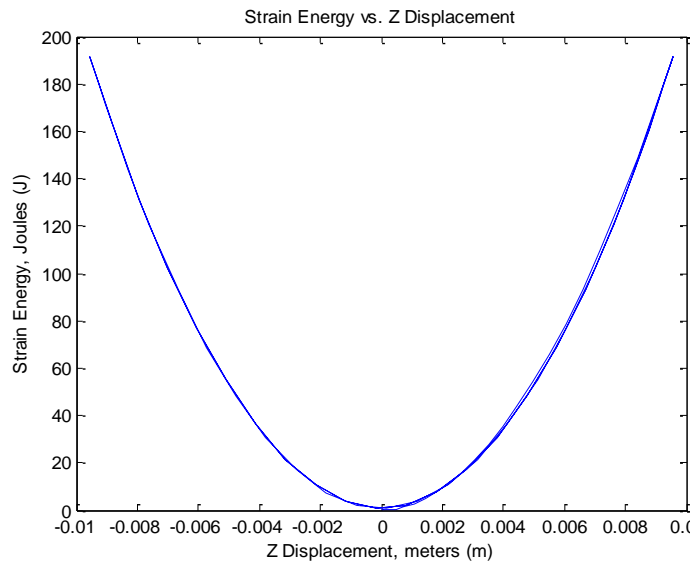


Figure 4.5.h Shell strain energy versus displacement

The shell is significantly weakened by the applied mechanical pre-compression when vertically erect. As the shell deflects towards the bifurcation equilibrium state, the shell becomes stiff and then stores elastic strain energy. Plotting the y displacement through each step incrementation

equilibrium solution gives a characteristic curve as shown within Figure 4.5.f. The shell deflection follows the forced bifurcation branching. The uppermost point along the shell is displaced towards the constrained lower pin joint. This nonlinear shell displacement amplifies the shell deflection, increasing the

xy plane deflection gradient in the z direction. Nodal displacement that occurs along the x direction is negligible for the defined loading and boundary conditions. The stored strain energy within the shell nears a maximum value as the cycle phase is complete

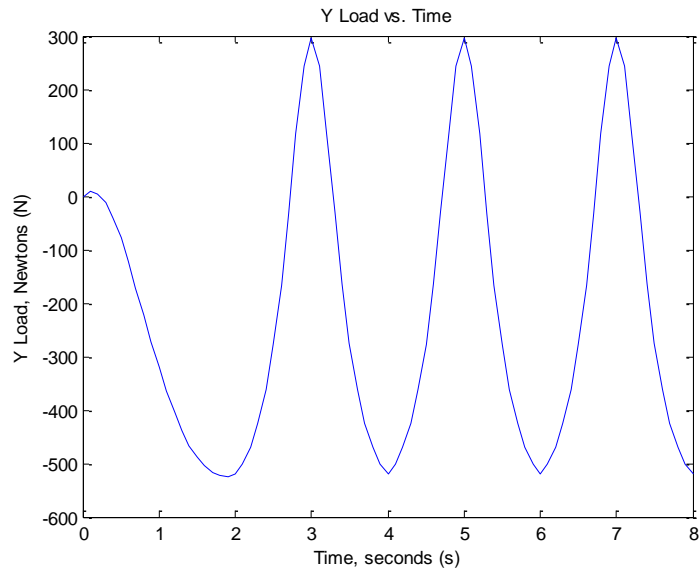


Figure 4.5.i Shell edge load versus time

as shown within Figure 4.5.g. The applied strain energy is released following the equilibrated deflection state with a load reversal.

When the shell is in the vertical, undeflected position there exists no kinematic energy exerted on the shell. The strain introduces small nodal displacements that occur in the y direction, compressing the finite elements to store strain energy.

The energy is stored as potential energy until the bifurcation is upset by input torque. Once the strained shell translates, the stored potential energy is released as kinetic energy and is then stored as strain energy as the shell achieves the deflection equilibrium state. This onset gives the first modal bifurcation point of zero strain energy, in which the strain maintains a negative value until the shell deflects. As shown within Figure 4.5.b, the boundary conditions and loadings are given such that the shell is weak when erect in the undeflected vertical position. The buckling load applied orthogonal to the shell section is determined solely from material stiffness and geometry. Reducing the shell sectional thickness, width and material stiffness reduces the required load to onset

bifurcation. Decreasing stiffness matrix then decreases the potential stored strain energy. Plotting shell strain energy versus z displacement for a node along the midplane gives the anticipated parabolic relationship as shown within Figure 4.5.h. The strain energy maintains a positive, definite

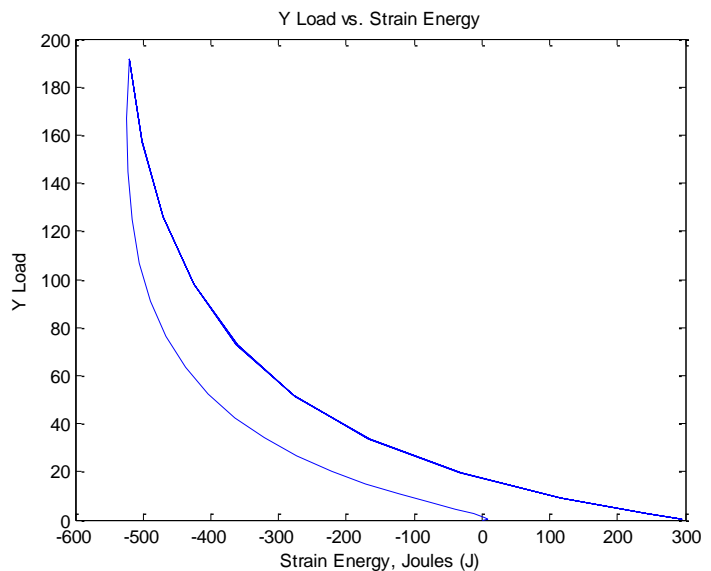


Figure 4.5.j Shell edge load versus induced strain energy

value for both positive and negative nodal displacements in the z direction.

For a given strain energy magnitude, there exists two possible equilibrium z displacements. The input strain energy alone cannot determine deflection path as the solution lies upon one of the two possible bifurcation branches. The applied moment coupling alongside the TSE and BSE forces deflection along the desired bifurcation path. Given direction and magnitude of the applied shell edge moment, the shell deflection path equilibrium displacement is determined.

The z nodal displacement results from the applied compressive load and edge moment magnitude and direction along the shell edge. Motion that occurs in a direction which does not originate along the input load vector does no such work on the system. If there exists displacement along the z direction without which a load is applied in the z direction, then the work through the z direction is null. The z displacement results from an applied load to the system coupled with an edge moment. In the shell bifurcation, the compressive load applied inward to the BSE and TSE edges does not solely upset the directed deflection. The applied shell

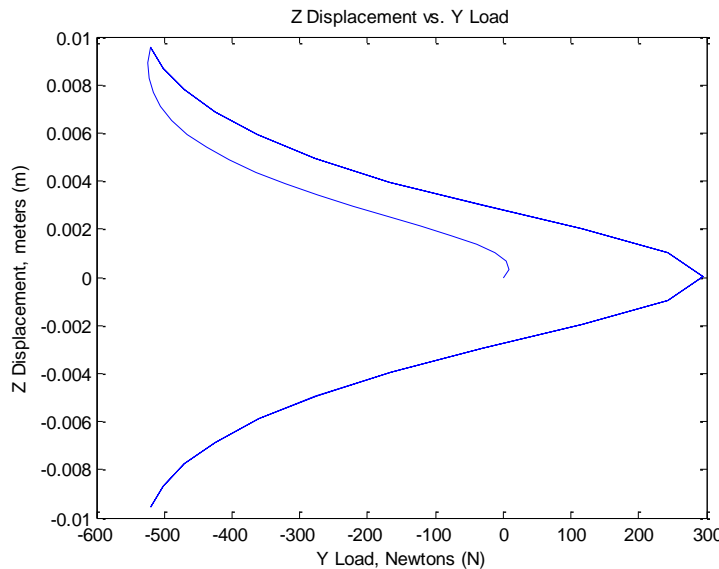


Figure 4.5.k Shell surface displacement versus edge load

edge load in the y direction does work through the y displacement. Applying a CW and CCW edge moment along the x axis generates an angular displacement that is directed orthogonal to the shell face. The angular displacement along the BSE and TSE then gives the displacement in the z

direction that does work on the system. Assuming an ideal case, the strain energy stored within the shell as shown within Figure 4.5.g is then expended to the neighboring fluid region.

The y reaction load versus time plot is shown within Figure 4.5.i, which gives the nodal force observed at the spatial constrained BSE. The applied load is compressive throughout the simulation; however, the y reaction load features tensile values as the shell releases stored energy in passing through the equilibrium position. The reaction load in the y direction is positive when the shell is in the vertical strained equilibrium position as shown within Figure 4.5.f.

In Figure 4.5.j elastic strain energy is plotted versus the y reaction load. A cusp originates from the initial vertical position to the deflected equilibrium solution. The initial profile in the first step increment is followed by rightward path for successive step incrementations. Once the shell is displaced from the initial vertical orientation, reduced y reaction load is required to achieve maximum strain energy stored in the deflected equilibrium position. The z displacement versus y reaction load is shown within Figure 4.5.k, where a similar behavior is observed to the aforementioned Figure 4.5.j profile. Starting at a null z displacement and y reaction load, the profile moves to the upper-

left cusp then along the path as shown within Figure 4.5.k. The compressive load drives the maximum z displacement. The tensile load is observed at the minimum z displacement that occurs as the shell

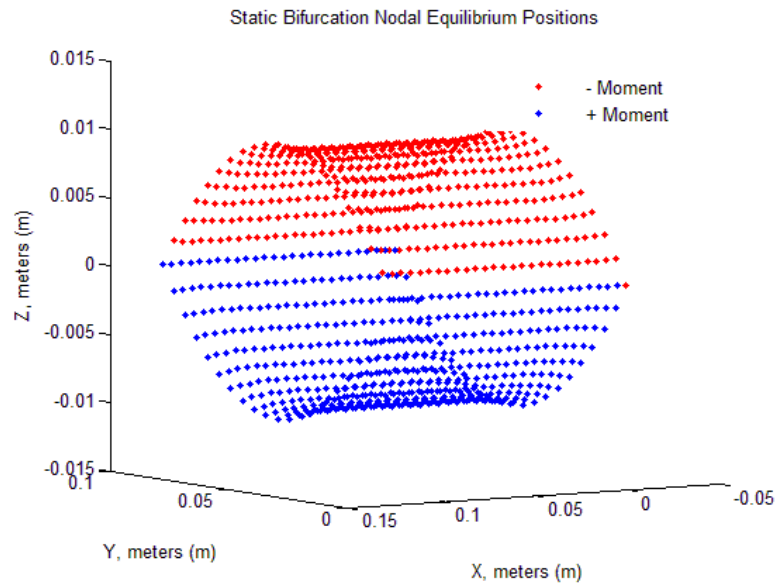


Figure 4.5.l Shell CW & CCW equilibrium positions

swings through the unstable vertical position.

To develop a sense for the volumetric cavity displaced during the shell bifurcation, the maximum deflection positions in the concave up and down equilibrium solutions are shown within Figure 4.5.1. The concave down deflection (red) from a negative shell edge coupling at the TSE and BSE for steps 1 and 3. The concave up deflection results from a positive shell edge coupling at the TSE and BSE for steps 2 and 4. The theoretical volumetric displacement between the concave up and down static equilibrium positions serves as the structural volume displacement per cycle. The volumetric stroke displaces the shell face through the deflection path, shifting the interior cavity volume. As observed within Figure 4.5.h, the elastic strain energy varies through the z displacement.

The positions shown in Figure 4.5.1 correspond to the equilibrium state at maximum deflection step increments. As the shell transitions from the concave up to down configurations, the shell strain energy releases back to a negative value as shown within Figure 4.5.g, returning to the elastically strained state in the deflected equilibrium position. Using numerical integration, the internal cavity volume displacement can then be determined between the concave up and down configurations shown in Figure 4.5.1. Assume that the x displacement is minor by comparison to that of the y and z shell edge nodal displacements; hence, the displacement can be written as the volumetric integral in cartesian coordinates.

$$V = \iiint dx dy dz \quad (4.5.1)$$

Applying the volumetric integral to the initial and final nodal coordinates then gives the plot shown within Figure 4.5.1. The y and z coordinates define the leading edges along the shell surface in motion. The shell edge resembles a parabolic function as shown within Figure 4.5.m. This data is used to construct a curve fit for the nodal output data.

To approximate enclosed volume, consider the concave down position shown within Figure 4.5.m. The axis of rotation is selected as $y = 0$ and the disk method volumetric integral

bounded by the approximated polynomial is used to determine the enclosed volume. Assuming that the shell in the concave up and down positions is equivalent in magnitude and opposite in direction, the volume of a solid revolution using the disk method about the horizontal axis of revolution gives,

$$V = \pi \int_a^b z(y)^2 dy \quad (4.5.2)$$

Fitting the nodal output data for the $z(y)$ coordinates gives the approximated polynomial function, which defines relative deflection along the leading shell edge nodal set. Using a fourth order polynomial approximation to compute volume over the bounded region between $[0,0.0975]$ gives an approximate volume of 6.5248 cm^3 from vertical to maximum deflected position.

The volume enclosed between the concave up and down positions is then twice the computed volume, which gives 13.0496 cm^3 for one completed bifurcation cycle. For the selected shell geometry and material property definition, the shell deflection does not provide the required 75 cm^3 per cardiac beat necessary for a comparable volumetric displacement to that of the human heart. It is then required that the left and right side chamber slave surfaces be incorporated into such a design to amplify the fluid displacement. The cycle frequency may also be increased to give additional volumetric displacement to match that of the cardiac output.

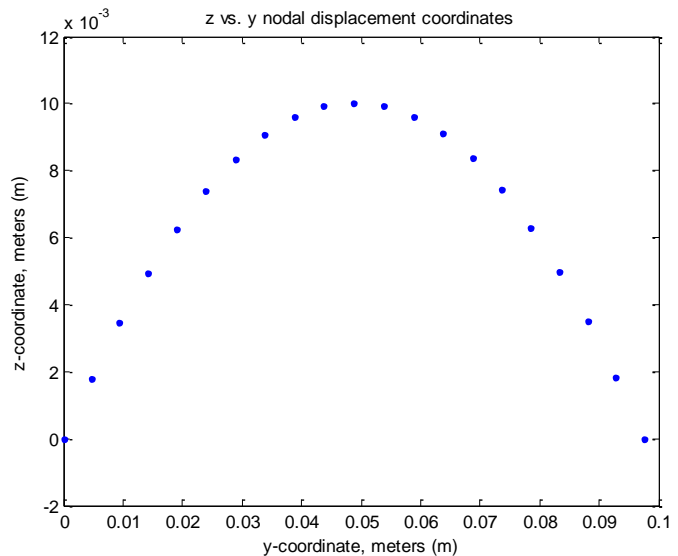


Figure 4.5.m Shell deflection path along surface edge

4.6 INDUCED FLASK BIFURCATION DYNAMIC RESPONSE

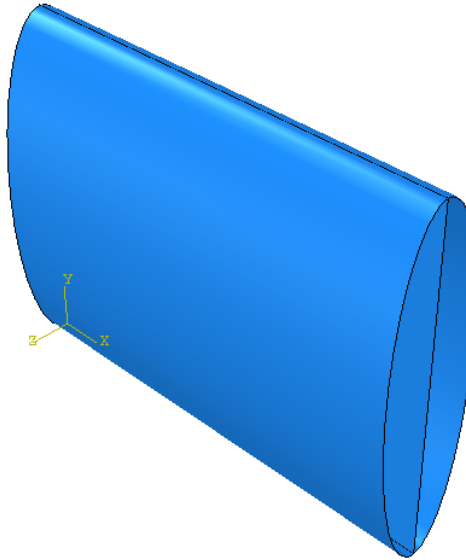


Figure 4.6.a Flask style container

Shell surface motion along the bifurcation path achieves volumetric displacement. The master surface is defined as the center strained shell driving the adjacent fluid. The deflection of this surface does not provide a volumetric cavity by itself which creates an enclosed control volume. Without a housing to encase the fluid region and driving master shell surface, it is impossible to compress the unbounded fluid region. The control volume must feature a minimum of three mechanically

coupled surfaces to compress the fluid region.

An encapsulating container houses the bifurcating master shell surface that is coupled with the simultaneous deflection of neighboring slave surfaces. A tie constraint is applied to the container as shown within Figure 4.6.a, which ties the master and slave surface edges boundary conditions. Initial shell curvature is elliptical to coincide with the anticipated parabolic outward normal master shell bifurcation path. Moment shell edge loading is applied primarily to the master shell surface with the secondary tied constraint driving the slave container surfaces. A CCW moment applied along TSE and BSE gives a parabolic displacement with a single point of inflection. The adjacent container surface is forced into a parabolic deflected geometry with two inflection points, which results from opposing moment loads coupled with a y displacement. Directed in-line to the shell rotation edges, the deflection increases the internal cavity volume. Bifurcation towards the container wall is accompanied by a nearly identical deflection path on the left side chamber.

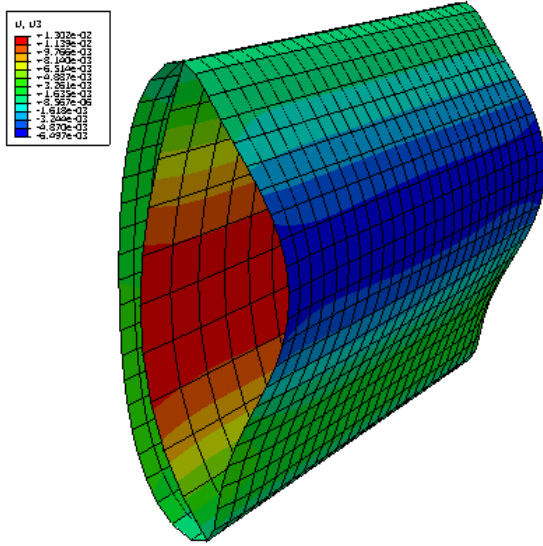


Figure 4.6.b Applied CCW input torque

Opposite to the shell normal, the container wall is forced outward and away from the bifurcating shell with two points of inflection. As shown within Figure 4.6.b, the shell bifurcation towards the left-hand-side (LHS) results from a moment applied along the BSE. The LHS bifurcation path is similar to that of the master surface, uniformly deflecting leftward normal towards the left slave surface. The right-hand-side (RHS) simultaneously

experiences the positive moment that drives the inward deflection on the right.

Initial shell geometry prior to the bifurcation governs the resulting deflection.

From the preceding single surface shell analysis it is known that the shell deflects to a parabolic shape following the bifurcation.

The defined elliptical slave surface shape enhances the fluid ejection ratio, which is defined as the initial internal cavity fluid volume to the final volume at maximum shell deflection. This ratio trends toward a null value as the master and slave surface equilibrium deflections are nearly coincident. The encased fluid region is partially ejected from the chamber with each cycle. The deflection path is

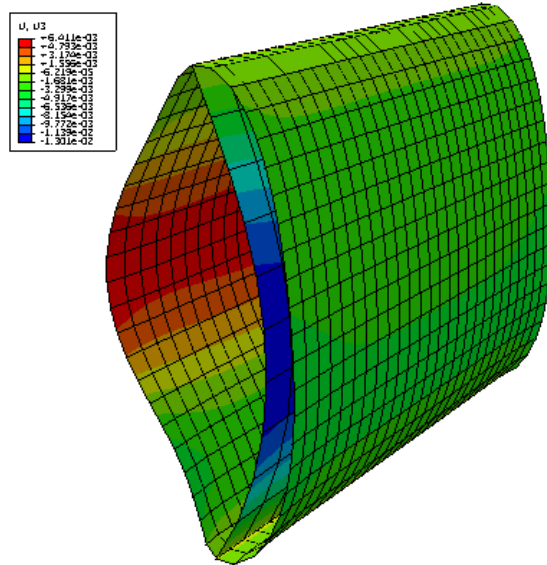


Figure 4.6.c Applied CCW input torque

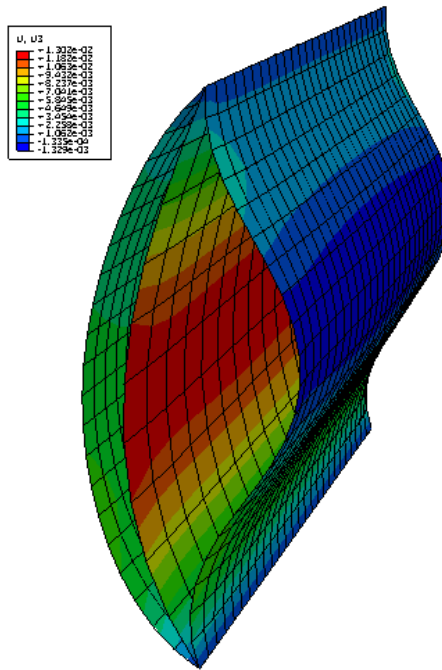


Figure 4.6.d Flask spline applied CCW input torque

carefully selected as to avoid master and slave surface contact, as the interaction could upset device operation.

The fluid expelled from within the heart is only a fraction of the total volume held within the chamber; hence, a complete ejection with the design is not required. Fluid particles lingering between each successive cycle need be minimized as to avoid cumulative damage to captive red blood cell corpuscles. The container loft surface is then modified to reflect a cubic spline between the TSE and BSE with a midpoint offset from the master shell surface

nearing maximum deflection displacement. The selected parabolic apex is determined from the maximum master shell surface displacement and the known inflection points. The geometrical modification places the shell bifurcation path in a similar fitting to that of the container housing in the deflected position. The spline shaped shell definition minimizes internal cavity entrained fluid as the master is driven towards the slave surface. The adjacent slave shell surface undergoes a simultaneous outward projection as shown within Figure 4.6.d. As the master shell surfaces is directed away, the shell edge moment acting on the top and bottom results in slave surface inflection, which

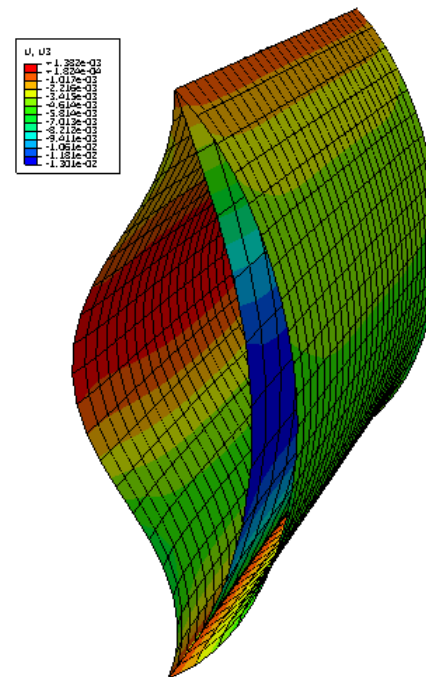


Figure 4.6.e Flask spline applied CW input torque

increases internal cavity volume. Fluid is ejected from the flask left chamber while ingesting fluid into the right side chamber. The process is then repeated as the direction of applied input torque acting on the BSE and TSE is reversed. Cycling CCW to CW induces fluid flutter in the direction of positive pressure. Such a mechanism provides a simultaneous push-pull fluid flow that is driven by impeding master shell surface deflection.

Integral within the direction of fluid flow is the design and orientation of passive check valves installed as to prohibit reversed fluid flow. A check-valve type design is required to passively transition fluid through the device without changing fluid flow direction. There exist minimal shear forces acting against the shell motion which result from no-slip condition along wall boundaries. Only an applied normal force is exerted on the shell pinned at the TSE and BSE. The internal cavity volume is squeezed as the bifurcating shell directs the normal applied force towards the container wall. The primarily fluid motion is induced by the master shell surface;

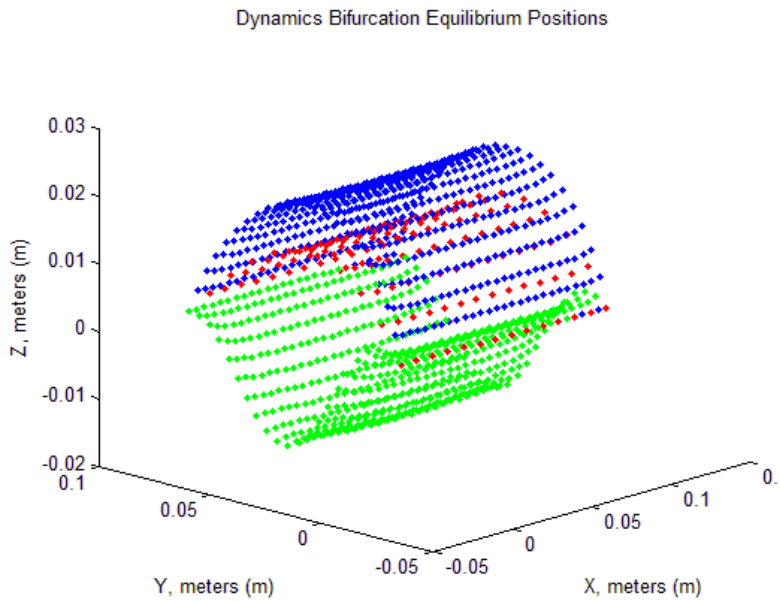


Figure 4.6.f Applied CCW input torque equilibrium position

maximum volumetric ejection.

however, the resulting container slave surface deflections play a significant role in the initial and final internal cavity volumetric displacement. Coinciding the shell concavity fit and direction with the adjacent container surface enables for

The inflection points along the deflected container slave surfaces act as characteristic pivot joints. The slave shell surface features a parabolic curvature, which amplifies the deflection magnitude for given input loading. For a leftward bound master shell surface deflection as shown in Figure 4.6.d, the rightward container cusps outward at the midplane inflection points. The deflection path along the opposite side results in a similar relative motion between the master shell surface and container as shown within Figure 4.6.e. Plotting final step increment displacement for master and slave surfaces provides the relative displacement shown within Figure 4.6.f. The nodal coordinates (X, Y, Z) defined at each step increment is then used to compute the internal cavity volume active within each cycle. The initial shell curvature plays a role in the ejection ratio. Matching the anticipated master surface deflection to the slave surface curvature increases the chamber ejection ratio. If the volume displaced equates to the original enclosed volume, then a work return limiting upper bound is created per the input force required to deflect the master surface. The slave surface observes edge loading applied at the TSE and BSE edges and is forced along the deflection path shown within Figure 4.6.f. The slave surface pair undertakes a bending load applied by the deflected master shell surface. Damaging stresses to the compliant slave element are reduced as the loading is primarily captured within the master shell fixed directly between the left and right chamber walls.

4.7 DEVELOPMENT OF FLUID STRUCTURE INTERACTION MODEL

Prior to developing a full-scale model to characterize the response of fluid to the contrived shell configuration, it is desired that a working computational model be developed to simplify geometry and mock simulate FSI problem. This reduction in problem complexity allows for solution convergence, computational runtime and information interchange proofing prior to use within the full scale simulation. The leading structural deflection is then used to distort the

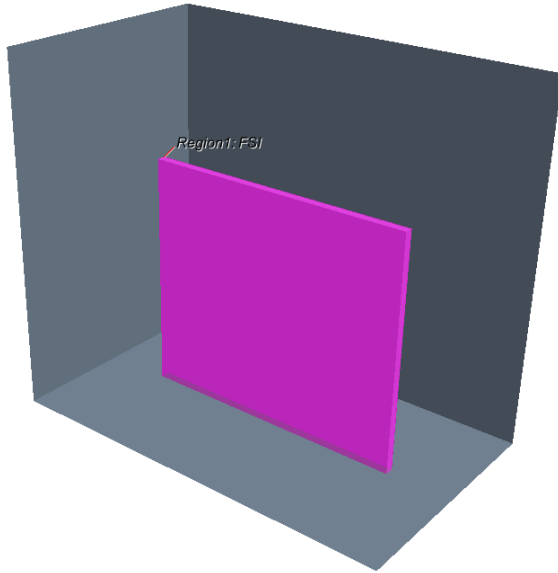


Figure 4.7.a Simple fluid boundary configuration for single shell FSI interface

fluid meshing. The problem is partitioned into segments with the intent that the fluid-to-structural interface will then be applied to a bifurcating fluid mechanism.

The master surface is defined as the center vertical structure which drives the neighboring right and left fluid regions to follow shell deflection shown within Figure 4.7.a. Given that this interface is crucial in developing the fluid-to-structural interface, it is then selected as

the initial rendition to the full-scale FSI model. The input file is created within Abaqus and modified to include the FSI interaction script defining the wetted fluid volume surface recognizable to STAR-CCM+.

Included within the Abaqus input file is a co-simulation step that defines the criteria used in the data exchange. These controls include coupling scheme, scheme modifier, step size and time incrementation. The scheme is selected as a gauss-seidel numerical computation led by Abaqus solution at an incrementation of 0.005 seconds with sub-cycle time incrementation.

The controls instruct the fluid

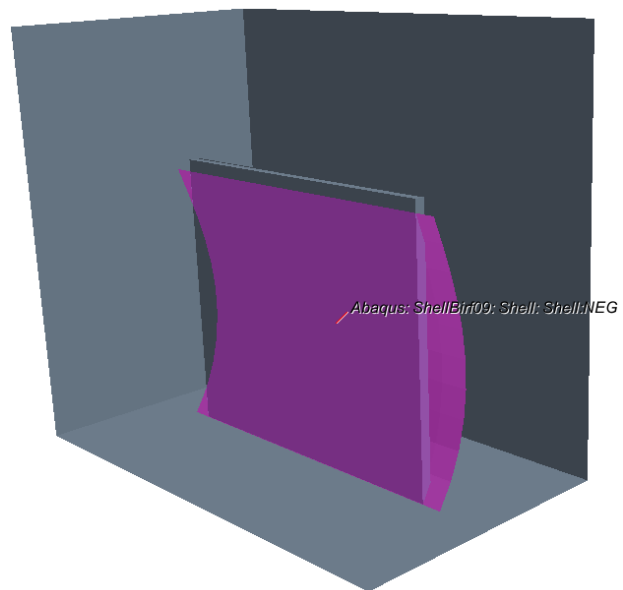


Figure 4.7.b Structural nodal displacement superimposed on the fluid FSI interface

and solid solvers how to talk, when to talk, what to talk about and who should begin the conversation. The information interface controls decrease communication errors between Abaqus and STAR-CCM+ in moderating the exchange of data. The common shared surface that is referenced within the Abaqus input file and the STAR-CCM+ simulation surface serves as the exchange point for the numerical vertex nodal data. Using a shell surface establishes a morphing plane which then distorts as the loading is applied.

The shell surface deflects to a concave geometry as shown within Figure 4.7.b that is then matched by the neighboring fluid mesh. The mesh must morph as the shell deflects downward to accommodate the transition as shown within Figure 4.7.c. Each step incrementation requires that the mesh definition be recomputed for changes to the shell geometrical position. The fluid mesh is matched to the geometric shell definition, requiring that the mesh size be sufficiently small as to avoid computational error and solution divergence. Misaligned fluid finite volume nodes are interpolated to match with the nearest structural finite element nodal definition. Decreasing the mesh size increases the mesh density, which then increases the computation runtime. This relationship in the spatial domain parallels the behavior of mesh density for convergence in the time domain; too large a mesh can lend itself to poor convergence or cell volume distortion. The detailed procedures are utilized to configure the coupled mechanical co-simulation.

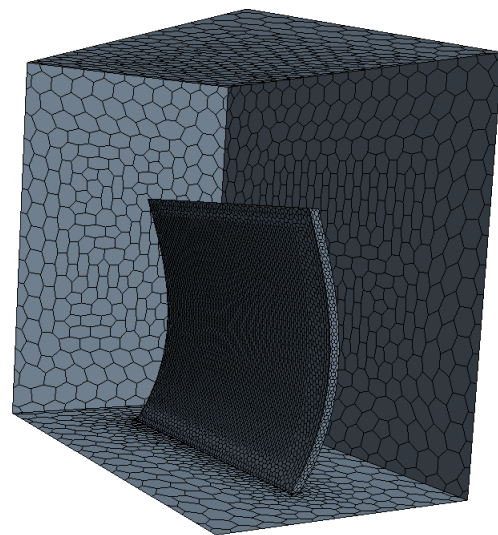


Figure 4.7.c Morphed mesh discretization in the equilibrium deflection position

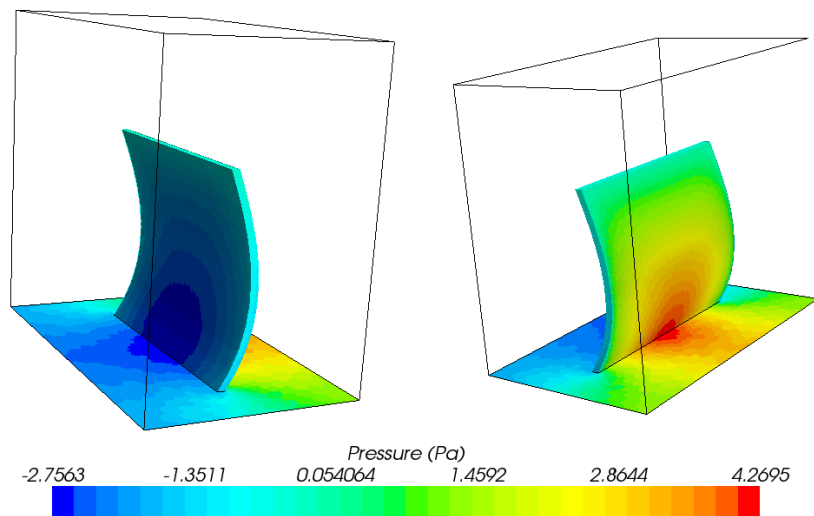


Figure 4.7.d Scalar field pressure output along FSI interface

Separate models for the fluid and solid domains are created to independently define the physical system in its entirety. Using the available STAR-CCM+ software,

the physical fluid model surrounding the shell surface is created. The rectangular three-dimensional container provides six no-slip boundary conditions to encase the housed fluid. Water is selected as the working fluid with laminar Newtonian fluid properties. The mesh continuum defines the parameters used in the analysis for the initial mesh and subsequent alterations to the mesh structure. A polyhedral mesh is applied to the fluid region as shown within Figure 4.7.c, with coarse density along the container six fixed wall definitions and fine mesh along the FSI surface. The increase in mesh density reduces nodal field data interpolation, resulting in increased solution accuracy near the surface of interest.

The FSI surface is part of the fluid region with the morphing function active during co-simulation. The six exterior walls are defined as fixed plane interfaces and are restrained to the initial geometry; hence, the fluid motion cannot impart structural deflection along these surfaces. The physics continuum is defined as a coupled flow, inviscid fluid with cell quality remediation should the structure distort neighboring cell definition. Initial conditions and reference values are initialized in freezing solver and morpher for a single step incrementation. This initializes input parameters used in the implicit unsteady numerical computation of field data output. A set of co-

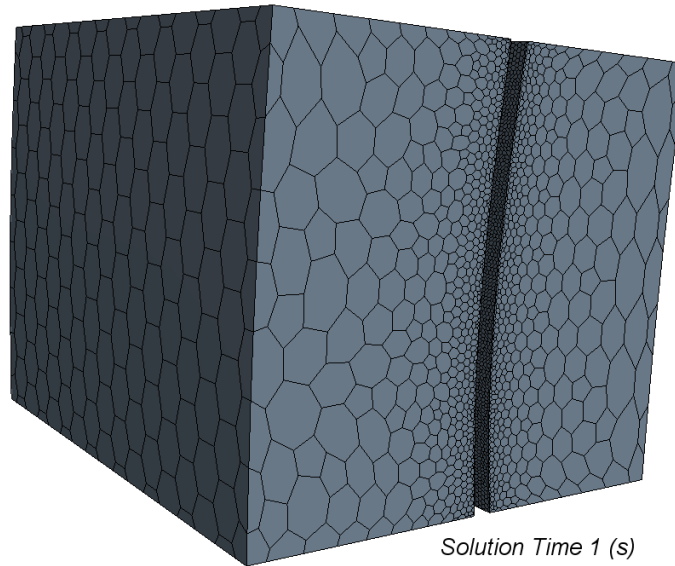


Figure 4.7.e Left and right fluid region morphed mesh discretization in the deflected position

simulation parameters is specified at the FSI interface to exchange field data. Abaqus leads the numerical solver, importing pressure values computed within STAR-CCM+ to compute the next step incrementation. STAR-CCM+ lags in the computation, requiring that the vertex nodal

displacements be known prior to the computation of pressure along the FSI surface. This iterative exchange of importing and exporting solutions allows for the strongly coupled fluid and structural models to be simultaneously solved. The pressure field data for the master shell surfaces along the left and right sides is shown within Figure 4.7.d, which displays the fluid pressure contour plot. Neighboring fluid on the left side surface is pulled while simultaneously pushing fluid along the right side surface. The boundary along the shell top surface permits fluid flow between the left and right side surfaces.

The mesh definition in Figure 4.7.e displays a refined version in which the shell top boundary separates the left and right side fluid chambers. The fixed plane parameters are then modified to be floating type boundaries which conform to co-simulation nodal vertex displacements and defined boundary control vertices. The pressure contour is shown within Figure 4.7.f following the master shell surface deflection and the floating wall deflection that occurs outward from the fluid control volume. The coupled implicit numerical solver is computational tasking, as the software must interactively collaborate to obtain the solution. The

input file defines the coupling scheme, time step incrementation and surface which data is exchanged. Modifying input file allows for direct programming to

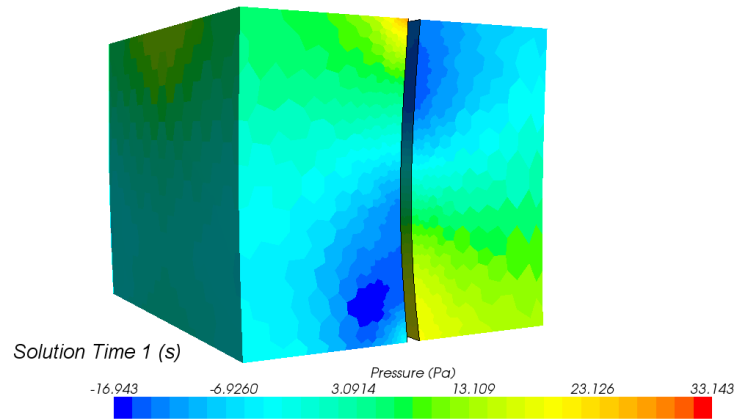


Figure 4.7.f Left and right side computed scalar field pressure

configure the exchange of field data without interfacing with the software.

Abaqus is not preprogrammed for use directly with third party software such as STAR-CCM+; hence, allowing STAR-CCM+ to use the input file format as the basis to define structural geometry, nodal definition, mesh, loading and solver. No further modification to the originating Abaqus defined input file is required to allow the solvers to communicate. Without the continuous exchange of information between the Abaqus and STAR-CCM+, solution would be degraded to a weakly coupled mechanical system. Without such software utilities capable of continuous mesh modification as the structural imparts deformation to the fluid, coincident nodal interchange would be heavily interpolated and the solution accuracy would be poor at best.

Weakly coupled FSI systems do not require the simultaneous coupling featured in strongly coupled FSI systems. The distinction between a weakly and strongly coupled fluid-to-structure system is subtle and can be misinterpreted in mechanical systems. For instance, consider an airplane wing in two separate scenarios; i) in motion and, ii) at rest. While the airplane is stationary, air flow across the surface of the wing does not impart significant structural deflection as the force exerted is negligible. If the airplane is instead traveling at high velocity to achieve lift, then the force exerted on the wing results in notable deflections along the wing structure. However, the velocity induced deflections are still small enough as to not geometrically distort

mesh neighboring the wing surface boundary. The problem can then be solved as a weakly coupled FSI system, in which the fluid continua is influenced by the presence of the structure but the structural deflection is not affected as to significantly alter the fluid flow trajectory.

Consider high velocity fluid flow across a wing that is great enough to induce structural deflections which modify fluid direction. For large deflections to the wing structure in which the flow field is significantly modified, it is then required that the system be solved as a strongly coupled FSI system. Wing structural contortion leads to modified fluid flow trajectory which then impacts lift and drag force.

Consider the proposed FSI between the wetted master surface and the neighboring fluid regions. The objective is to use the deflection of the structure to impart fluid motion; hence, no such small deflection approximations may be used to simplify the FSI as a weakly coupled system. An unsteady implicit numerical solver is required to provide an accurate response between the fluid and structural models. Solution convergence is a function of time step incrementation, spatial mesh morphing and size to actively emulate the amorphous shell surface curvature. Evolving fluid region geometry requires the use of a polyhedral mesher to track finite volumes in which the flow physics is computed.

4.7.1 Geometry Creation

The flow region creation of geometry for the computational fluid dynamics numerical simulation is different than that of the physical domain. Geometry gives the relationship between the fluid and solid continuum, located in the absolute laboratory coordinate system. Fluid region is defined as a spatial domain relative to the adjacent solid physical domain for the problem modeled. The geometry creation allows for the flow dynamics to be developed in the fluid region. A simple geometry of finite length behaves differently than a complex geometry of infinite length. Flow regime is included by selecting the appropriate geometrical length to fit the problem

physics. Each cell is surrounded by faces, which form a grid type pattern throughout the domain. Structured grid requires that the physical geometry maintain rectangular geometrical definition throughout the simulation. The initial geometry can be serviced through the use of a structured, rectangular grid to represent the region. As the defined region begins to distort due to the imparted FSI acting on the region, there is a breakdown in the rectangular cell grid and the volumes become negative as the mesh tries to maintain nodal alignment. Use of a structured finite-volume element is insufficient to capture the fluid response to structure exercising the interface. It is then required that a polyhedral mesh shape be selected in discretizing the fluid continuum.

4.7.2 Mesh Generation

Fluid domain geometry is provided for the fluid regions as a continuum representation of physical part or medium. The domain is then divided into a number of smaller subdivisions which must not overlap to solve the flow physics with the created flow geometry domain. Grid mesh control volume generation represents the region geometry subdivision, which provides a domain rendition of the physical part modeled. The fluid flows in each control volume are solved numerically to determine flow properties which include velocity, mass flow and pressure. Solution accuracy is heavily governed by the mesh density within the computational region. Unstructured grids are built from hexahedral prisms, tetrahedral and geometry-based polyhedral mesh definitions. Angles between the wall and grid line must be near 90 degrees to avoid mesh distortion and numerical inaccuracy due to element skewness. Maintaining consistent mesh discretization gives a solution to the governing set of partial differential equations independent of the mesh geometry. In the volume, the energy norm error is aimed at maintaining a constant value within all elements trending towards a null value.

4.7.3 Fluid Properties & Physics

The underlying flow physics is unique to the system fluid flow, which may be inviscid or viscous, transient or unsteady, compressible or incompressible, laminar or turbulent. The definition of fluid properties defines the meshed region and gives a multitude of behaviors which the continuum must satisfy. Water has a unique set of fluid properties aside from that of compressible gas; hence, the appropriate definitions and flow relationships are defined within the input pre-processor. The density and dynamic viscosity are amongst the two main criteria in defining viscous fluid flow. Quantifying key material parameters characterizes how the fluid responds to the modeled problem physics.

4.7.4 Boundary Conditions

Fluid flow boundary conditions are required to accommodate fluid behavior entering and exiting flow domains at the inflow and outflow boundaries. A boundary can be represented as an open flow region or an impenetrable wall adjacent to neighboring solid along the region periphery. This solid need not be stationary as wall deflection is permitted when fluid-structural type interactions occur along the fluid boundary. Contact between the wall and the fluid is enforced to maintain selected boundary conditions. The inlet fluid velocity is defined to give a reasonable estimation for fluid which enters the flow domain. At the outflow boundary which observes fluid departure, a specified relative pressure is defined. The inflow and outflow pressure or mass flow rate boundary conditions are determined to establish relative pressure values along the boundaries. This ensures mass flow into and out of the region across fixed pressure boundaries. Subsonic and supersonic flow can be specified as part of the flow regime; however, only subsonic flows are considered in this analysis.

4.7.5 Computational Fluid Dynamics Solver

The solver procedure executes the initialization, solution control, computation monitor, and convergence criteria in obtaining the numerical solution. Should the solution fail to converge, then modification of the solution parameters or region mesh is required. Fluid flows are nonlinear and require treatment of numerical phenomena to be resolved through an iterative solution. Flow boundary conditions must be initialized prior to the first simulation step increment. Initial conditions can be freely selected; however, providing an initialization guess near the solution decreases computational run time and increases convergence rate. If poor initial conditions are elected to start the numerical solver, then divergence or excessive run time results. Finite-volume methods give the algebraic equations which govern the fluid flow differential equations. Application of finite-difference approximations to a finite volume cell in space provides transport variable surface fluid determined using the numerical interpolation methods. [12]

4.7.6 Numerical Methods for Computational Fluid Dynamics

In the solid-mechanics approach, the finite-element method is utilized to obtain solutions for the shell bifurcation structural response. The objective is to minimize the difference between the exact solution and the base shape function for each finite element. Fluid-mechanics problems are local conservative, which is not necessarily a property of finite-element methods as the difference between the base functions and the exact solution is minimized in a global sense.. Numerical solutions to the governing set of equations use the finite-volume discretization to give small volumes defined as mesh cells. At each cell definition, the complex partial derivatives for conservation principles can be simplified to an algebraic contribution; solving a set of linear algebraic equations to represent the governing partial differential equations. Solutions to this set of equations are performed through numerical iteration, tabulating numerical error as part of the

solution. As the size of cell decreases, the known incorporated error is significantly reduced from the solution.

The Gauss-Seidel algorithm is an iterative method used to obtain the numerical solution for nearly all commercially available CFD codes. Gauss-Seidel algorithm uses initialization as a starting guess to give a numerical value for all cells, then iterating until the error converges below the user-defined error criterion. The iterative numerical solution scheme begins with a guess initialization for each node. The system of equations is then solved for the first node by using the initial guess values for neighboring zero and second nodes. [13] The same set of equations can be solved for the second node using the computed value for the first node with an initial starting guess value for the third node. This process is repeated until a convergence criterion is satisfied and the numerical solver can terminate iteration scheme. Residual errors are computed at each step iterate to indicate how close the approximate solution is to achieving numerical convergence.

4.8 ENCAPSULATING FLUID CONTAINER DYNAMIC BIFURCATION

Morphing surface geometry plays a significant role in the resulting change in internal chamber volume. The loads and boundary conditions applied as shell edge loads along the master surface does not convey the most practicable configuration for an internally actuated biomedical device. The aforementioned analysis makes the presumption that the loading and boundary conditions can be enforced on the device exterior. Applying the exterior load requires that additional space be occupied to fit the tied shell geometry with an external load sufficient to replicate the observed shell deflection path. This severely limits the utility of such a device and requires that the applied loading be induced internally along the master surface shell definition to minimize spatial design requirements. In place of the shell edge load applied along TSE and BSE, a uniform shear surface traction load is created along on the master surface as shown within Figure 4.8.a. The master and slave surfaces are modeled as a single extruded construct.

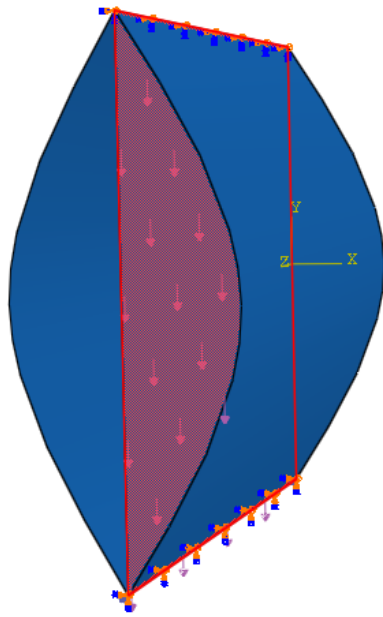


Figure 4.8.a Applied master shell surface traction

The tie constraint that was previously applied to TSE and BSE shell edges is now replaced by a single solid continuum. The stress and strain observed by the master surface is directly propagated to the neighboring slave surfaces. The shell edge load which emulates an applied input torque is replaced with a concentrated input torque at the top and bottom side outermost point nodes. Placing the applied input torque at a single nodal definition gives an accurate response to how the shell responds to an input torque point load.

The original presumption was that the motor input torque could be modeled uniformly along length of shell edge; however, this fails to convey the true physics behind how such a load is applied to the system. The motor input load is applied along a single point on the shell edge and not along a line, which increases localized stresses at the point of applied input torque. The simplifications stated in the preliminary analysis give excellent illustrations as to how the device should function. Modifications reflect current state mechanical actuators that are available to deliver the desired loading parameters. The power source is exclusively electric, in which the aid of onboard hydraulic or pneumatic systems is not permitted within the actuator selection. To induce the mechanical strain along the master surface, the use of a piezoelectric patch may be utilized.

The original presumption was that the motor input torque could be modeled uniformly along length of

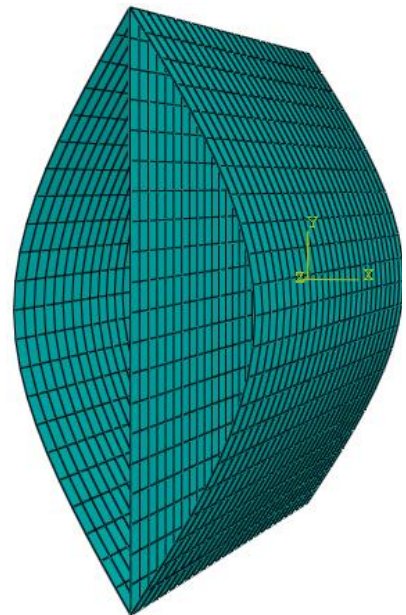


Figure 4.8.b Master & slave surface mesh discretization

An electric motor coupling applied to a point along the master surface top and bottom shell edge can provide the necessary input torque required to upset the desired shell deflection path.

It should be noted at this point that the design provided does not fully disclose the final geometry or material properties. The intent is to illustrate how the use of a bifurcating shell element can be used to generate fluid flow through an encapsulated fluid region. The final material properties and geometrical definitions are subject to design constraints such as fatigue longevity and corrosion resistance, which are not to be discussed. Modification of the master and slave surface material properties alters the mass and stiffness matrices, which then influences magnitude but not the characteristic deflection response. It is then nonessential that the material and geometry properties be definitively selected, as the objective is to understand the physics and to illustrate the concept. Illustration provides a precursory glimpse as to how such a mechanism can be used to impart fluid flow.

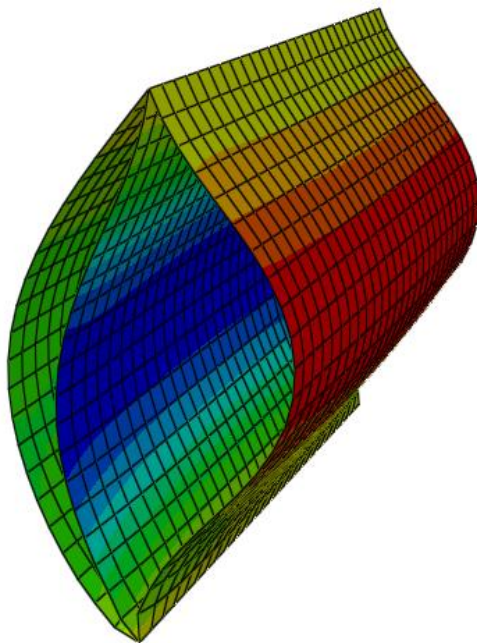


Figure 4.8.c Applied CCW input torque

Consider a fixed control volume soda can that is filled without separation between the housed fluid and container. The container fully envelopes the encased fluid region such that all fluid is tightly bounded and cannot escape. The fluid is held at pressure within the can and the stress-strain relationship experienced by the can abides by the biaxial state of stress. The hoop and axial stresses are a function of pressure, size and cross-sectional thickness of the can. Material parameters regulate the magnitude of stretch that occurs in the circumferential and radial directions. The induced strain associates the state of stress to a linearly proportional modulus of

elasticity. As the pressure increases within the can, the induced strain undergoes a proportional increase in magnitude. The can stretches as the pressure is increased in accordance with Hooke's law, elongating in the axial direction while radially expanding the outward normal. The fluid region exerts an applied pressure on the solid envelop, which results in structural deflection. The structural definition lags that of the applied pressure transient acting along the can inner peripheral interface.

Consider the outcome when the can is dropped from a considerable height to the ground. Upon impact, the structural undergoes permanent deformation from that of the initial geometry and forces structure inward towards the fluid. The sudden inward contraction provides an impulse to the enveloped fluid region. In an attempt to occupy the original fluid volume within the reduced and distorted volume envelope, the incompressible fluid exerts an opposing pressure along the interfacing wall. This increases the stress and strain experienced through the cross-section to the point at which the fluid breaches the solid envelope. The fluid conforms to the envelope geometry until the structure itself requires that the fluid be compressed. The can is an example of a fixed boundary control volume in which compression to the contained fluid is channeled through the structure cross-section.

The volumetric envelope defined for this analysis features geometry as shown within Figure 4.8.b. The forward and aft sections between the master and slave surfaces do not contribute to the fluid contraction, as these boundaries must feature passive check-valves to regulate the flow of fluid through the chamber ports. Fluid resistance through the valve is experienced by such a valve design, which results in turbulent flow presumptions. To maintain laminar fluid flow through the chamber, it is assumed that there is no such obstruction in the flow path to upset fluid turbulence. In essence, the analysis is performed on a soda can without the top and bottom sections. The pressure and mass flow rate magnitudes experienced are significantly reduced from that of an enclosed control volume. Omitting these surfaces from the analysis gives

numerical results which are stabilized and do not suffer from residual error or negative cell volumes. The add-in check valve design and construct is briefly discussed within sections to follow, giving a precursory look at how the valves can be incorporated into the forward and aft chamber envelopes.

Separation of the slave from master surface deflections along the top and bottom locations can be used as a structural actuation to open and close the passive valves. As shown within Figure 4.8.c, the separation between the left-half and right-half envelopes provides a fitting location for valve placement and actuation. The red contour bands on the right-half slave surface denote a positive x direction nodal displacement and the master surface blue contour bands display the negative x direction nodal displacement. The left-side slave surface maintains similar geometry as the master surface is stressed and the neighboring chamber deflects. The design is to follow the prescribed master and slave surface deflection paths. The valves must be mechanically compliant and pressure actuated to force the valves open and then to quickly shut the valve to avoid fluid mass flow reversal.

4.9 IMPLICIT DYNAMIC FLASK DEFLECTION FLUID RESPONSE

The interaction between the structure and fluid continuum is a complex relationship that requires the use of implicit solver software tools to compute. The mathematical background in solving such problems along with the theory is discussed in the preceding sections. The constitutive principles govern the laws of fluid and structural mechanics. Coupling the fluid response to that of the structural nodal displacement requires that the fluid and structure actively receive and transmit field data in an attempt to accurately solve the system physics. For each implicit step incrementation, the governing constitutive equations must be solved to reach an interim equilibrium solution. A computational programming tool is used to automate the numerical solver.



Figure 4.9.a Structural nodal displacement superimposed on the FSI interface

The outer shell slave surface forms the leftward bound on the fluid container. Obtaining a solution to the non-linear structural deflection of the thin plate or shell element can be performed independently of the fluid system and is shown in Figure 4.9.a. The independently solved structural deflection introduces an artificially high deflection magnitude when neighboring fluid region is not included within the solution. The structure features a mass inertia that is relatively small when compared to that of the fluid; hence, the fluid tends to dominate the mass matrix $[M]$ in the solution and cannot be omitted from the numerical simulation. Though the structure mass inertia is insignificant to the overall shell deflection, the induced traction shear stress along the mid plane master surface generates a mechanical increase in the stiffness matrix $[K]$. This increase in the stiffness matrix is sufficient to overcome the fluid mass $[M]$ and damping $[B]$ matrices. The ejection of fluid from within the chamber occurs as the structure becomes unstable and senses the neighboring incompressible fluid. The structural deflection as shown in Figure 4.8.c gives the deflection path void of any such fluid contact with the master and slave shell surfaces. This deflection serves as an accurate representation of how the structure would respond if no such fluid region is encapsulated within the container.

The outer shell slave surface forms the leftward bound on the fluid container. Obtaining a solution to the non-linear structural deflection of the thin plate or shell element can be performed independently of the fluid system and is shown in Figure 4.9.a. The independently solved structural deflection introduces an artificially high deflection magnitude when neighboring fluid region is not included within the solution. The structure features a mass inertia that is relatively small when compared to that of the fluid; hence, the fluid tends to dominate the mass matrix $[M]$ in the solution and cannot be omitted from the numerical simulation. Though the structure mass inertia is insignificant to the overall shell deflection, the induced traction shear stress along the mid plane master surface generates a mechanical increase in the stiffness matrix $[K]$. This increase in the stiffness matrix is sufficient to overcome the fluid mass $[M]$ and damping $[B]$ matrices. The ejection of fluid from within the chamber occurs as the structure becomes unstable and senses the neighboring incompressible fluid. The structural deflection as shown in Figure 4.8.c gives the deflection path void of any such fluid contact with the master and slave shell surfaces. This deflection serves as an accurate representation of how the structure would respond if no such fluid region is encapsulated within the container.



Figure 4.9.b Left side fluid region mesh discretization



Figure 4.9.c Morphed mesh discretization in the deflected equilibrium position

The structural solution was obtained in advance to insure equilibrium convergence. For the coupled FSI system to solve, it is required that the structure maintain convergence and stability during the structural analysis. For a given traction shear force applied parallel to the master shell surface, there is a corresponding nodal displacement of the mechanism with and without the neighboring fluid continua. The structural model outputs the nodal displacements to the fluid model, which then computes and transmits fluid response pressure and wall shear stress field data to the structural model. The objective is to generate

simultaneously a positive and negative chamber pressure induced on the left and right sides, respectively for an applied CW input torque. The fluid continuum is represented by two regions for the left and right chambers. A boundary separates the left and right fluid regions along which the structural nodal displacement can be applied to the master surface. Each fluid region consists of a set of boundaries, which maintain conditions along the surface as specified by the user input parameters. The boundary demarcations are defined along each surface for the port, wall and fluid-structure interface. To illustrate the pressure

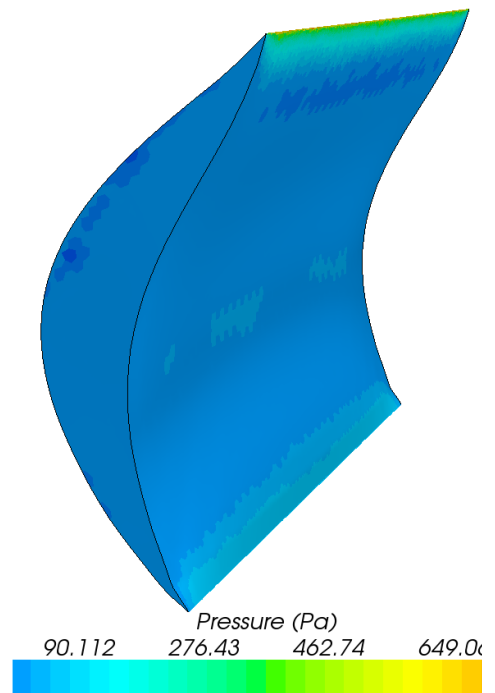


Figure 4.9.d Scalar field pressure

applied to the chamber halves, the boundaries assume that there is a stagnation inlet at each port opening.

An infinite region of mass continuity is then presumed to exist forward and aft the porting boundaries. The master and slave surfaces are specified as wall boundaries driven by the co-simulation field data obtained from the nodal vertex displacement. A coarse mesh is applied in the inner fluid region with a fine mesh towards the fluid-structural interaction master and slave shell surfaces. As the structure deforms, the incompressible encapsulated fluid conforms to the change in container geometry. Should the mesh density be too large alongside the nodal displacement driven fluid-structural interaction surfaces, then the solution fails to converge and erroneous numerical residuals result. Reducing the mesh base size alongside these surfaces precludes numerical instability or solver divergence. A small time step iteration of 0.005 seconds is selected to obtain equilibrium and to maintain stability throughout the simulation. Large time steps increase solution convergence rate, but introduce numerical divergence between iterates.

The left and right chambers are solved simultaneously for two independent fluid regions. The fluid regions sense the container and contract or expand to accommodate the change to the original control volume geometry. To illustrate the pressure versus volume relationship for each chamber, the analysis is independently computed for the left and right fluid regions. As shown within Figure 4.8.c, the master surface deflects toward the leftward chamber. The fluid volume contained between the master surface and the left chamber wall contracts inward as shown within Figure 4.9.c from the initial mesh definition in Figure 4.9.b. The chamber volume decreases during the inward contraction and the resulting pressure increases through the cycle. The pressure profile is nonlinear as the master surface bifurcation achieves solution equilibrium.

The volume reduction simultaneously pushes fluid outward from the chamber through the forward and aft ports. This increase in pressure as shown by the contour scalar output map within Figure 4.9.d, displays the relationship

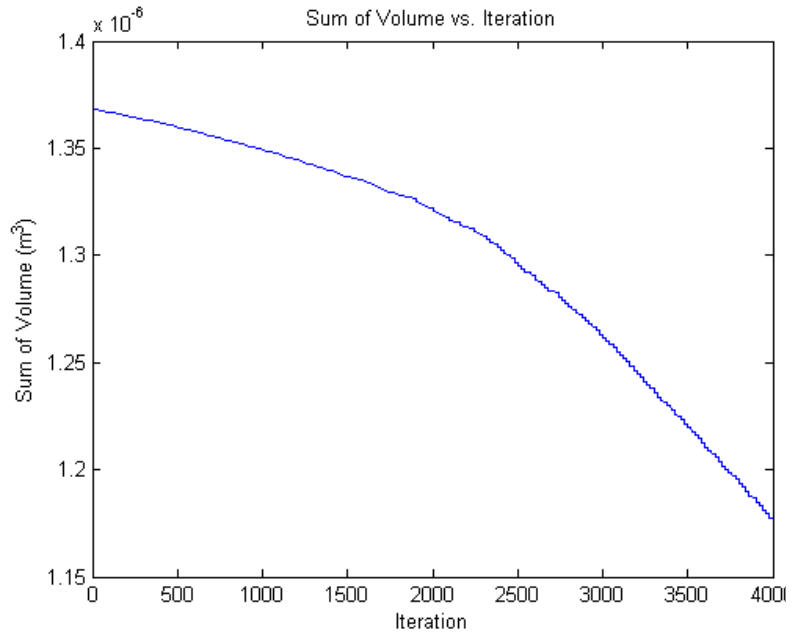


Figure 4.9.e Applied CCW input torque left side fluid region volume decrease

between chamber volume contraction and subsequent pressure increase. The relationship is similar to the pressure-volume characteristics required in replicating the nonlinear periodic heart rhythm.

A similar exercise is performed on the left chamber for the reciprocating stroke in which the master surface bifurcates away from the leftward chamber wall towards the right by reversing the applied input torque from CCW to CW. The left and right chambers are maintained at equal volumetric dimensions to maintain symmetry assumptions and to reduce numerical simulation run time. Provided herein is an assortment of simulation results for volume, pressure, volume change, mass flow rate and flux through a single chamber for one-half cycle. Output is given at the region level and does not include flow modification to in-line valve or regulator type devices. The pressure magnitude is then significantly reduced given that the container is not sealed at the port boundaries. The incompressible fluid is permitted to pass through the ports unimpeded by flow obstructions such as a passively actuated valve.

The characteristic pressure profile does maintain an accurate representation of how the fluid control volume responds if the regions were closed along the port boundaries; however, the scalar field data magnitude is reduced given the loose port side control vertices.

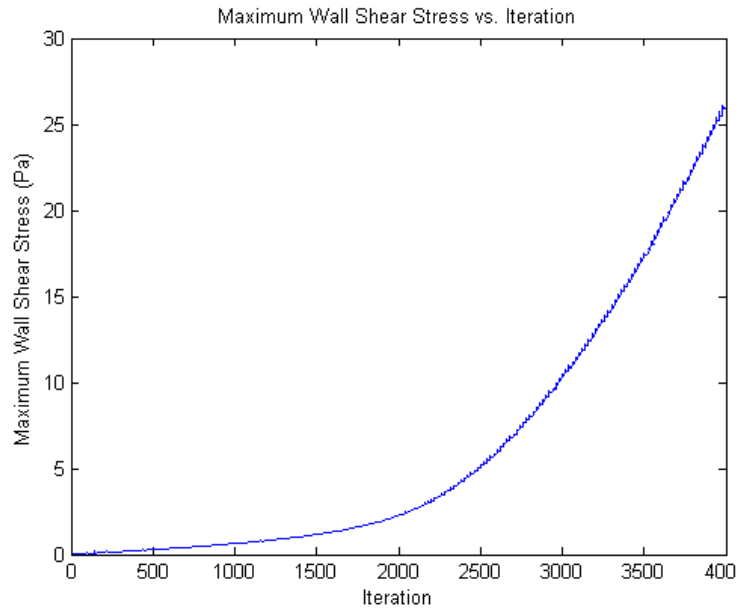


Figure 4.9.f No-slip wall shear stress increase

The sum of volume throughout the numerical simulation is shown within Figure 4.9.e, which gives the change in interior volume as the master surface moves toward the leftward slave surface. The decrease in volume results in a volume integral of pressure computed for the fluid region as shown in Figure 4.9.h. The volume integral of pressure per definition is the computed energy or work required in Joules (J). This is computed for the entire fluid region and takes into account the fluid density and stroke per the inputted nodal displacements. Once the master shell surface reaches the bifurcation loading, the input energy required to onset the deflection is decreased and the mass flow rate is rapidly increased. This relationship is shown in Figure 4.9.h, where the work at approximately the 2500th iterate decreases with an increasing mass flow rate as shown in Figure 4.9.g. The maximum wall shear stress detected along the fluid-structure interaction surface is shown in Figure 4.9.f for all finite volumes. As the master surface forces fluid from within the chamber, the resulting wall shear stress exponentially increases up to a maximum value

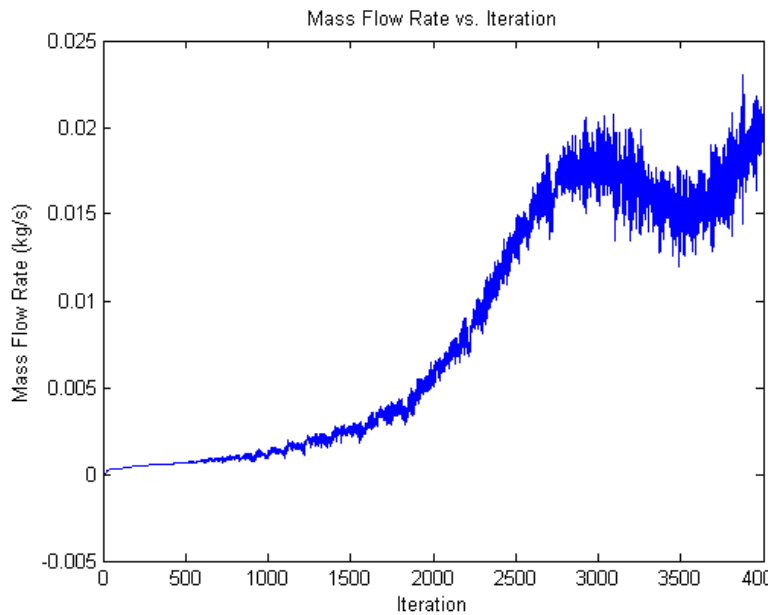


Figure 4.9.g Mass flow rate ejection through virtual ports

increase within the chamber. The embedded thin mesher is used in geometries that are predominately thin or include thin structures, generating a prismatic type of mesh. The thin meshing model allows thin regions in the geometry to have a prismatic volume mesh as to improve the overall cell quality and reduce cell count. Polyhedral meshes provide a balanced solution for complex mesh generation problems in non-rectangular geometries as shown within Figure 4.9.b and Figure 4.9.c.

As the mesh distorts to suit the morphing geometry, the polyhedral mesh density and shape is modified. The mass flow rate through the aft and forward port locations is shown within Figure 4.9.g, which appears to be noise. This data fluctuates as the boundary is an imaginary plenum of fluid upstream and downstream the fluid region. Without a means of passive or active fluid flow regulation from the control volume, the flow direction varies in accordance with the equilibrium residuals in the continuity equation. If the ports were sealed along the boundaries, then the mass flow rate solution would include less severe residual error. Cell volumes along the

concluding the numerical simulation. This is anticipated given that a no-slip fluid boundary condition is imposed along the co-simulation fluid-structure interaction wall surface.

The wall shear stress increases as mass flow rate and pressure

port boundary constantly change direction and give a fluctuating mass flow rate, which can be used to determine the characteristic curve profile and magnitude as shown within Figure 4.9.g.

The polyhedral meshing model utilizes an arbitrary polyhedral cell shape to build the core mesh. Surface remeshing is used with specific conformal meshing obtained for multi region cases. Physics models are employed within the fluid system to identify the equations of state needed to complete the CFD analysis. The model features constant density, implicit, unsteady, laminar, incompressible presumptions to identify the bounded set of equations required to describe how the fluid is to respond to the structural nodal vertex displacements. Water is selected as the working fluid, not in that it is a perfect representation of blood; rather, that it is a reasonable approximation for characterizing the mechanism response to the induced deflection paths. Any nonlinearity should be the direct result of design and not the selected fluid properties. The provided inputs were carefully selected and justified as to avoid any misuse of the numerical solver.

The simulation is an insightful tool to illustrate how the thin plate or shell deflection is used to impart motion of house chamber fluid volume. The pressure amplitudes vary slightly if the assumed Newtonian fluid is realized as a non-Newtonian fluid of varying density; however, the directionality of pressure and fluid motion will be minimally affected by such an approximation. The pressure magnitudes presented reflect only the shell surface actuating pressure and not the observed outlet pressure at the theoretical valve cross-section. The addition of hydraulic effects would then give a significant rise in the observed pressure through valve orifice. This reduction in nominal valve cross-section invalidates the laminar flow assumption, as the fluid then would exhibit turbulent fluid flow response through the orifice. Valve design and fluid region closure then permits the reduction in nominal port flow area to amplify the pressure amplitude and to regulate mass flow rate. The volume integral of pressure is plotted versus the sum of volumes, which gives the relationship between enclosed volume and work potential. The

plot is shown within Figure 4.9.h, which gives the inversely related pressure to the sum of finite volumes.

The volume integral of pressure takes into account an integral scheme which averages the finite volume numerical solution collectively amongst the individual cell

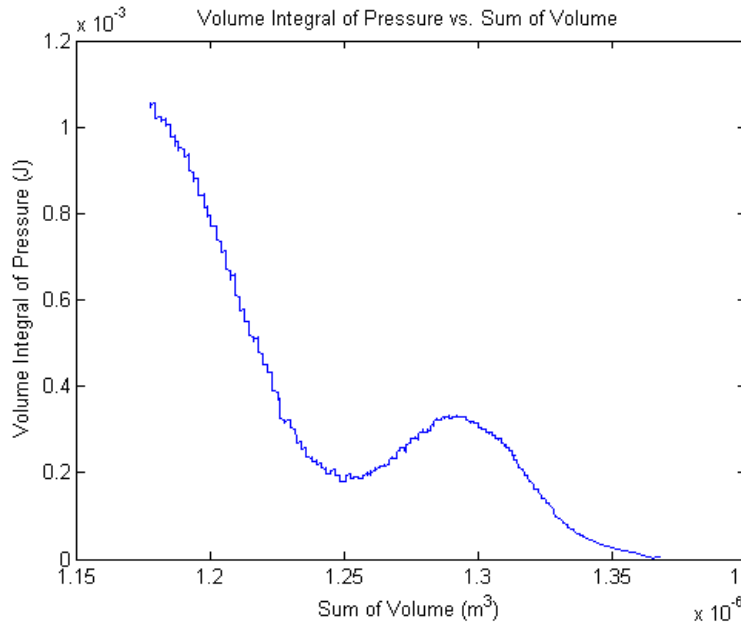


Figure 4.9.h Fluid volume contraction pressure decrease

volumes. By virtue of the numerical solver, individual volumes feature residuals to the continuity, mass and momentum equations. An averaging scheme seeks to minimize the error between the inner volume discretization and to give a solution that is computationally accurate. The implicit numerical solver does not give an exact solution, as it is a numerical approximation which iterates to minimize the residual error in the computation. Increasing the number of iterates for each step incrementation decreases the residual error in the numerical solution and increases computational run time. As shown in Figure 4.9.h, there appears to be small steps between each increment which represents the equilibrium solution for each solved step incrementation. Steps that are too large decrease the accuracy in the solution and provide a coarse representation which results in solution divergence. Increasing the step count provides increased solution resolution; however, expends excessive computational run time when selecting a small step incrementation size. The solution time for one-half cycle is one second and is referenced as the simulation step time. This one



Figure 4.9.i Morphed mesh discretization in the deflected equilibrium position

residuals is caused by the cell volume change in mass flow magnitude and direction as the fluid is moved through the chamber port boundaries. The induced master surface structural bifurcation is borderline stable and nonlinear; hence, the fluid region becomes attenuated to this behavior and

second step time is divided into two hundred step increments equal to 0.005 seconds in length per time step incrementation.

The structural equilibrium solution is determined at each step incrementation and outputted to the fluid solver, which then further divides the step increments into twenty sub-iterates to reach the fluid equilibrium solution for each step incrementation.

Since the fluid solver may abruptly generate erroneous solutions at any step incrementation, the residual error is closely monitored for convergence. As shown in Figure 4.9.g, the mass flow rate solution goes from a steady increase to a fluctuating numerical solution. The increase in equilibrium

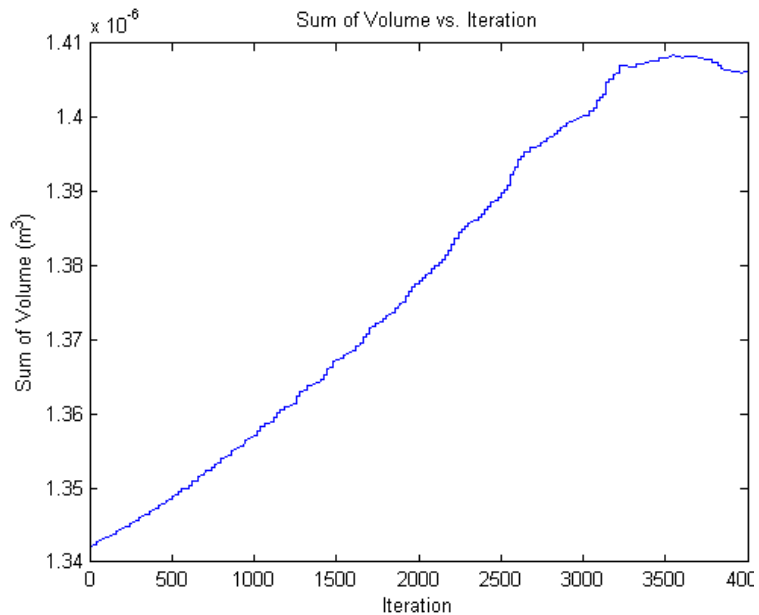


Figure 4.9.j Applied CW input torque left side fluid region volume increase

overcompensates the step increment numerical solution. The direction of the applied input torque is reversed for the same fluid region as shown within Figure 4.9.b original mesh geometry.

The deformed mesh configuration is shown within Figure 4.9.i, which displays a similar region distortion as predicted within Figure 4.8.c structural deflection. Though the observed FSI deflection is less than that of the independent structural deflection, the concave and shape is identical. In the reversed input torque deflection as shown within Figure 4.9.i, the master surface is driven towards the right side as the slave surface is deflected into a nearly vertical position.

Deflecting the slave surface into the vertical position then stores energy within the slave shell surface that is released once the applied moment is removed. The volume region between the left chamber master and slave surfaces is expanded as the master surface moves away from the slave surface. This relationship is shown within Figure 4.9.j, wherein the sum of volumes is increased linearly up until the slave surface reaches a vertical configuration and the volume increase plateaus near the 3000th iterate. The heart features a similar volumetric ejection as it nears the maximum systole contraction.

The volume integral of pressure plot as shown in Figure 4.9.k performs as expected for the first 2200 iterates, then changes direction and becomes positive. The negative pressure experiences a filling stage followed by a rapid

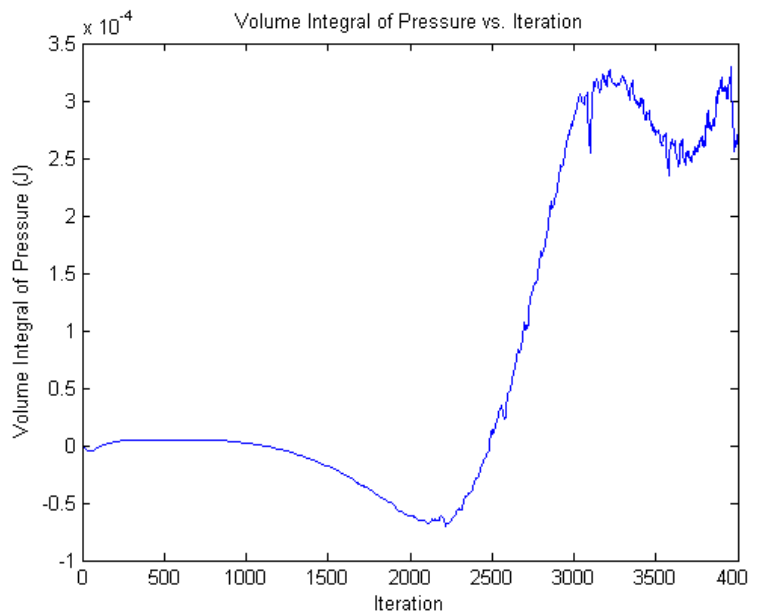


Figure 4.9.k Pressure generated fluid work profile

transition to a positive pressure with increasing volume. This outcome is not anticipated and fails to make interpretable physical sense, though it is not the victim of a numerical simulation residual error buildup or software misuse.

This phenomenon acts contrary to the anticipated deflection; however, it is worth including in this discussion as its implication may be better understood upon further investigation. The maximum wall shear stress shown within Figure 4.9.1 is similar to the characteristic behavior as shown within Figure 4.9.f for the no-slip condition prescribed along co-simulation wall definitions. The maximum wall shear stress increases exponentially during the simulation.

As the master surface pulls away from the slave surface, the shearing action increases magnitude along the fluid-to-structural interfacing boundaries. The increase in wall shear stress is not desirable; yet, it is tolerated to impart motion to the fluid region. Any such fluid motion which occurs across the structural interface wall boundary will inherently generate some degree of shear stress; though, the magnitude is significantly lessened in using an applied normal force along the master surface. The observed shear stress is not the result of a slicing action typical to that of a

blade; rather, the shear stress is attributed to the no-slip condition and the walls proclivity to gripping fluid in motion. The wall shear stress is the surface attempting to shear fluid neighboring structural boundary. Any contact with the fluid adjacent to a moving

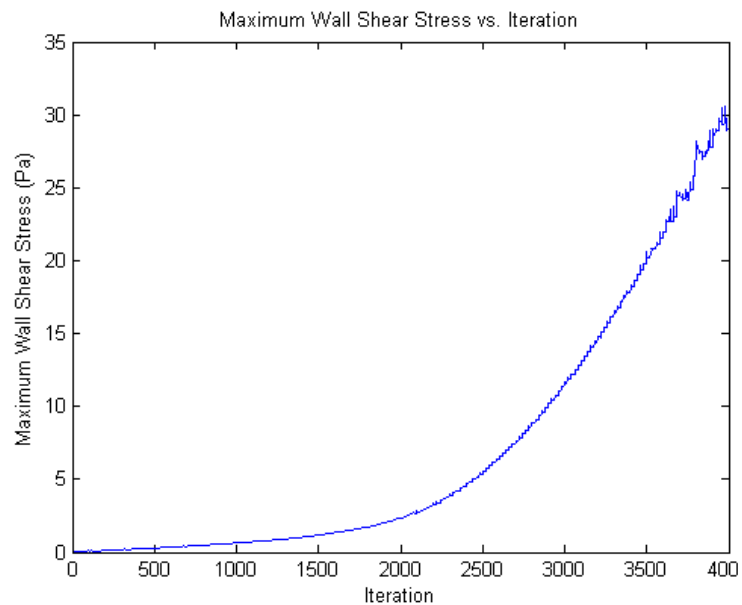


Figure 4.9.1 No-slip wall shear stress increase

surface will experience shear stress that can damage the housed fluid particles.

The key is to maintain acceptable limits for minimizing the effective shear stress along the surface in motion. In a centrifugal type impeller pump, the blade velocity relative to the blood occurs at a rate of several hundred revolutions per minute to maintain the required fluid flow. The relative impeller velocity shears through the fluid to create a positive pressure between the pump inlet and outlet ports. This leads to increased fluid turbidity that can further damage delicate red blood cell corpuscles. Acceleration of the fluid particle in such a design is directed outward from the impeller rotational axis, increasing the particle impact force with the housing fluid container. This centrifugal acceleration effectively smashes the fluid particles following the impeller slicing action. Heavier fluid particles which coagulate from prior loop passage are forced to the outer slip plane at a faster rate. The acceleration forces any healed fluid particles that were previously damaged in a prior loop circulation to the interface between blade and housing. In the proposed alternative method for achieving fluid motion, the violent shearing action and rapid acceleration of damaged fluid particles is replaced by a squeezing motion that attempts to minimize slip plane velocity and the resulting red blood cell corpuscle coagulation. By design and aside from any material considerations, the nominal decrease in applied wall shear stress for the proposed design is significantly decreased to that of the aforementioned centrifugal pump wall shear stress.

The fluid region directly adjacent to the structural experiences maximum wall shear stress and locations near the fixed bottom side edge experience shear stress of decreased magnitude. The plot shown in Figure 4.9.m propagates the phenomenon as shown in Figure 4.9.k, wherein the volume integral of pressure transitions from a negative suction pressure to a positive displacement while simultaneously increasing volume summation. The volume integral of pressure tends to become unstable as the master shell surface transitions through the induced bifurcation. This in part could be attributed to the morphing cell volumes used to discretize the fluid geometrical changes during the simulation.

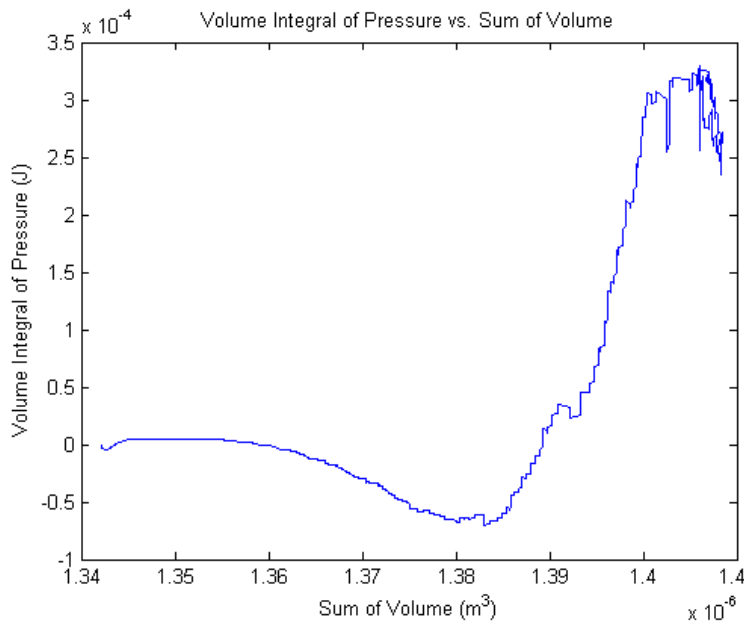


Figure 4.9.m Fluid volume expansion pressure profile

As the master and slave surfaces deflect, the fluid region is distorted to accommodate the change in the boundary surface geometry. If the cells are forced to change rapidly at any one step increment, then the residual error becomes excessive. This is not

believed to be the outcome shown within Figure 4.9.k and Figure 4.9.m, as the solver makes a gradual climb atypical from a residual error accumulation.

The divergent shift from a negative suction pressure during the volumetric contraction within the first 2200 iterates occurs as the strained master surface nears the equilibrium state of stress. At the instant of induced master shell bifurcation, there is sufficient strain within the shell element to forcefully move the neighboring fluid region. Once the master shell surface nears the equilibrium position at maximum deflection, the neighboring slave surface in the chamber overcomes this master shell applied load and the chamber pressure reverts back to a positive volume integral of pressure. The slave shell surface return spring back reverses the master shell surface mechanical strain and allows for the stored energy to restore the master surface into the initial vertical position. This behavior is further examined in the left and right chamber simultaneously simulation. Decoupling the left and right side chambers allowed for attention to be directed on how the master shell surface bifurcation influences the neighboring fluid region.

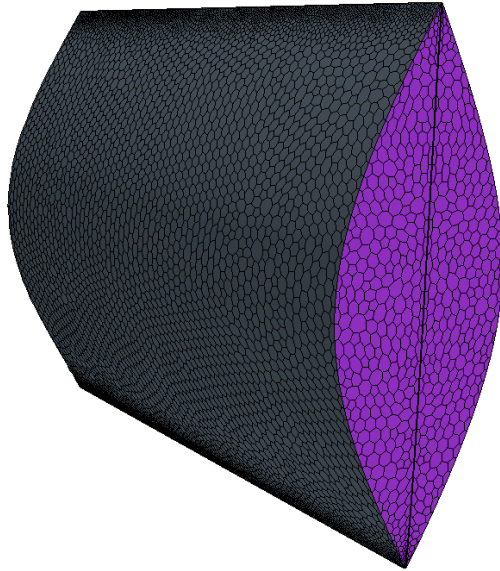


Figure 4.9.n Left & right side fluid region initial mesh discretization

The characteristic response to each fluid region relative to this driving surface is discussed aside from the complete system which features both the left and right side chambers. The simulation modified to feature both the left and right side chambers then permits the fluid-structure interaction to be solved simultaneously for the system as a whole.

The initial polyhedral fluid region mesh is shown within Figure 4.9.n for the left and right side chambers used within the coupled simulation. As in the previous analysis, the

forward and aft porting conditions are defined as stagnation boundaries which emulate an infinite fluid region adjacent to the port openings. The left and right forward ports shown in Figure 4.9.n by the purple shaded regions are permeable boundaries which allow fluid to move in and out of the chamber. The polyhedral mesh density increases along the top and bottom connection between the master and slave surfaces. The grey regions represent the fluid neighboring the structural wall co-simulation surface. This boundary is impenetrable and is designated as a no-slip boundary condition, which tends to grip the passing fluid as the shell surfaces move relative to the fluid region. The



Figure 4.9.o Left & right side final mesh discretization

nodal displacements imported from Abaqus implicit numerical analysis provide the response to the simulated fluid contact force neighboring the structure. Data is exchanged during the simulation between Abaqus and STAR-CCM+ to redefine the mesh, run requested scalar reports and to achieve a convergent numerical solution. The fluid region mesh is updated at each step incrementation and is modified to fit the deformed geometry. The mesh definition is shown at the final step incrementation in Figure 4.9.o. In this simulation, the input torque applied at the bottom points forward and aft are directed CCW as to upset the leftward master shell surface bifurcation mode. The left side chamber mesh discretization experiences decreased mesh base size and increased density. The fluid region conforms to the narrowing gap between the left chamber master and slave surfaces. The right side chamber mesh base size maintains the target dimension as the gap between the master and slave surface is increased throughout the simulation. The collective left and right side fluid chambers exhibit a similar characteristic deflection as shown within Figure 4.9.c and Figure 4.9.i for the CCW and CW applied input torque.

By the symmetrical nature imposed in such a design, it is then anticipated that reversing the input torque in the CW sense would then give an identical deflection path in the opposite direction. The conjugate motion in reversing the applied input torque from CW to CCW changes the mass flux direction and the resulting fluid flow direction.

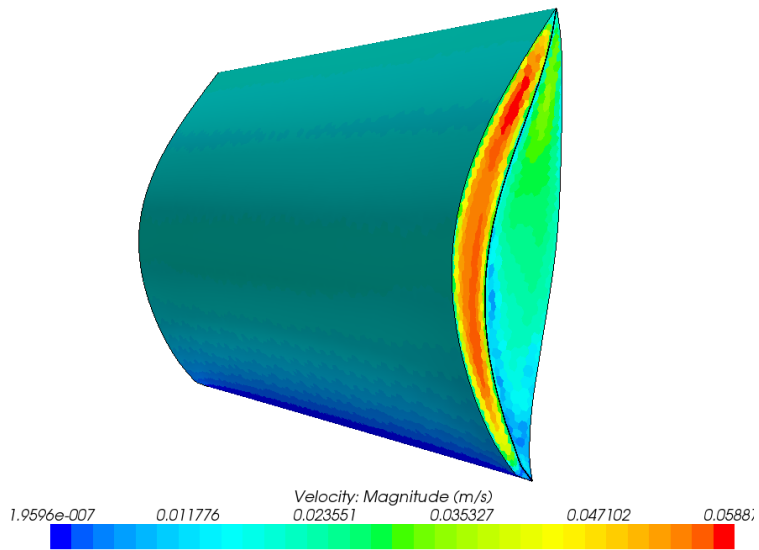


Figure 4.9.p Velocity field through forward port boundaries

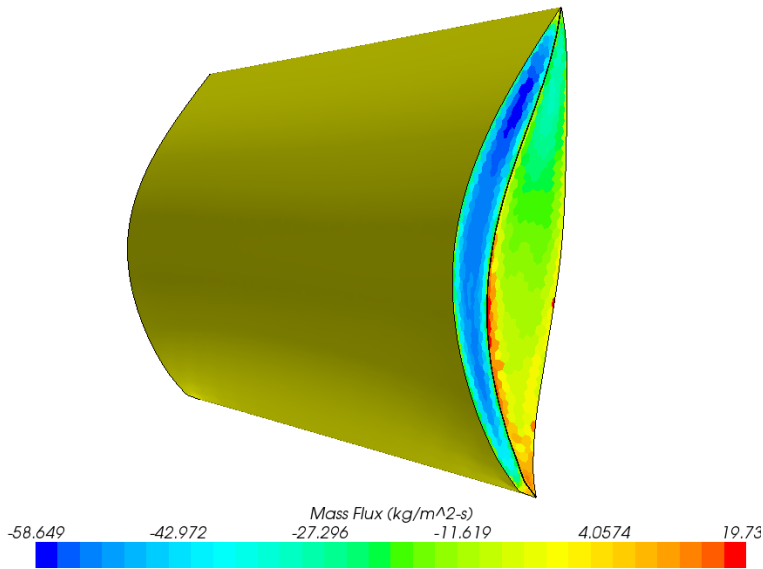


Figure 4.9.q Scalar field mass flux through permeable forward port boundaries

For reasons that will be discussed, the intent is not to move the fluid forward only to reverse flow direction; rather, the simulation is to demonstrate how the left and right side chambers simultaneously move fluid in opposite directions during the common master shell

surface bifurcation. This simulation does not include any such flow control devices which restrict mass transfer backflow into the chamber or create a pressure boundary along the forward and aft ports. The mass flux magnitude and direction is shown within Figure 4.9.q for the CCW input

torque induced

bifurcation. Negative

values indicate mass that

is moving outward from

within the internal

chambers and is split

symmetrically by the

forward and aft port

boundaries. Positive

values indicate mass that

is entering the chambers

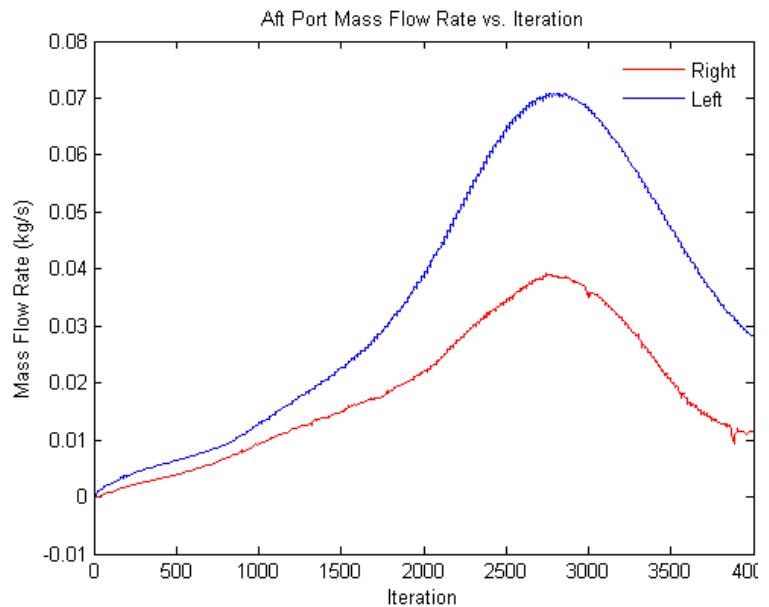


Figure 4.9.r Left & right aft port mass flow rate

moving through the permeable forward and aft, left and right porting boundaries. As shown within Figure 4.9.q, the left chamber experiences a negative pressure along the forward and aft ports; hence, mass is being expelled from within the chamber. The right side chamber simultaneously experiences a positive mass flux of a lesser magnitude directed into the chamber.

This mass moving into the fluid region is in response to the internal volumetric expansion between the right side master and slave surfaces. It is interesting to note that the majority of fluid within the right side chamber experiences positive fluid flow; however, there are localized cell volumes at the top right section which experience a negative mass flux. This is consistent with the phenomenon shown within Figure 4.9.k and Figure 4.9.m whereby the volume increases with an accompanying increase in pressure. The right side slave surface straightens near the top, adjacent to the negative mass flux cell volumes. The shell straightening modifies the initial bending load at the master-to-slave connection to a vertical tensile loading that stretches the slave surface. The right side slave surface bottom is near the applied input torque and maintains shell curvature and bending as the primary loading.

Fluid adjacent to this region experiences a positive mass flux indicating an increase in mass transferred into the chamber. The straightening phenomena can then give the required actuation in opening and

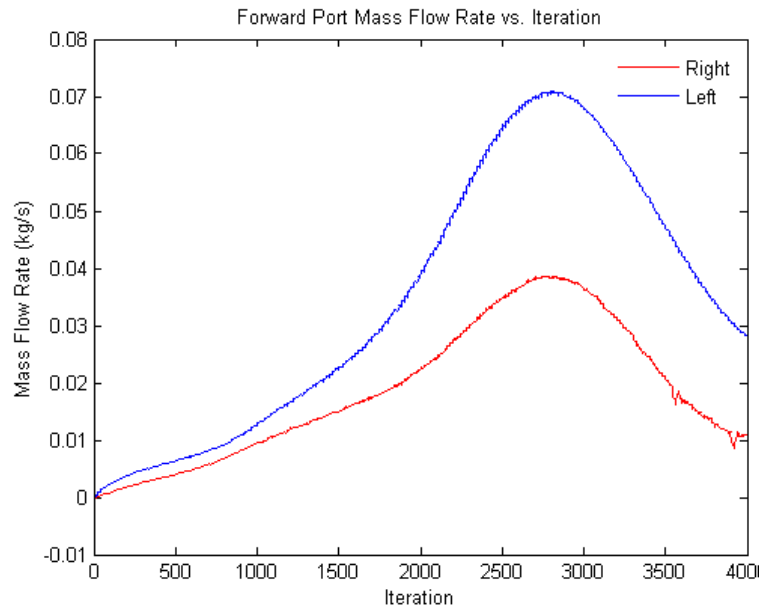


Figure 4.9.s Left & right forward port mass flow rate

closing valve once the chamber is filled and the chamber undergoes geometric stiffening.

The velocity magnitude is shown within Figure 4.9.p, which gives the rate at which mass moves across the left and right, forward and aft port boundaries. As anticipated, the left side chamber experiences fluid velocity magnitude that is nearly twice that of the right side chamber. The left side chamber nominal cross-sectional area is reduced as the master shell surface deflects toward the slave shell surface. For equal volumetric flow rate to occur through the left and right forward and aft port boundaries, the velocity is increased to maintain the mass conservation. This assumption presumes that the left and right side chambers are identically equal in geometry and material properties.

The chambers can be independently altered by modifying the left and right slave surface geometries as to achieve the desired fluid flow profile. The slave surface height and length must remain common to the left and right sides; however, the initial shell curvature and cross-sectional thickness along with the material properties may be modified to curtail the characteristic fluid response. The mass flow rate through the aft port is shown within Figure 4.9.r for the left and right chamber side permeable port boundaries. The right side port experiences mass flow rate nearly half that of the left side port. The characteristic profile for the left and right side porting is similar, with the varying mass flow rate magnitude that begins after the 1000th iterate. The increase in mass flow rate for the left is steeper than the right side port. The mass flow rate is a magnitude and not a vector quantity; hence, there is no such directional distinction made between fluid entering and leaving the chamber in the computation. The mass flow rate is governed by the propagated structure nodal displacements along the fluid-structural interaction boundary. For a mutual master surface applied simultaneously to the left and right side chambers, there exist two similar characteristic profiles with different peak magnitudes and rise rates. Fluid expelled from the chamber by the master surface undergoes a mass flow rate increase that is steeper than fluid pulled into the adjacent chamber.

A plot is provided in Figure 4.9.s, which displays the forward port mass flow rate for the left and right side induced chamber flow. The mass flow rate is identical to that discussed in Figure 4.9.r, indicating that the mass continuity equation is upheld and that the

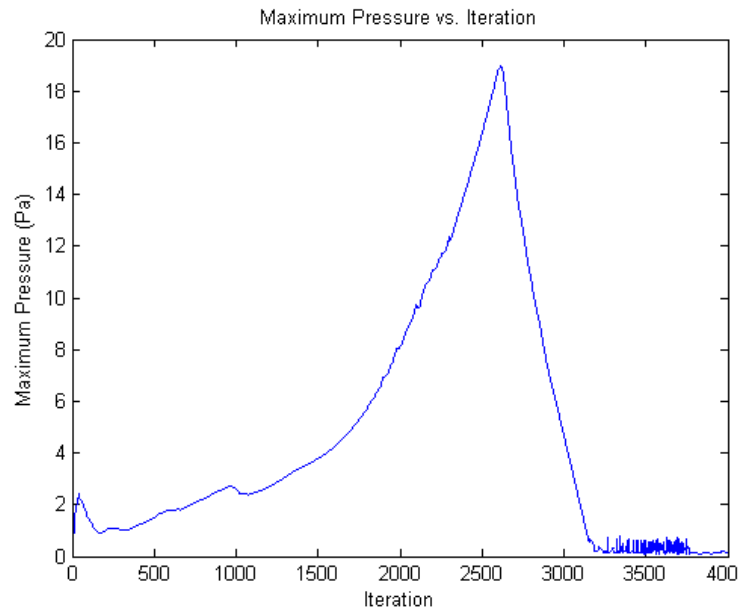


Figure 4.9.t Finite volume observed maximum pressure

forward and aft port boundaries experience equivalent fluid flow. Inner chamber fluid particle recirculation is possible; however, mass accumulation is not permitted for equal inflow and outflow conditions.

The maximum pressure achieved within the left chamber is plotted in Figure 4.9.t, which occurs along the porting boundary. The chamber pressure increases dramatically from 1500th to 2500th iterate, with a sharp decline immediately following peak pressure. The sharp spike in pressure occurs during the onset of the master shell surface bifurcation and steadily decreases as fluid is forced from within the chamber.

The pressure curve shown within Figure 4.9.t represents left side chamber and does not include pressure values for the right side chamber, which are persistently below the left chamber pressure profile as fluid is being pulled into the region. The first 2000 iterates are nearly linear up until the master shell surface begins to deflect, then the maximum pressure rate increases sharply to the noted peak value. The volume integral of pressure plot is shown within Figure 4.9.u for the

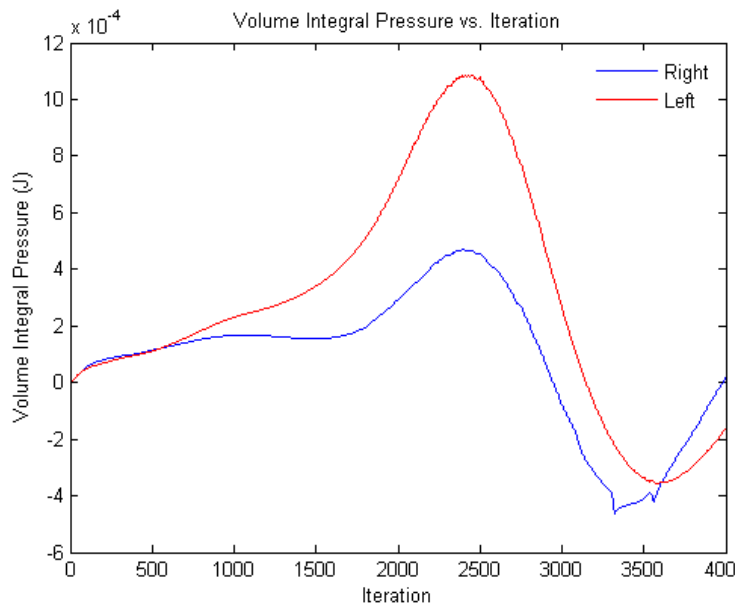


Figure 4.9.u Left & right pressure generated work profile

left and right chambers.

As anticipated, the left chamber leads the right and features a steepened rise throughout the fluid ejection period. The solution tends to be positive throughout the simulation for both the right and left side chambers; however,

towards the last 500 iterations the volume integral of pressure trends to a negative value. The volume integral of pressure indicates the work performed on the fluid region and the inner cell volume definitions. The increase in the theoretical fluid work is expected as the fluid is moved from the chamber and through both forward and aft ports. The negative work occurs as the fluid-structural interaction master and slave surfaces reach an equilibrium position. At this position, there is little to no additional fluid ejected from within the chamber and the solution trends towards a null or negative value. Approaching the equilibrium position, the loading that performs the work is increased to gain a marginal increase in the deflection path. This behavior exhibits that of a nonlinear system, as increasing the load fails to achieve a linearly corresponding output deflection. As the master surface approaches the slave surface, it is mechanically restrained from contacting or otherwise imparting inner shell interference. The left and right side chambers become critically stiff as the surfaces approach the equilibrium position. This pressure profile is typical of the stiffening stage which occurs during cardiac systole. The electrochemical impulse provides a mechanical disturbance which then allows the heart muscle to contract and stiffen.

The fibrous strain temporarily allows the heart to become significantly stiffer at systole than during the diastole state prior to contraction. The results provided describe fluid motion through forward and aft ports on the left and right side boundaries open to an infinite plenum of fluid neighboring the partially bounded regions. The ports are defined as stagnation boundaries, which are appropriately utilized to demonstrate the coupling between the left and right side

chambers. The next simulation is to conjure fluid response to a semi-closed container by defining



Figure 4.9.w Morphed mesh discretization in equilibrium position

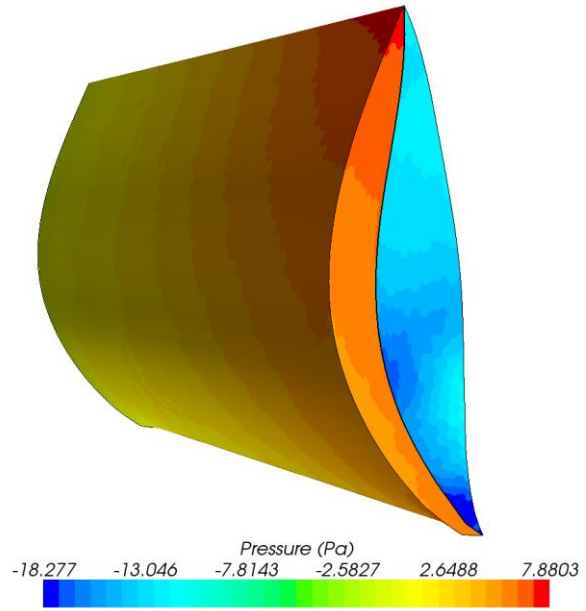


Figure 4.9.v Applied CCW input torque scalar field pressure response

the aft, forward and left, right ports as walls with floating volume vertices. The master and slave surfaces maintain wall co-simulation definition and connectivity to the port boundaries. The mesh vertices along the port boundaries allow for fluid regions to maintain conformance with the driven structure nodal displacements while maintaining cell volume continuity. If the port boundaries are treated as fixed vertices, then the master and slave surface definitions move relative to the ports and the cell volumes create a manifold separation condition.

The mesh distortion then prohibits co-simulation morpher from The mobile vertices tend to underestimate the scalar output computed which decreases solution accuracy. Though the preferred method would to be in avoiding such use of floating type vertices along numerical computation boundaries, it is necessary for the simulation to successfully execute and for the characteristic fluid response to be determined. While not discussed at this point, the design of ports along the forward and aft sections play an essential role in how fluid is controlled in moving through the chambers. Defining a periodically permeable porting boundary that is actuated by the driven master shell surface would then allow for the port mesh vertices to be fixed to a structural displacement.

The deformed mesh is shown within Figure 4.9.w for the port boundaries defined as floating type vertices. The in-plane mesh morph is similar to Figure 4.9.o with similar deflection path and magnitude along the master and slave shell surfaces.

The out-of-plane motion of vertices orthogonal to the port boundary is minimal given that the nodal shell displacements do not deflection normal to port boundaries. There is minimal mesh motion which occurs forward and aft to the left and right side chambers. The scalar pressure generated within the left and right fluid regions given a CCW input torque is shown in

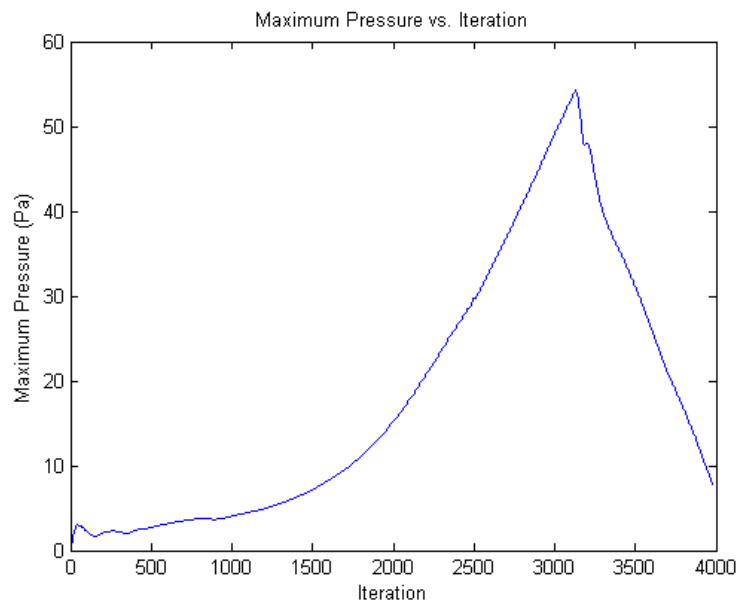


Figure 4.9.x Finite volume observed maximum pressure

Figure 4.9.v. The left side chamber experiences a positive pressure increase as the master shell surface moves toward the slave shell surface. Conversely, it is shown that the neighboring right side chamber experiences a volumetric expansion and a corresponding decrease in pressure. The pressure magnitudes are not exact as the mesh vertices are floating type cell volumes which conform to the structural nodal displacements and the relative mesh distortion of neighboring structural elements. Given the wall boundary applied along porting locations, the maximum internal pressure is amplified by nearly 3 times the induced pressure in assuming a stagnation boundary along the ports. The semi-rigid wall definition partially constrains the incompressible fluid and increases the pressure magnitude when a loading is applied to the region. The lack of a solid boundary along the port allows fluid to be ejected from the chamber with minimal mechanical resistance to obscure fluid flow. Adding a wall along the port boundary increases the resistance along the flow path and impedes mass transfer rate at the benefit of pressure generation within the chamber.

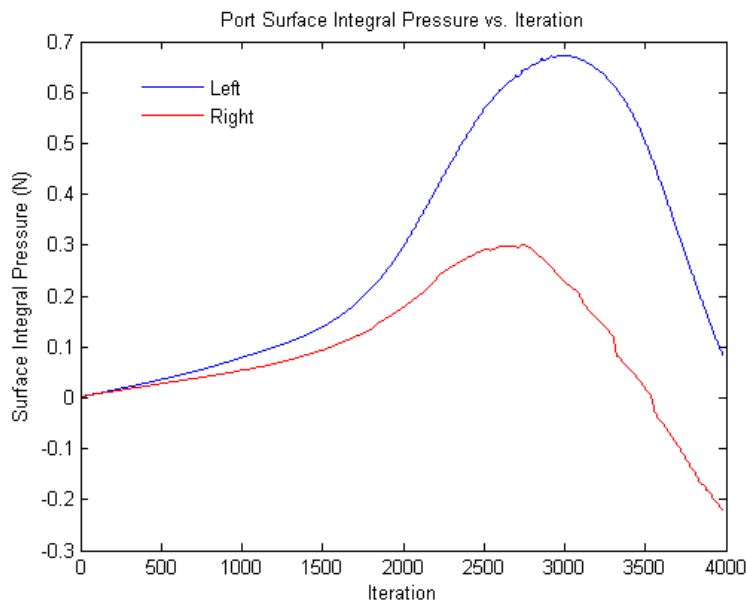


Figure 4.9.y Left & right side port surface force

Recall that as the heart undergoes isovolumetric contraction, mass transfer through the valves is null as the chamber pressure builds within the sealed control volume. This behavior is essential in the cardiac cycle, as the heart isovolumetric contraction generates pressure

required to simultaneously actuate the porting valve and to overcome flow resistance in ejecting fluid from within the chamber. Once the mechanically passive valve opens and blood is forced through the valve, a back pressure is sensed at the end of stroke which shuts the valve as the chamber simultaneously draws fluid into the chamber. The direct passive sensor actuating the valve prevents mass backflow and seals the volume for mass transfer.

The surface integral pressure measure is shown within Figure 4.9.y for the left and right chamber ports along the pressure sensing boundary. The left chamber observes an increased magnitude to the right side chamber with a similar profile. Pressure sensed through the left chamber port maintains a positive magnitude throughout the simulation. The right side chamber experiences an initial increase in pressure followed by a steady decline to a negative magnitude. The fluid region senses an initial pressure increase which is concluded by a negative pressure along the port boundary. The surface integral indicates a concave down pressure profile with a negative first order differential that follows the initial positive increase in the rate of applied pressure. As the master

surface structural element forces fluid within the volume to contract, the rate of increase in the pressure profile tends to decrease as the shell is deflected into the equilibrium position.

The pressure pulse is maintained for

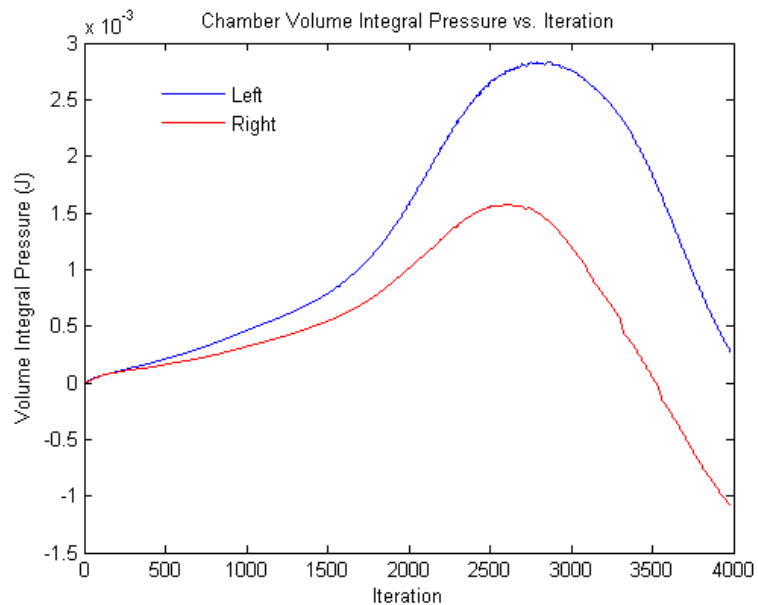


Figure 4.9.z Left & right side pressure generated work

nearly 1500 iterates or approximately 0.38 seconds, which permits the applied pressure to force fluid through the geometrically morphing port surface.

The change in geometry of the aft and forward ports modifies the chamber pressure output. The surface integral pressure measures the port specific field data observed along the port boundary. The fluid region itself experiences a similar mechanism for pressure amplification as shown within Figure 4.9.z. The pressure magnitude is greater for the left side chamber and observes a similar pressure profile experienced within the fluid volume. The right side chamber volume integral pressure trends closely in response behavior to that of the left side chamber. The volumetric pressure within the left and right fluid regions is influenced less by the morphing port geometry as shown within Figure 4.9.z. This nominal change in the port geometry on the left side narrows as the right side chamber observes an increase in the nominal port geometry cross-section. The surface integral pressure increases in the left side chamber while simultaneously enacting a right side chamber pressure decrease. Chamber pressure is fluctuated by master and slave shell surfaces that

deflect along the port boundaries. The fluid response adopts behavior to conform to the structural nonlinearity, which is evident in the surface and volume pressure plots. As the master surface deflection is initiated, there is a sharp rise in the observed

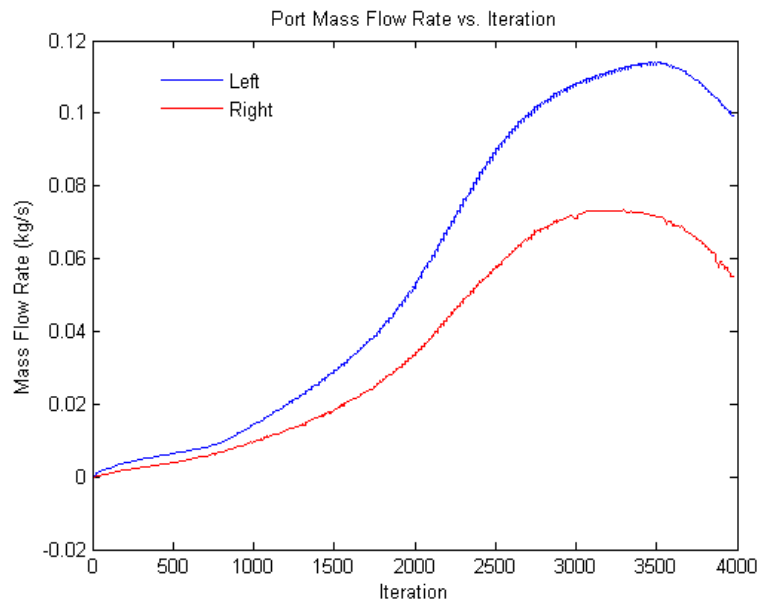


Figure 4.9.aa Left & right side ejection port mass flow rate

pressure which occurs near the 2000th iterate or approximately after 0.43 seconds during the 1 second stroke length.

During this time, the master surface shell builds up the mechanical strain that induces the first bifurcation mode. It is immediately following the upset that the sharp rise in chamber pressure occurs, delivering a nonlinear rise in the mass flow rate as shown within Figure 4.9.aa. The mass flow rate plateaus after 3000 iterates or 0.75 seconds following the pressure peak as shown within Figure 4.9.z. The mass flow rate is linear as the master surface builds the mechanical strain, generating a mass flow rate nearly 1/6th to that observed at maximum peak only 0.5 seconds following the pre-strain cycle phase. For both the left and right side chambers, it is observed that the mass flow rate maintains a positive value as to reflect the computed scalar magnitude. The mass flow rate peak lags that of the pressure spike as the fluid passes through the port boundary. The fluid region experiences a pressure peak which results in the rapid increase in the mass flow rate as shown within Figure 4.9.aa. If the simulation were allowed to settle at the equilibrium position

following the peak pressure amplitude, then the extrapolated mass flow rate would trend towards a null value as the internal chamber pressure is relieved. The pressure profile as shown in Figure 4.9.z reaches a peak on the left and right side chambers at nearly the

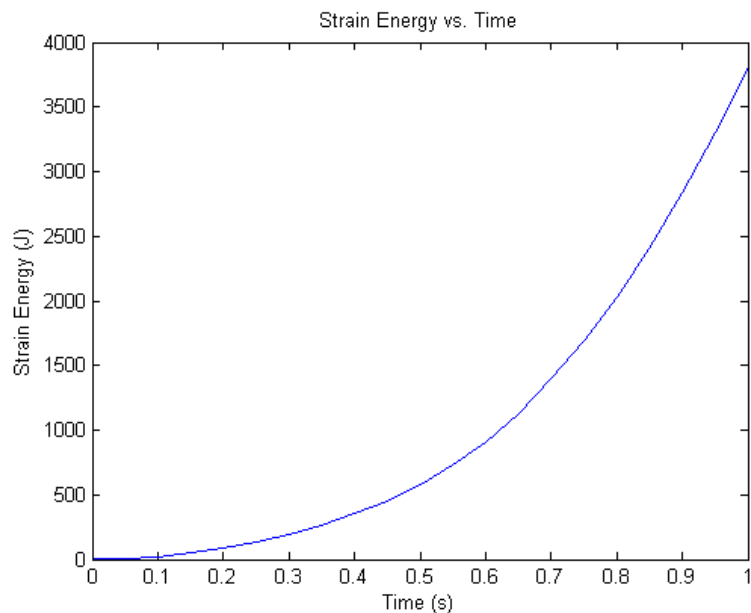


Figure 4.9.bb Shell strain energy versus time

same iterate, with the right side leading the left side chamber.

Once the mass flow is initiated within the fluid regions, the pressure tends to steadily decrease in amplitude. In Figure 4.9.z, the volume integral of pressure for the left and right side chambers decrease as the mass flow rate through the port alters the internal fluid volumetric region. The peak in magnitude for port and chamber pressure on the left side corresponds to the maximum pressure shown within Figure 4.9.x. The values reflected in Figure 4.9.x indicate the maximum pressure observed within the individual volume cell regions that comprise the bounded fluid. The observed chamber pressure is shown within Figure 4.9.v, which gives the magnitude and location for the pressure profile contours. Located along the bottom edge surface junction, there is a local increase in the scalar magnitude. The input torque applied along the edge tie gives an increase in the fluid directly adjacent to the coupled surfaces. Geometrically thinned regions of fluid near the top and bottom edges experience an increase in pressure as the shell surface is displaced. Fluid that is located along the slave surface apex observes a pressure response that is nearly $1/3^{\text{rd}}$ that of fluid nearest the surface edge junctions. The increase in pressure along the narrowed regions is important in the design, as fluid which occupies this boundary observes maximum shear stress. A localized increase in the wall shear stress could then damage the housed fluid particles if the fluid remains stagnant. Morphing the port output geometry is used as a means to amplify the internal chamber pressure near regions which undergo high wall shear stress.

The cycling induced by a reciprocating CW to CCW input torque requires a rapid response to the impending fluid motion. The use of an active actuator to control fluid flow is not permitting, as the frictional increase through the valve orifice significantly increases the fluid shear stress. An integrated active control valve lags in the response to the fluid motion and may not allow synchronization with the master shell surface timing. It is then necessary that a passive type control valve be implemented within the design, utilizing the nominal port cross-section to

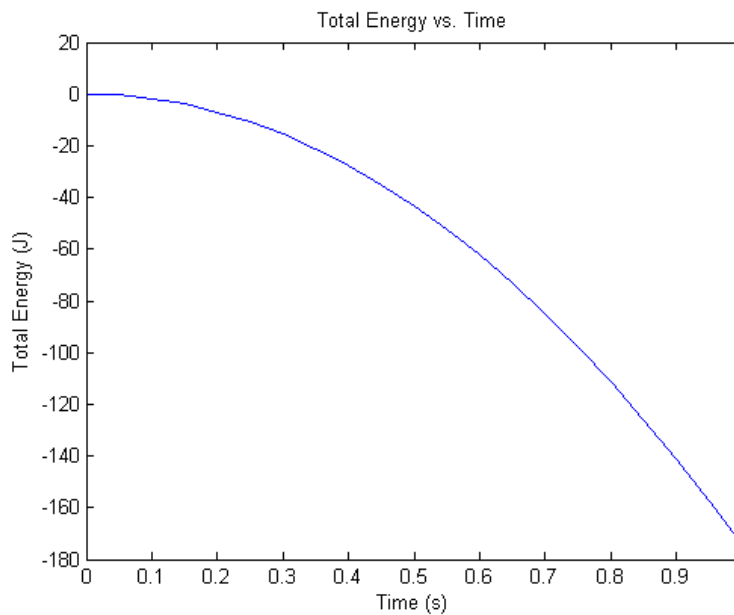


Figure 4.9.cc Shell input energy versus time

compensate for the desired pressure profile. The master and slave surface deflection increases or decreases port geometry based upon the directionality of applied input torque.

The morphing port valve geometry reverses the fluid structural interaction relationship, as the fluid is

then used to lead motion of the passively actuated port valve. The chamber fluid pressure imparts a load to the port valve, deflecting the valve in the direction of fluid flow. Pressure achieved within the chamber is induced by the bifurcating master and slave surfaces; however, the magnitude is governed by the valve material stiffness and compliance. As pressure builds within the chamber, the valve remains shut until the pressure differential forward and aft the port is sufficient to open the orifice. The phase is similar to the cardiac isovolumetric contraction, in which the chamber volume remains constant while the pressure increases to actuate the valve.

The master shell surface pushes and pulls the neighboring fluid regions which then opens and closes the passive actuating valve. Unidirectional fluid flow is achieved in using a check valve style passive valve to actuate the port boundary. A preliminary analysis is provided to illustrate use of a flapper nozzle valve design response. The structural model data outputted by STAR-CCM+ is stored within the database file. The structural analysis was discussed in depth prior to introducing the fluid region, which modified the resulting deflection magnitude. The

structural model nodal displacements along the shell master and slave surfaces give the computed strain energy as shown within Figure 4.9.bb. In the initial vertical configuration, the strain energy imparted to the master and slave shell surfaces is null. The shell deflection results in a nonlinear increase in the strain energy stored within the shell surfaces. The total energy is plotted in Figure 4.9.cc, which gives a negative value resulting from the master and slave surface bifurcation. The shell surfaces expend the initial mechanical pre-compression stored strain energy to impart fluid flow.

The elastic strain energy as shown within Figure 4.9.cc recovers the expended total energy from the initial to deflected state. Energy is converted from the initial pre-compressed master shell surface to the deflected master and slave surface equilibrium positions, less the energy required to move fluid within the left and right side chambers. Strain energy is recoverable and can be used in the next cycle phase to reverse deflection and fluid motion direction. Total energy includes both conservative and non-conservative energy terms in the computation. The external energy expended on the fluid is non-conservative and must be replenished for each half-cycle master shell bifurcation. The passive actuating valves internal to the fluid region do not contribute external work on the fluid and are not included within the energy dissipation.

4.10 FLAPPER NOZZLE VALVE DESIGN

The valves separating fluid boundaries along the loop-to-atrium, atrium-to-ventricle and ventricle-to-loop require pressure-actuated fluid flow design. The flapper nozzle valve facilitates the return flow Q_r by alternating the flapper angle φ as shown within Figure 4.10.a. Pivoted about the axis of rotation at a distance r from the nozzle centerline, the rotating flapper is to open and close fluid flow boundary as the driving master shell surface control pressure is periodically cycled. CW flapper valve rotation closes the valve while CCW flapper valve rotation opens the valve. The flapper valve flow forces, volumetric flow rate, and actuating pressure are linearized.

Housed within the device are six flapper nozzle valves to actuate fluid motion between the quadrants and to the exterior flow ports. The rectangular array as shown within Figure 4.10.b is to allow for a visual illustration of valve configuration. The pre-compressed master shell surface bisects the up-rightward diagonal path from the lower left to upper

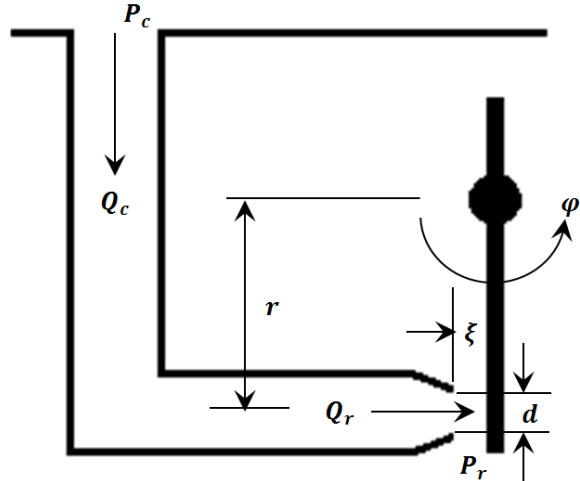


Figure 4.10.a Flapper nozzle variable definition

right corner. The valve actuation sequence is shown in Figure 4.10.b for the two bifurcation paths. The valves are designed as to permit fluid motion as shown within the CW and CCW bifurcation paths. As the shell rotates in the CW direction, O_{III} senses an increase in pressure and actuates the flapper nozzle valve to open at the interface between O_{III} and O_{II} while simultaneously closing shut valves interfaced at the top and left exterior fluid boundaries.

The CW shell rotation performs a reciprocating valve motion on the opposite partition, forcing open the external flapper valves at O_{IV} and O_I while simultaneously closing shut the

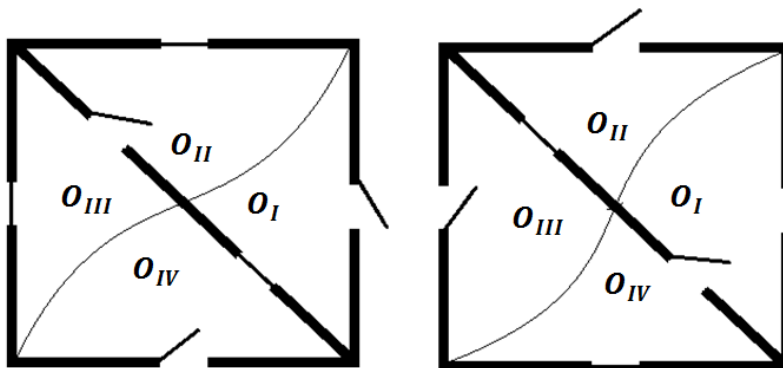


Figure 4.10.b Conceptual valve synchronization mapping

intermediary flapper valve between O_{IV} and O_I quadrants.

In the CCW plate rotation, the process is repeated in the reverse sense. As the shell flutters from

the CW to CCW bifurcation modes, the flapper nozzle valves simultaneously actuate the open and close positions as shown within Figure 4.10.b. The valve configuration differs from the simplified flask style design in that now fluid is compartmentalized into four separate chambers. Exterior boundaries are fixed and the focus is shifted from the master shell surface deflection to the valve mechanism employed in opening and closing the internal and external fluid boundaries.

4.10.1 Flapper Nozzle Valve Model

Rotating the flapper in the CCW direction opens the valve while a CW rotation closes the valve. The linearized volumetric flow rate through the flapper nozzle valve is given as,

$$Q_r = \frac{1}{2} Q_{ro} + K_q r \varphi + K_c (P_c - P_r) \quad (4.10.1)$$

Where Q_{ro} is the nominal flow rate through the flapper nozzle valve at steady operating conditions, K_q and K_c are the flow gain and pressure-flow coefficients. The opening of the flapper nozzle valve is given as $\xi = u + x$, where x is defined as $r\varphi$ for small displacements and u is the nominal valve opening. The area that restricts the flow is computed as $A = \pi\xi d$; where ξ is the height and d is the nozzle diameter. Applying the Reynolds transport theorem, the conservation of fluid momentum for the control volume through the flapper nozzle valve is defined as,

$$\vec{F} = \frac{\partial}{\partial t} \int_{c.v.} \rho \vec{u} dV + \int_{c.s.} \rho \vec{u} (\vec{u} \cdot \vec{n}) dA \quad (4.10.2)$$

Where \vec{F} is the vector force acting on the control volume, ρ is the fluid density, u is the fluid velocity vector and \vec{n} is the normal unit vector pointed outward from the control-volume surface. The scalar equation for fluid-momentum force acting on the flapper in the horizontal direction, where the first two terms represent the transient flow force F_t and F_s gives the steady flow force.

The transient flow force imparts the load necessary to either open or close the valve depending on the directionality of $\frac{\partial Q}{\partial t}$ given a steady flow force that continuously attempts to open

the valve. The transient flow force associated with the angular velocity of the flapper $\dot{\varphi}$ is stabilizing and the steady flow force associated with the angular position of the flapper φ ;

$$F_x = -\rho L \frac{\partial Q}{\partial t} + \rho \frac{Q^2}{A_n} + A_n P_c \quad (4.10.3)$$

$$F_s = K_{fq} r \varphi + (A_n + K_{fc}) P_c \quad (4.10.4)$$

$$F_t = \rho L K_q r \dot{\varphi} + \rho L K_c \dot{P}_c \quad (4.10.5)$$

$$K_q = \pi d C_d \sqrt{\frac{2}{\rho}} \quad (4.10.6)$$

$$K_c = \frac{\pi u d C_d}{\sqrt{2 \rho P_{co}}} \quad (4.10.7)$$

$$K_{fq} = 16 \pi u P_{co} C_d^2 \quad (4.10.8)$$

$$K_{fc} = 8 \pi u^2 C_d^2 \quad (4.10.9)$$

$$F_x = -[\rho L K_q r \dot{\varphi} + \rho L K_c \dot{P}_c] + K_{fq} r \varphi + (A_n + K_{fc}) P_c \quad (4.10.10)$$

The flapper is approximated as a simple mechanical non-uniform oscillator driven by a constant applied torque through a small angular displacement; where m is the flapper mass, c is the damping coefficient and g is gravity.

$$m L^2 \ddot{\varphi} + c \dot{\varphi} + m g L \varphi = F_x r \quad (4.10.11)$$

The second order system is simplified as a first order system when the system is overdamped. The inertia term $m L^2 \ddot{\varphi}$ is negligible assuming that the applied torque at the flapper pin contends primarily with the viscous fluid. Omitting the inertial term then gives a first order system for a simple pendulum flapper,

$$c \dot{\varphi} + m g L \varphi = F_x r \quad (4.10.12)$$

Cardiac isovolumetric contraction increases fluid pressure from approximately 10 to 80 mmHg immediately after filling. Volume is constant during the contraction until the control pressure is sufficient to open the valve, ejecting blood from the heart control volume. Diastolic pressure is equivalent to the control pressure required to actuate the valve into the open position.

This is achieved at the approximately 120 mmHg, when the force holding shut the flapper valve is exceeded and blood is forced from within the chamber. The return pressure is equal to diastolic pressure that follows the ejection of blood. Once the control volume is ejected, the heart undergoes an isovolumetric contraction to the minimum pressure of approximately 10 mmHg. The valves permit blood to enter the control volume until the relaxed heart is filled with blood.

To model the dynamic relationship between flapper valve actuation and applied pressure, a MATLAB Simulink control system model is created.

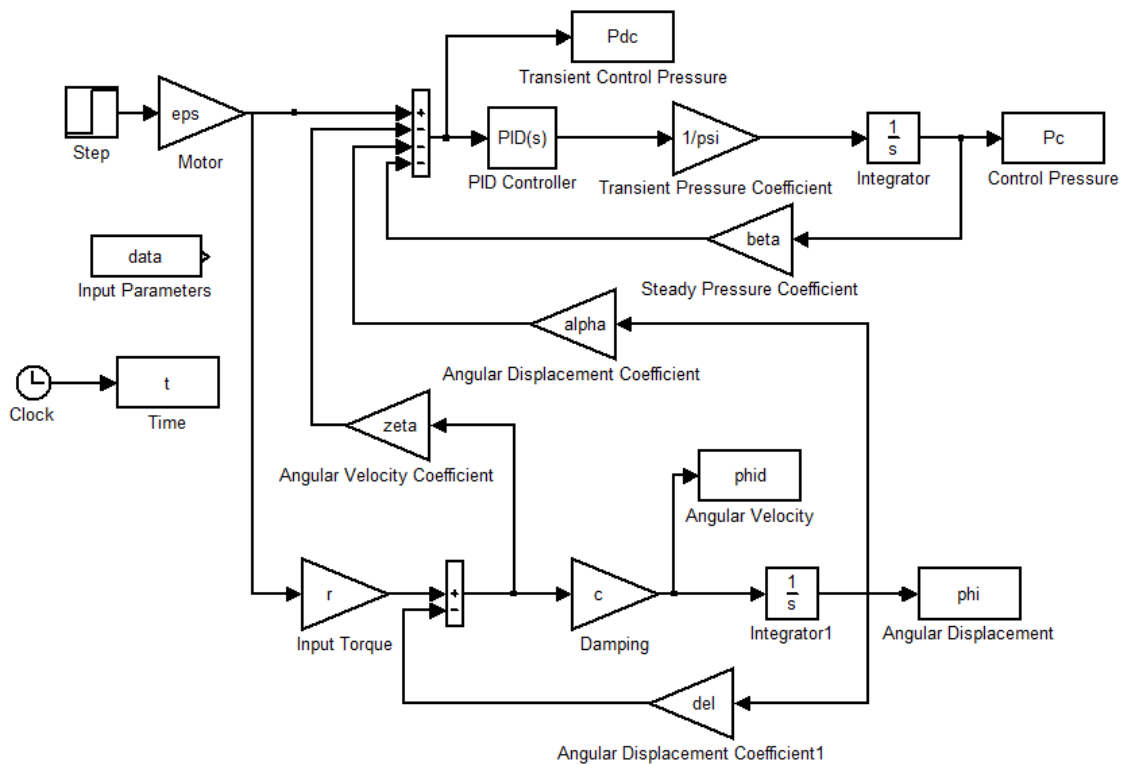


Figure 4.10.c MATLAB Simulink flapper valve control system flow diagram

In this model, it is assumed that the control pressure P_c is equal to the systolic pressure required to actuate passive valve. The dynamic pressure actuates valve into the open position at approximately 120 mmHg while the static pressure maintains a minimum of 80 mmHg system pressurization following the applied pressure transient. In the first order model, the system plant couples the control pressure and flapper angular displacement to achieve the desired fluid system characteristics.

The system model is given within Figure 4.10.c for the set of first order systems coupled to give the mechanical response. Coefficients used within the model are provided in Table 4.10-a, which are approximated by scaled geometric dimensions of the heart and fluid properties equivalent to that of water. The objective in this analysis is not to quantify the input parameters; rather, to be near in scale with the appropriate unit conversions as to examine the flapper valve response to input control pressure.

Table 4.10-a Flapper valve variable definition

Variable	Definition
ρ	$1060 \frac{kg}{m^3}$
L	$0.01 m$
d	$0.005 m$
C_d	0.62
P_{co}	$80 mmHg$
r	$0.025 m$
c	0.05
α	$51.525 N$
β	$9.857 \times 10^{-4} m^2$
δ	$1.893 \times 10^{-6} N - m$
ε	$40 \frac{N}{A - m}$
ψ	$1.112 \times 10^{-5} m^2 - s$
ζ	$2.171 \times 10^{-8} N$

Subsequent design iterations require that the valve input parameters be selected as to achieve chamber pressure ejection in conformance with the FSI simulation results. This model-based approach demonstrates utilization of the flapper nozzle design.

4.10.2 Model Simulation Results

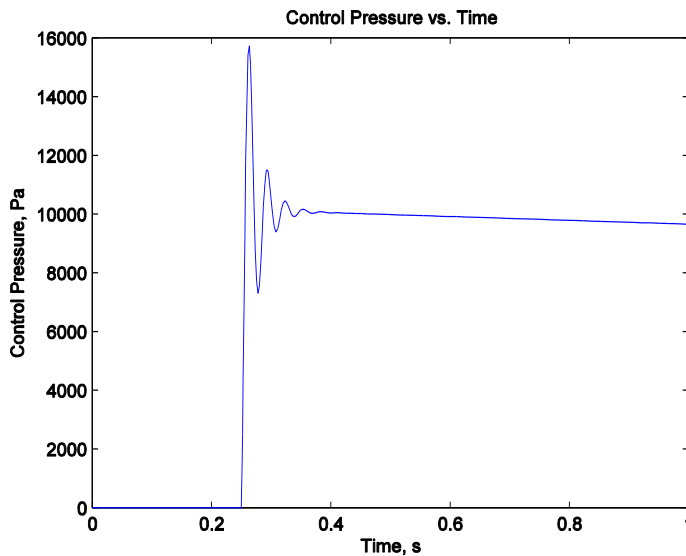


Figure 4.10.d Flapper valve control pressure versus time

The model shown within Figure 4.10.c gives the system characteristics, coefficient gains and input parameters for the flapper valve system dynamics. A step input is selected as the input actuation, which represents the master shell surface pulsation between CW to CCW input torque rotations.

The structural analysis for the master shell surface gives the deflection path and the resulting pressure amplitude within the chamber. The flapper valve response is treated as a separate entity from the obtained simulation-based numerical results.

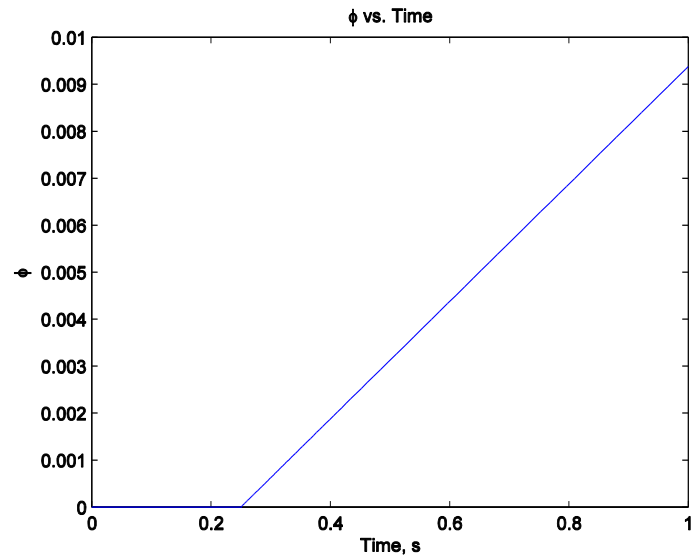


Figure 4.10.e Flapper rotation angle versus time

The valve actuation presumes a theoretical control pressure created by the master shell surface deflection, though it is not directly coupled with the structural analysis. This analysis is parsed as to avoid excessive computational resources and to independently investigate flapper valve response in controlling fluid port boundaries. The model includes a single flapper nozzle valve and does not incorporate the multiple valve synchronization design shown within Figure 4.10.b.

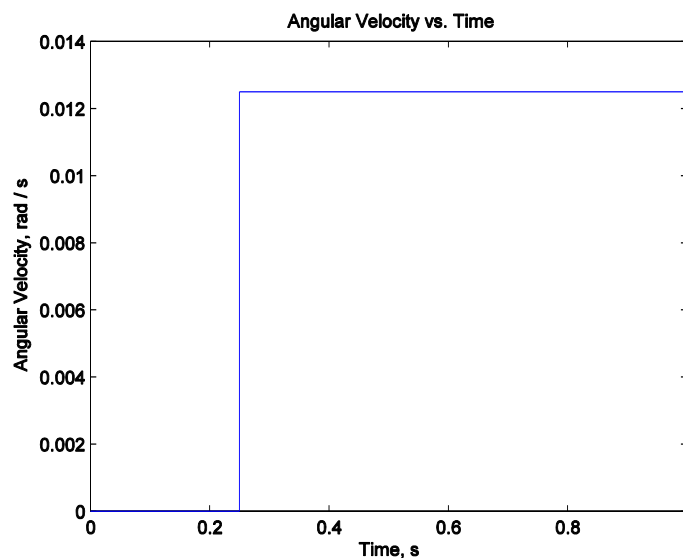


Figure 4.10.f Angular velocity versus time

In Figure 4.10.d, the systolic control pressure is achieved nearing 16 kPa or 120 mmHg to open valve, then settles to the diastolic control pressure of 10 kPa or 80 mmHg. The blood control volume observes a momentary applied pressure that is stored within elastic blood vessel walls released during relaxation.

Figure 4.10.e displays linear angular displacement with time as the flapper valve transitions toward the open position after 1 second elapsed time. Adjusting the input torque applied to the flapper pivot increases the magnitude of the angular displacement.

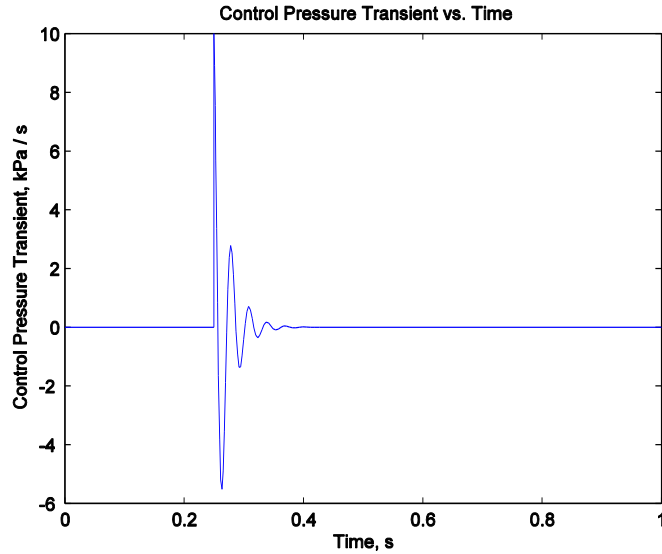


Figure 4.10.g Control pressure overshoot response

Increasing the rate at which the flapper valve can respond requires an increase to the applied input torque at the flapper pivot or a change in the motor torque constant. The increase in applied input torque is achieved by increasing the characteristic pivot joint material stiffness at the flapper rotation axis. The control pressure transient is shown in Figure 4.10.g for the applied step input. The control

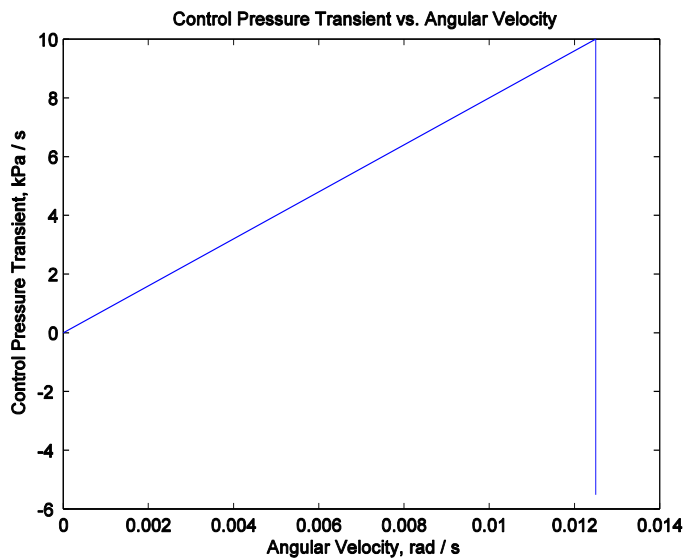


Figure 4.10.h Valve control pressure versus time

pressure transient mimics systolic conditions observed during the ventricular contraction. The applied pressure transient settles at approximately 0.1 seconds following the initiation of valve opening. Flapper valve angular velocity during the applied control pressure stroke remains constant as shown within Figure 4.10.f.

The angular displacement changes through time, but the rate at which the valve changes position is constant. Plotting the control pressure transient versus angular velocity shown in Figure 4.10.h indicates that the control pressure linearly varies with the angular displacement, consistent with first order system behavior.

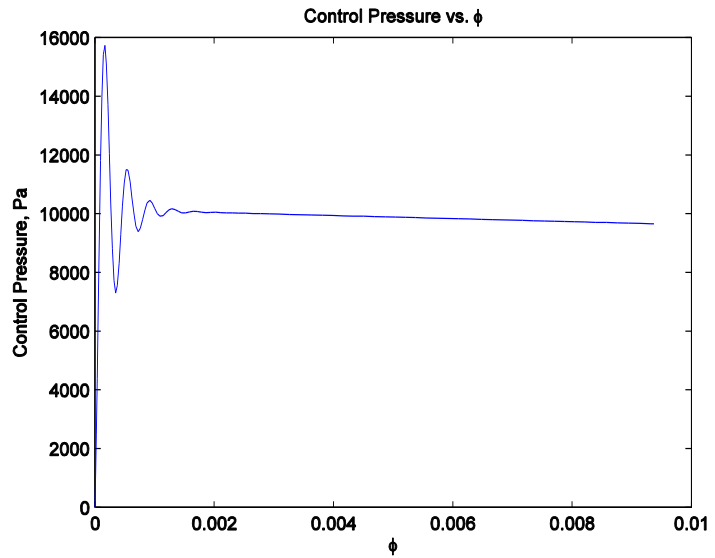


Figure 4.10.i Control pressure versus rotation angle

Figure 4.10.i gives the relationship between control pressure and flapper valve angular displacement. Systolic pressure amplitude forces the valve to open and continues through the stroke of the pendulum as the applied input torque overcomes the viscous fluid damping flapper

valve motion. The fluid flow forces applied to the flapper valve maintain the diastolic pressure magnitude as the angular displacement is increased at the flapper pivot.

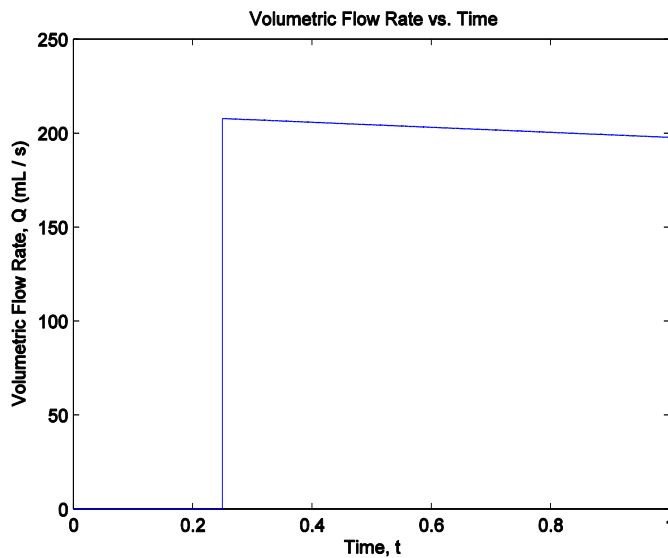


Figure 4.10.j Volumetric flow rate versus time

The pressure versus volume plot gives a direct corollary between applied pressure and supplied volumetric flow. Modifying the PID controller to

achieve minimal overshoot and settling time, an approximation for the volumetric flow rate is computed using the known parameters and the numerical simulation results obtained for ϕ and P_c as shown in the volumetric flow rate versus time plot in Figure 4.10.j.

Volumetric flow rate through the flapper valve nozzle maintains a nearly constant rate with a gradual decay. Given the approximate volumetric flow rate through the flapper nozzle valve and the known control pressure that actuates the valve, it is then possible to obtain a pressure versus volume relationship for the set of selected input parameters.

The desired pressure versus volume relationship is highly nonlinear; however, such a response is not expected using the provided linear equations. The valve is not designed to generate the nonlinear flow dynamics observed in the cardiac cycle. The nonlinearity is introduced by the FSI simulation-based numerical results. To match the pressure versus volume relationship, the valve cannot alone yield such a nonlinear fluid flow profile. This nonlinearity is created in using the master shell surface bifurcation to deflect neighboring slave shell surfaces which then results in fluid displacement. The flapper valve responds to the enacted pressure transient and to release mass

through the control volume consistent with the driving structure nodal displacements. The volumetric flow rate observed through the valve is governed linearly by the direct pressure input to the valve.

Plotting the pressure versus volume ejection as shown within Figure 4.10.k gives the

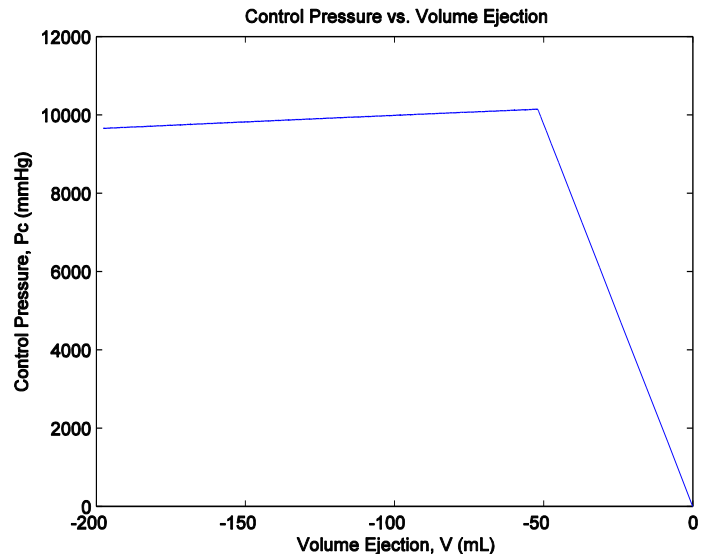


Figure 4.10.k Control pressure versus ejection volume

linear relationship in using the flapper valve to linearly moderate and control chamber pressure. To achieve the nonlinear fluid response, it is then required that the valve be used in sequence to the master shell surface deflection as to mimic the cardiac pressure versus volume profile.

The cardiac cycle is not initiated by the compliant valve motion; rather, the pump control pressure initializes the valve position along the port boundaries. Incorporating mechanically pre-compressed master shell surface deflection to generate fluid flow that is controlled by the housed flapper nozzle valves encompasses two essential components in replicating the nonlinear cardiac cycle.

Current-state technologies fail to provide a pump capable of generating fluid flow without significant shear stresses while simultaneously actuating passive valves to regulate port boundaries. Furthermore, common approach is to treat the valve design separate from that of the pump. Any such contrived design which fails to integrate pressure controlled valve actuation is handicapped to the fit, form and function of the human heart. The master shell surface displacement replaces fluid acceleration as used in impeller type designs by gently squeezing the delicate fluid. With the implementation of pre-compressed mechanical shell carefully designed to replicate the pressure-volume transient, it is possible to provide such fluid motion without imparting severe shear stresses that damage the blood.

4.11 QUADRANT CUSPED PASSIVE VALVE ACTUATION

The fluid flow through the port boundary must be passively controlled through the use of a mechanically compliant actuating valve. The open and close valve positions must be passively actuated given the applied surface pressure and magnitude. Bisecting the four quadrants into a cusped configuration maintains biaxial symmetry about the horizontal and vertical valve central axes. The flapper valve response to applied control pressure permits the use of said valve to regulate fluid flow through port boundaries. This valve type is configured as to allow positive

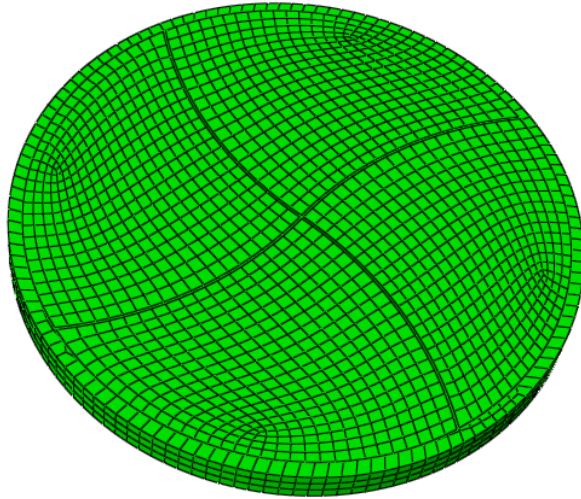


Figure 4.11.a Quadrant cusped flapper valve mesh discretization

during operation as to avoid the onset of blood coagulation and accumulation of fluid particles on stagnant surfaces which can react with the blood chemistry. Not all surfaces are permitted free motion; however, it is the objective to make all fluid bounding surfaces distort as to introduce wall shear stress in stagnant regions. The valve is shown within Figure 4.11.a viewed from the top in the closed position. Located beneath the top quadrant cusped valve is a backstop that prevents the valve from distorting beyond the planar surface during a negative pressure impulse.

The structural analysis is performed using Abaqus commercial software with a linearly ramped pressure load applied to the underside surface directed outward normal from the valve surface. A uniformly

pressure to open the port while a negative pressure forces the valve into the closed position. The cusped valves are constrained along the valve peripheral edge, which is simplified as a stagnant interior cusped valve that undergoes outward and inward flutter normal to the compliant cusp.

It is desired that any blood contacting the valve element move

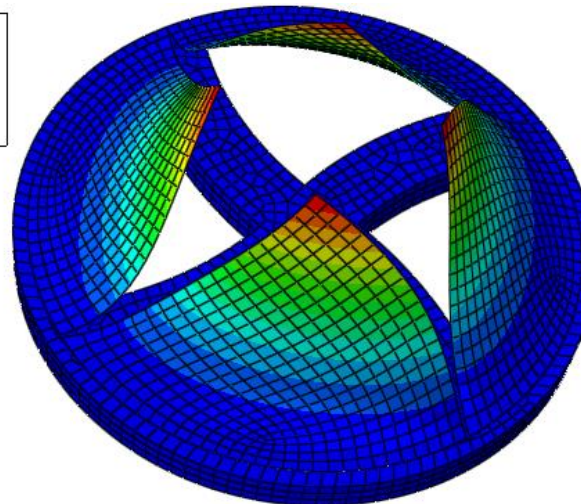
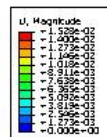


Figure 4.11.b Applied surface pressure deflection

distributed surface pressure is applied to the bottom of hexahedral meshed shell surface which deflects upward as shown within Figure 4.11.b. The applied load is to emulate the results obtained from the FSI simulation-based numerical results. The contours display displacement magnitude for the cumulative x , y and z directions showing a maximum displacement along the quadrant cusp point shown in red of approximately 15 mm at 1200 Pa applied uniform pressure. When subjected to a ramp input, in which the pressure is linearly varied with time, the nodal displacement for the cusp point follows linearity throughout the deflection of quadrant valve consistent with the flapper valve model simulation results. The deflection versus pressure plot is shown within Figure 4.11.c for a single valve, in which the actuating pressure forces the valve cusps into the open position. The nominal cross-section through the valve increases as the valve deflects upward as shown within Figure 4.11.b.

Positive pressure forces the quadrant cusps to separate into the open position, which permits increased fluid flow through the opening. The separation imparts motion of the valve surface that is to sever any stray fluid particles residing along the cusped valve surface. In this type of passive design, no such integrated active control systems are required to actuate the valve position. The valve actuation is governed strictly by the input control pressure amplitude and the resulting quadrant cusp valve deflection. Pressure direction is reversed to include negative applied pressure acting along the same

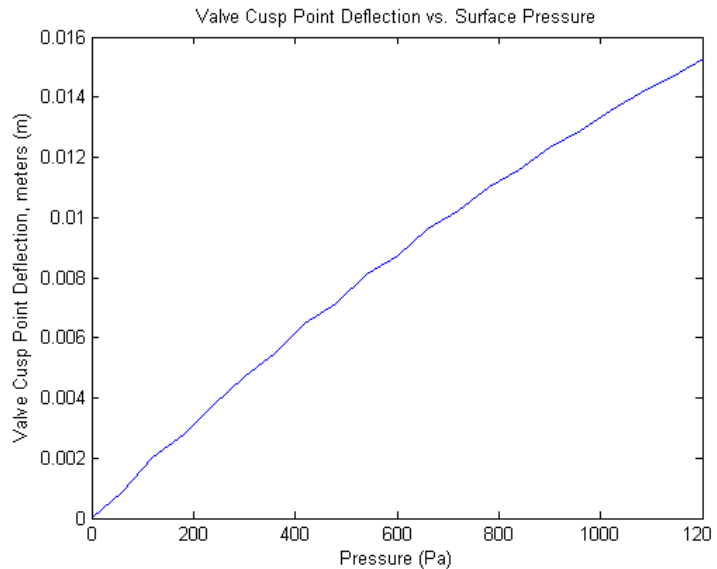


Figure 4.11.c Valve deflection versus actuating pressure

quadrant valve surface. The valve is forced into the closed position where it cannot deflect beyond the underside sealing backstop surfaces. Negative pressure is distributed uniformly along the valve surface, which creates a seal between the valve underside and the backstop top surface. The sealing action uses the negative applied pressure to hold shut the valve into the closed position without distorting the cusp. If the valve deflection is too large, then the cusp peripheral edge pulls away from the mechanical stop and a manifold condition is created. A break in the sealing surface then destroys the valve closure which maintains contact between cusped valves to backstop surfaces. The four valves function in coincidence, yet are independently actuated by the mutual input fluid pressure. The optimal design is one in which the underside mechanical stop is replaced by an imaginary contact interface between each valve edge. This creates a boundary in which the valves form a negative pressure suction seal, similar to the tricuspid and bicuspid valves in the heart.

5 CONCLUSION

A finite element structural model coupled with a finite volume fluid model simulates the motion of fluid particles through a geometrically morphing control volume. The numerical simulation demonstrates an approach which couples structural and fluid interaction at each time step increment to mimic cardiac mass transport cycle. The heart contraction exerts a controlled nonlinear structural bifurcation which induces systolic blood pressure and mass flow. Mechanical shell pre-compression coupled with input torque generates a master and slave surface internal chamber volumetric displacement. Numerical field output results for pressure, mass flow rate, velocity and volume are provided to illustrate the proposed fluid pump. Passive actuator valve design is required to actively moderate chamber ejection pressure amplitude. Positive displacement fluid flutter serves as a feasible mechanism to transport fluid continua through the vascular network.

BIBLIOGRAPHY

[1-15]

1. Burkhoff, D.M., *Mechanical Properties of the Heart and Its Interaction with the Vascular System*. Cardiac Physiology, 2011. **Cardiac Physiology**: p. 28.
2. Hicks, G.H., *Cardiopulmonary anatomy and physiology*. Vol. xiii. 2000, Philadelphia: W.B. Saunders. 523.
3. Burkhoff, D.M.P., *Assessment of Systolic and Diastolic Ventricular Properties via Pressure-Volume Analysis: a guide for clinical, translational, and basic researchers*. American Journal Physiological Heart and Circulatory Physiology, 2005. **289**(H501-12).
4. Suga, H., *Total mechanical energy of a ventricle model and cardiac oxygen consumption*. American Journal Physiological Heart and Circulatory Physiology, 1979. **236**(H498-505).
5. Semigran, M.J., *Heart Failure - Fundamental and Clinical Cardiology*. 2nd ed, ed. L.L.C. Taylor & Francis Group. 2012, Boca Raton: CRC Press. 475.
6. Evans, J.D.W., *Cardiovascular System*. 4th ed, ed. C. Course. 2012, Edinburgh: Mosby / Elsevier. 154.
7. Sawhney, G.S., *Fundamentals of Biomedical Engineering*. Vol. viii. 2007, New Delhi: New Age International Ltd. 264.
8. Korakianitis, T., *Optimized Pulsatile-flow Ventricular-assist Device and Total Artificial Heart*, L.L.C. LTK Enterprises, Editor. 2003.
9. Manning, N., *Hydraulic Control Systems*, ed. J.W. Sons. Vol. xvii. 2005, Hoboken. 446.
10. Zienkiewicz, O.C., *The Finite Element Method for Fluid Dynamics*. 6th ed, ed. Oxford. 2005, Boston: Elsevier Butterworth-Heinemann. 435.
11. Pai, P.F., *Highly flexible structures: modeling, computation, and experimentation*. Education Series, ed. AIAA. Vol. xvii. 2007, Reston: American Institute of Aeronautics and Astronautics. 742.
12. Tu, J., *Computational Fluid Dynamics: A Practical Approach*. 1st ed. 2008, Boston: Butterworth-Heinemann. 453.
13. Andersson, B., *Computational Fluid Dynamics for Engineers*. Vol. xi. 2012, Cambridge: Cambridge University Press. 189.
14. Axisa, F., *Modeling of Mechanical Systems*, ed. F.S. Interaction. Vol. 3. 1941, Amsterdam: Butterworth-Heinemann. 747.
15. Strogatz, S.H., *Nonlinear dynamics and chaos : with applications to physics, biology, chemistry, and engineering*. Studies in Nonlinearity. Vol. xi. 2000, Cambridge: Westview Press. 498.